



저작자표시-비영리-변경금지 2.0 대한민국

이용자는 아래의 조건을 따르는 경우에 한하여 자유롭게

- 이 저작물을 복제, 배포, 전송, 전시, 공연 및 방송할 수 있습니다.

다음과 같은 조건을 따라야 합니다:



저작자표시. 귀하는 원저작자를 표시하여야 합니다.



비영리. 귀하는 이 저작물을 영리 목적으로 이용할 수 없습니다.



변경금지. 귀하는 이 저작물을 개작, 변형 또는 가공할 수 없습니다.

- 귀하는, 이 저작물의 재이용이나 배포의 경우, 이 저작물에 적용된 이용허락조건을 명확하게 나타내어야 합니다.
- 저작권자로부터 별도의 허가를 받으면 이러한 조건들은 적용되지 않습니다.

저작권법에 따른 이용자의 권리는 위의 내용에 의하여 영향을 받지 않습니다.

이것은 [이용허락규약\(Legal Code\)](#)을 이해하기 쉽게 요약한 것입니다.

[Disclaimer](#)

Doctoral Thesis

Quantified Design Guidelines of Compact Active  
EMI Filters to Reduce the Common-Mode  
Conducted Emissions

Dongil Shin

Department of Electrical Engineering

Graduate School of UNIST

2018

Quantified Design Guidelines of Compact Active  
EMI Filters to Reduce the Common-Mode  
Conducted Emissions

Dongil Shin

Department of Electrical Engineering

Graduate School of UNIST

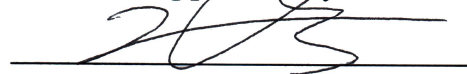
Quantified Design Guidelines of Compact Active  
EMI Filters to Reduce the Common-Mode  
Conducted Emissions

A thesis  
submitted to the Graduate School of UNIST  
in partial fulfillment of the  
requirements for the degree of  
Doctor of Philosophy

Dongil Shin

12. 04. 2017

Approved by



Advisor

Jingook Kim



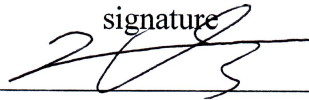
# Quantified Design Guidelines of Compact Active EMI Filters to Reduce the Common-Mode Conducted Emissions

Dongil Shin

This certifies that the dissertation of Dongil Shin is approved.

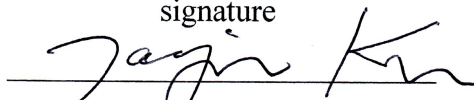
12. 04. 2017

signature



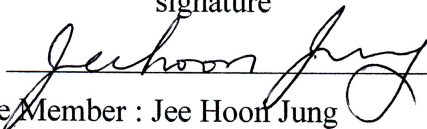
Advisor: Jinguok Kim

signature



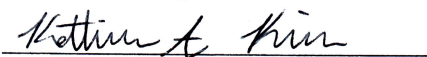
Committee Member : Jae Joon Kim

signature



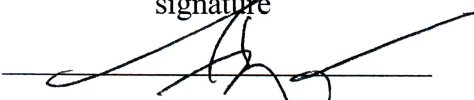
Committee Member : Jee Hoon Jung

signature



Committee Member: Katherine Ann Kim

signature



Committee Member : Ki Jin Han

## Abstract

In switching mode power supplies (SMPS), noise currents induced by the switching operation travel along the input power line and may, in turn, cause interference with other electronic systems, including the SMPS's auxiliary circuit. The noise current, caused by the switching operation to convert the voltage, is the main source of the conducted emissions.

The passive EMI filters (PEFs) composed of a common mode (CM) chokes, Y-capacitors, and X-capacitor are generally used to suppress the conducted emissions. However, the CM chokes are bulky and occupy a lot of room. Y-capacitors cause the undesired touch current flowing from the power lines to the earth GND.

In this thesis, three types of active EMI filters (AEF) – 1) voltage-sense voltage compensation (VSVC); 2) voltage-sense current-compensation (VSCC); 3) current-sense current-compensation (CSCC) – have been proposed to help overcome the limitation of the PEFs. The proposed AEFs have been designed as the feed-forward or transformerless configurations to manufacture in the compact size. Each AEF is completely analyzed by using the equivalent circuit model. Based on the rigorous analysis, the design guidelines of each AEF are established. In the design guidelines, the practical issues regarding the stability and high-voltage immunity are also considered. The performance of each AEF is validated through the experiments using a vector network analyzer (VNA) and the CM-conducted emissions measurements.

The feed-forward VSVC AEF is designed in a compact package to suppress CM-conducted emissions. The power line impedance is enlarged by the VSVC AEF and verified through the measurement. The VSVC AEF was installed in a 200W switching mode power supply (SMPS) board with 64 kHz and 110 kHz switching frequencies, demonstrating its usefulness by experiments. The performance degradation due to the magnetic saturation and the AEF grounding impedance was also analyzed and investigated

The transformerless VSCC AEF is developed to avoid the degradation due to the magnetic saturation. The sensing and compensation part is realized by only the capacitors, and the push-pull amplifier is utilized to generate the compensation signal corresponding to the sensed noise. Furthermore, the protection circuits against the high-voltage transient are developed and applied into the AEF. The VSCC AEF is then implemented into a real 2.2 kW current resonant inverter, and the conducted emissions are reduced by 5dB to 25 dB at a frequency range from 150 kHz to 6 MHz. In addition, the AEF's immunity against high-voltage transients is demonstrated by lightning surge tests.

The CSCC AEF is designed as the symmetric structure using the capacitive coupling. The transformer with a small number of turns is utilized for the sensing transformer to avoid degradation due to the magnetic saturation. The CSCC AEF is also designed using the proposed design guidelines

and employed into the real product. In the CM conducted emissions measurement, the CSCC AEF shows 5~20 dB noise attenuation from 150 kHz to 10 MHz. The degradation of the CSCC AEF due to the asymmetric structure is investigated by using the VNA measurements.

**Keywords:** Active EMI filter, common mode (CM), conducted emission (CE), current sense current compensation (CSCC), electromagnetic interference (EMI), feedback, feed-forward, high voltage transient, immunity, lightning surge, voltage sense current compensation (VSCC), voltage sense voltage compensation (VSVC)



# Contents

<b>Chapter I Introduction</b> .....	1
1.1. Introduction to EMI Issue in the Power Conversion System.....	1
1.2. Methods of the Noise Reduction Technique.....	2
1.3. Review of the AEF Topologies.....	4
1.4. Objective of This Work .....	8
<b>Chapter II Analysis and Design of the Feed-Forward Voltage Sensing Voltage Compensation Active EMI filter to Suppress the Common Mode Conducted Emissions</b> .....	10
2.1. Introduction.....	10
2.2. Analysis of Voltage Sensing Voltage Compensation Active EMI Filter.....	11
2.2.1. Feedback Loop Gain .....	12
2.2.2. Noise Attenuation By Impedance Boosting.....	13
2.2.3. Stability of the VSVC AEF.....	14
2.3. Design Guidelines of the VSVC AEF.....	15
2.3.1. Input Filter Capacitor, $C_{in}$ .....	15
2.3.2. Minimum Operation Frequency $f_o$ , $L_{inj}$ and $R_o$ .....	16
2.3.3. Sensing part and Amplifier, $R_1$ , $R_2$ and $C_{sen}$ .....	18
2.3.4. Optimization of Parameters Considering Stability .....	18
2.4. Implementation and Validation.....	20
2.4.1. Characterization of Components.....	20
2.4.2. Designed AEF and Experimental Validation using VNA.....	23
2.4.3. Conducted Emissions Measurement .....	27
2.4.4. Performance Degradation Due to Magnetic Saturation .....	30
2.5. Summary .....	32
<b>Chapter III Quantified Design Guidelines of Compact Transformerless Active EMI filter for Performance, Stability, and High Voltage Immunity</b> .....	34
3.1. Introduction.....	34
3.2. Analysis of the EMI Filter with the VSCC AEF.....	35
3.2.1. Circuit Model of the Total EMI Filter with the VSCC AEF.....	35
3.2.2. Circuit and Block Diagram Analysis .....	37
3.2.3. Loop Gain and Impedance Analysis .....	40
3.3. Design Guidelines of the VSCC AEF For the Performance .....	44
3.3.1. The Selection of $C_{inp}$ , $C_{sen}$ , $C_{inj}$ , $C_{DC}$ .....	44
3.3.2. BJT Selection and Push-pull Amplifier Design.....	47
3.4. Design Guidelines of the AEF For Stability and Immunity.....	49
3.4.1. Damping Circuit Design for System Stability .....	49

3.4.2. Surge Protection Circuit Design .....	56
3.5. Implementation and Measurements of the VSCC AEF .....	59
3.5.1. Design Flow and Implementation .....	59
3.5.2. VNA Measurements for Performance Validation.....	62
3.5.3. Measurement in a Real Application in a Product.....	63
3.6. Summary .....	66
<b>Chapter IV Design Guide of the Feed-Forward Current Sense Current Compensation Active EMI filter</b> .....	67
4.1. Introduction.....	67
4.2. Analysis of the EMI Filter with the CSCC AEF.....	67
4.2.1. The limitation of the Standalone feed forward CSCC AEF .....	67
4.2.2. Circuit analysis of the CSCC AEF.....	69
4.2.3. The Effective Capacitance of the CSCC AEF .....	71
4.3. Design Guidelines of the CSCC AEF .....	74
4.3.1. Approximation of the Expressions and $f_{op}$ .....	74
4.3.2. Design Guideline for the sensing transformer .....	76
4.3.3. The selection rule of $C_{inj}$ , $C_Y$ and $C_o$ .....	77
4.3.4. Design of the push-pull amplifier .....	77
4.3.5. The system stability and Damping resistor $R_d$ .....	79
4.4. The Implementation and Measurement of the EMI Filter with the AEF .....	80
4.4.1. Design Flow and Implementation .....	80
4.4.2. Performance Validation by VNA Measurements .....	83
4.4.3. CM Conducted Emissions Measurement.....	84
4.4.4. The Discussion.....	85
4.5. Summary .....	87
<b>Chapter V. Conclusion</b> .....	89
5.1. Performance Comparison Among the AEFs.....	89
5.2. Conclusion .....	90
<b>REFERENCES</b> .....	92
<b>APPENDIX. A.</b> .....	96
A.1. Introduction.....	96
A.2. Closed-Form Expressions of Radiated Emissions for the Package-Level PDN .....	98
A.2.1. Equivalent lumped-circuit model for the package-level PDN .....	99
A.2.2. Closed-form expressions for radiated emissions.....	102
A.2.3. Validation of the closed-form expressions.....	105
A.3. Quantified Design Guides of The PDN for Reduction of Radiated Emissions.....	111

A.3.1. Normalized regulation for radiated emissions .....	111
A.3.2. Dominant current path at each frequency region and sensitivity analysis .....	113
A.3.3. Extraction of optimal distance between the vias and the ESR values for target radiated emission level.....	117
A.3.4. Control of the resonance frequency .....	118
A.3.5. Flow chart of the quantified design guides .....	121
A.4. Summary .....	124

## List of figures

**Fig 1-1.** The concept of electromagnetic interference

**Fig 1-2.** The conducted emissions due to the parasitics in the power conversion system

**Fig 1-3.** Half-bridge isolated dc/dc converter with parasitic compensation in [8]

**Fig 1-4.** The example of the Active EMI filter

**Fig 1-5.** The topologies of the Active EMI Filters

**Fig 1-6.** The induction motor system configuration with the VSVC AEF in [19]

**Fig 1-7.** The induction motor system configuration with the CSCC AEF in [23]

**Fig 1-8.** The basic structure of the digital AEF in [27]

**Fig 2-1.** An Active EMI filter in a SMPS board

**Fig 2-2.** (a) Schematic of the VSVC AEF (b) Disconnected circuit model for calculation of the loop gain

**Fig 2-3.** (a) Gain margin with variable  $R_1$  (b) Gain margin and minimum operation frequency with variable  $R_o$

**Fig 2-4.** Design and optimization flow for the VSVC AEF

**Fig 2-5.** Measurements and modeling of the common mode choke; (a) the photograph and circuit model ( $L_{cm}=14\text{mH}$ ,  $R_{cm}=80\text{k}\Omega$ ,  $C_{cm}=8\text{pF}$ ) (b) impedance parameters

**Fig 2-6.** Measurements and modeling of the injection transformer; (a) the photograph and circuit model ( $L_{inj}=110\text{uH}$ ,  $R_{inj}=5.5\text{k}\Omega$ ,  $C_{inj}=1.8\text{pF}$ ) (b) impedance parameters (c) coupling coefficients extracted from measurements

**Fig 2-7.** Measurements and modeling of the unity gain amplifier ( $R_1=5.6\text{ k}\Omega$ )

**Fig 2-8.** The magnitude and phase of the loop gain for the designed AEF

**Fig 2-9.** Calculated and Experiment results (a) Schematic of the two-ports network (b) The  $1/Y_{21}$  between LISN and the noise source with and without the AEF (c)  $S_{21}$  parameter with and without the AEF



**Fig 2-10.** (a) Photograph of the implemented AEF in a compact package (b) Schematic of the implemented AEF

**Fig 2-11.** (a) the conducted emission measurement setup, (b) photograph of the AEF installed in the real SMPS board (c) Measured CM conducted emission in the real SMPS board

**Fig 2-12.** Experiments to verify the effect of core saturation (a) schematic of the AEF with an additional winding connected to the electrical load (b) the  $1/Y_{21}$  with the AEF by varying the additional current

**Fig 2-13.** (a) the schematic of the VSVC AEF with grounding inductance  $L_g$  (b) the  $1/Y_{21}$  with the AEF by varying the  $L_g$

**Fig 3-1.** (a) A typical CM EMI filter with passive L-C-L configuration (b) The transformerless AEF employed in the the filter configuration

**Fig 3-2.** Schemtics of the L-C-L EMI filter with the VSCC AEF

**Fig 3-3.** (a) the equivalent circuit model of the EMI filer with AEF (b) the circuit model after applying the miller's theorem

**Fig 3-4.** The block diagram of the EMI filer with the VSCC AEF

**Fig 3-5.** Calculation (dashed lines) and simulation (solid lines) results (a) impedance seen at the sensing node to the LISN,  $Z_{in,AEF}$  (b) the loop gain of the EMI filter with AEF,  $A\beta_t$

**Fig 3-6.** (a) The impedance of the AEF part,  $Z_{AEF}$  (b)  $NA$  due to the AEF and passive Y-capacitor

**Fig 3-7.** Impedacne of the AEF without the damping circuits,  $Z_{AEF0}$  (solid lines), The impedance is approximated to  $Z_{AEF0,low}$  (dashed lines) and  $Z_{AEF0,high}$ (dotted lines) at the low and high frequency ranges, respectively.

**Fig 3-8.** Investigation of four different configurations of the damping circuits (a) Circuit schematics (only the AEF parts are drawn for simplicity) (b) the impedance of the AEF part and the total loop gain,  $Z_{AEF}$  and  $A\beta_t$

**Fig 3-9.** The maximum phase of the loop gain,  $A\beta_t$ , while sweeping the value of (a) $C_f$ , (b) $R_f$ , (c) $C_{in}$ , and (d) $R_{in}$

**Fig 3-10.** The CM noise with and without the damping circuits (a) in the time-domain measurements (b) in the frequency-domain measurements

**Fig 3-11.** The proposed surge protection circuits for the AEF

**Fig 3-12.** the NA according to the parasitic capacitance in the (a) varistor,  $M_3$  and (b) TVS diode,  $T_1$

**Fig 3-13.** Design flow of the VSCC AEF

**Fig 3-14.** Photograph of the total EMI filter with the VSCC AEF

**Fig 3-15.** (a) Schematic of a VNA measurement (b)  $S_{21}$  parameter with the prospsed AEF and with the PEF (c) Measured  $NA$  with the VSCC AEF and with the PEF

**Fig 3-16.** (a) CM conducted emissions meusrement result (b) BJT voltages and currents measured during the lightning surge test

**Fig 4-1.** Comparison bewteen (a) the standalone type AEF in [40] and (b) the symetric CSCC AEF with  $C_{inj}$

**Fig 4-2.** (a)L-C-L EMI filter with the proposed CSCC AEF (b) the equivalent circuit model of the EMI filter with the proposed AEF

**Fig 4-3.** The block diagram of the EMI filer with the AEF

**Fig 4-4.** Calculation (doted or dashed) and simulation (solid) results (a) the loop gain (b) the close-loop gain of the EMI filter with the AEF

**Fig 4-5.** (a) the feedback input impedance,  $Z_{in,fb}$  and the impedance of the AEF part,  $Z_{AEF}$  (b) the  $NA$  with the AEF and with  $C_{inj}$

**Fig 4-6.** Comparison between  $Z_{AEF}$  and  $Z_{AEF,app}$

**Fig 4-7.** (a) the gain margin accorindg to  $R_d$  (b)  $Z_{AEF}$  with variable  $R_d$

**Fig 4-8.** The design flow of the CSCC AEF

**Fig 4-9.** The photograph of the total EMI filter with the CSCC AEF

**Fig 4-10.** (a) Schematic of a VNA measurement to verify the AEF performance of the CM noise reduction (b)  $S_{21}$  parameter with the AEF and with the PEF

**Fig 4-11.** (a) the CM conducted emissions measurement setup (b) measured CM conducted emissions with the AEF and the PEF

**Fig 4-12.** (a) Schematic of a VNA measurement to verify the transformation from DM noise to CM noise due to the balance structure of the AEF (b)  $S_{dc21}$  parameter with the asymmetric ( $C_{inj1}=3.3\text{nF}$ ) and symmetric ( $C_{inj1}=C_{inj2}=1.5\text{nF}$ ) AEF

**Fig A-1.** Development of PDN design guidelines as the reverse of radiated emission analysis

**Fig A-2.** Example of package-level PDN (a) Cross-section view. (b) Equivalent lumped-circuit model

**Fig A-3.** PDN structure in the spherical coordinates

**Fig A-4.** Calculation procedure for the far-zone radiated emissions

**Fig A-5.** (a) Photograph of the test board (b) Impedance covers from the models and measurements

**Fig A-6.** Comparison among the results obtained from the closed-form expressions, PEEC model, and HFSS with  $i_{IC}=1\text{A}$ . (a) Total radiated emissions (b) Radiated emissions caused by each current component

**Fig A-7.**  $H$ -plane normalized field patterns (solid line: HFSS, dot line: closed form expression) at (a) 30 MHz; (b) 108 MHz; (c) 300MHz; (d) 1.24 GHz

**Fig A-8.** (a) Maximum radiated emissions measurement setup in a semi-anechoic room (b) Maximum radiated emissions

**Fig A-9.** (a) Comparison between the  $|E_{reg}|$  and the actual radiated emissions (b) Comparison between the  $|E_{reg,n}|$  and the radiated emissions due to the 1A switching current at all frequencies

**Fig A-10.** (a) Current components obtained by solving (A.6) for the PDN lumped-circuit model (b) Dominant current path for the radiated emissions in the frequency range below the  $f_{res1}$  (c) Path at the resonance frequency of  $f_{res1}$  (d) Path in the frequency range between the  $f_{res1}$  and the  $f_{res2}$  (e) Path at the resonance frequency of  $f_{res2}$

**Fig A-11.** Radiated emission (a) at 30 MHz and at 300 MHz with varying  $l_{via1}$  (b) Resonance frequencies (108 MHz, 1.24 GHz) with varying  $R_{dec1}$

**Fig A-12.** (a) Simplified equivalent model of the test PDN structure (b) Calculation procedure of the resonance frequencies

**Fig A-13.** (a) PDN design flow satisfying the regulation of radiated emissions (b) Radiated emissions from the prototype PDN and the optimized PDN

## **List of tables**

**Table 2-1.** Component Values of The VSVC Active EMI Filter

**Table 3-1.** Components Values of The VSCC Active EMI Filter

**Table 4-1.** Components Values of The CSCC Active EMI Filter

**Table 4-2.** Specification of the Core for the Sensing Transformer

**Table 5-1.** Comparison of Performances and Characteristics Between AEFs

**Table A-1.** Values of the Circuit Elements Used in the PDN Example

**Table A-2.** Sensitivity of Radiated Emissions to PDN Parameters

## Nomenclature

<b>AEF</b>	Active EMI Filter
<b>ADM</b>	Amplitude Difference Measure
<b>BJT</b>	Bipolar Junction Transistors
<b>CE</b>	Conducted Emissions
<b>CM</b>	Common Mode
<b>CSCC</b>	Current Sense Current Compensation
<b>DM</b>	Differential Mode
<b>EFIE</b>	Electric field integral equation
<b>EFT</b>	Electric Fast Transient
<b>EM</b>	Electromagnetic
<b>EMC</b>	Electromagnetic Compatibility
<b>EMI</b>	Electromagnetic Interference
<b>ESD</b>	Electrostatic Discharge
<b>ESL</b>	Equivalent Series inductance
<b>ESR</b>	Equivalent Series Resistance
<b>EUT</b>	Equipment Under Test
<b>FSV</b>	Feature Selective Validation
<b>GND</b>	Ground
<b>IC</b>	Integrated Circuit
<b>LISN</b>	Line Impedance Stabilization Network
<b>MCU</b>	microcontroller
<b>MNA</b>	modified nodal analysis
<b>NA</b>	Noise Attenuation
<b>PCB</b>	Printed Circuit Board
<b>PDN</b>	Power Distribution Network
<b>PEEC</b>	Partial Element Equivalent Circuit
<b>PEF</b>	Power EMI Filter
<b>RE</b>	Radiated Emissions
<b>SMPS</b>	Switching Mode Power Supply
<b>S-parameter</b>	Scattering-parameter
<b>VNA</b>	Vector Network Analyzer
<b>VSCC</b>	Voltage Sense Current Compensations
<b>VSVC</b>	Voltage Sense Voltage Compensations

# Chapter I

## Introduction

### 1.1. Introduction to EMI Issue in the Power Conversion System

Electromagnetic interference (EMI) is a disturbance generated by an electric device which causes the other device to malfunction or critical problems. The noise emissions should be considered in the design process of the electric appliance not to pollute the electromagnetic environment, and the household appliances are required to satisfy EMI regulations such as the Federal Communication Commissions (FCC) and Comité International Spécial des Perturbations Radioélectriques (CISPR) [1].

In the regulation, the EMI problems are categorized as the conducted emissions and the radiated emissions and the limit of each emissions is presented. The conducted emissions mean that the noise coupling occurs through the conductive path as shown in Fig 1-1, and these are regulated at the relatively low-frequencies below 30MHz. On the other hand, the radiated emissions are the noise interfere with the victim through the radiated coupling. As compared to the conducted emissions, the regulation of the radiated emissions is defined at the higher frequency range from 30 MHz to 1GHz.

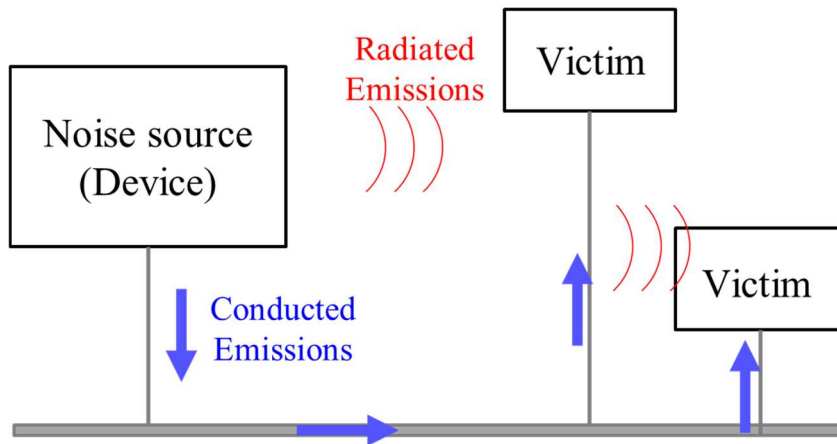


Fig 1-1. The concept of electromagnetic interference

In the power conversion system using the switching operation, the parasitic  $C$  between the heat sink and the switch components, and the parasitic  $L$  due to the device leads in Fig 1-2 are major culprits of the conducted emissions. The high-frequency ringing, which is related to the differential noise (DM) current,  $i_{dm}$ , can occur due to the parasitic  $L$  by device leads and increase the voltage stress of the component. Also, the high voltage transition ( $dv/dt$ ) due to the switching operation can generate the

common mode (CM) noise current, denoted as  $i_{cm}$ , by charging and discharging the parasitic  $C$ . Thus, as a power conversion system advances based on the high-speed switching operation, the conducted emissions became more serious, and designers should more carefully consider the EMI issue.

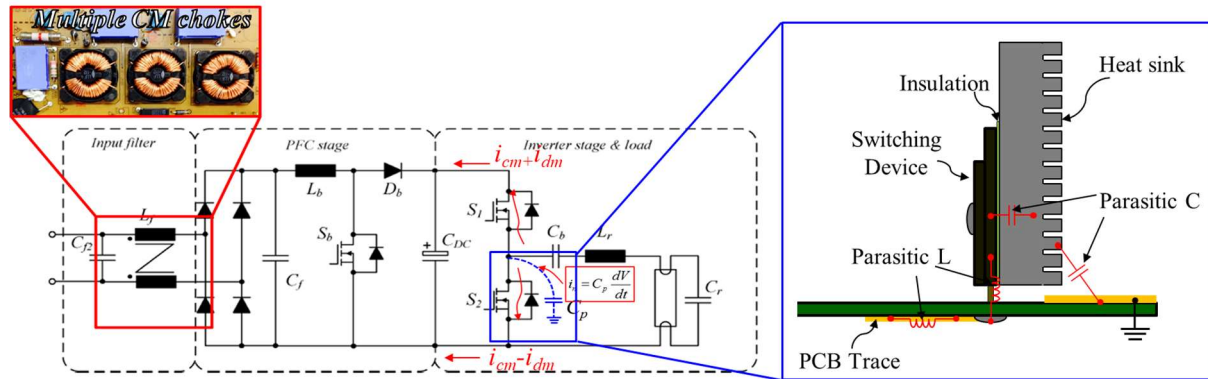


Fig 1-2. The conducted emissions due to the parasitics in the power conversion system

## 1.2. Methods of the Noise Reduction Technique

The passive EMI filters (PEFs) composed of the CM chokes, and X and Y-capacitors are widely used to suppress the conducted emissions. X-capacitors can reduce the DM conducted emissions from the switching mode power supply (SMPS) to the utility side by forming the low-impedance return path. The CM noise currents from the equipment under test (EUT) are also reduced by the high impedance of CM chokes and the low impedance shunt path due to Y-capacitors. Although the EMI filter can be easily implemented, it has some limitations. A large value of the Y-capacitor may cause dangerous the touch currents exceeding safety regulation limits and is therefore prohibited [2]. To achieve proper noise attenuation regarding CM conducted noise at the low frequency range, the PEFs are thus constructed as the multiple LC structures which occupy a lot of space. Also, in practice, the magnetic flux generated by the AC current partly remains inside the CM choke and magnetically saturates the core of the choke. The CM impedance of the choke can be significantly decreased due to magnetic saturation, and overall performance of the EMI filter is degraded when employed in a high power system [3]-[5]. An expensive core material is necessary to avoid such magnetic saturation. Furthermore, thick wire in the CM choke is required for high power applications. Thus, the size and cost of the CM choke remain design issues in EMI filters.

Several methods have been reported to effectively suppress the CM conducted emissions in a smaller size [6]. One of the methods is the passive cancellation [7]-[8]. In this method, the compensating winding is added on the converter transformer to replicate the noise. Using the

compensation capacitor corresponding to the parasitic capacitance that causes the CM noise current, the replicated noise is injected into the GND to cancel out the noise as shown in Fig 1-3. The passive cancellation can show good noise attenuations at the low frequency range, allowing for the input filter to be reduced. However, the parasitic capacitance should be identified to determine the value of compensation capacitor. Accordingly, it is difficult to be implemented in a complex SMPS board where the parasitic capacitance is not obvious.

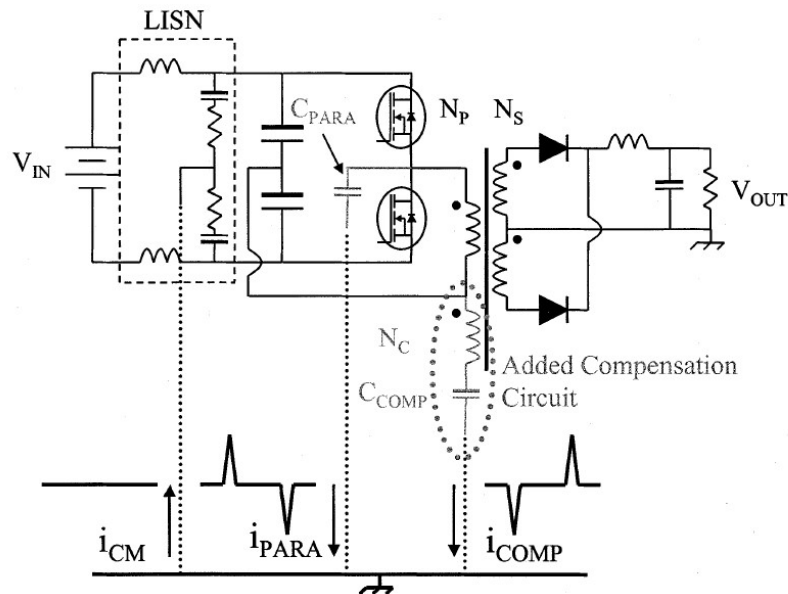


Fig 1-3. Half-bridge isolated dc/dc converter with parasitic compensation in [8]

Active EMI filters (AEFs) have been proposed to effectively reduce the CM conducted emissions in [9]-[31]. The AEFs are composed of the sensing, compensation part and amplifier as shown in Fig 1-4. The AEFs capture the CM noise from the EUT and inject the compensation signal corresponding to the captured noise. Identification of the CM noise is not necessary as compared to the passive cancellation since the operation of AEFs is just based on the sensed signal. Although the AEFs need several components and consume extra power, it would be the most practical solution for suppressing common mode noise in very low frequency, since it can be implemented in a compact size compared to the passive filters. Also, compared to the passive cancellation method, the AEFs can be applied to any SMPS board regardless of the complexity. Therefore, this thesis focuses on the AEF as the effective method to reduce the CM conducted emissions.



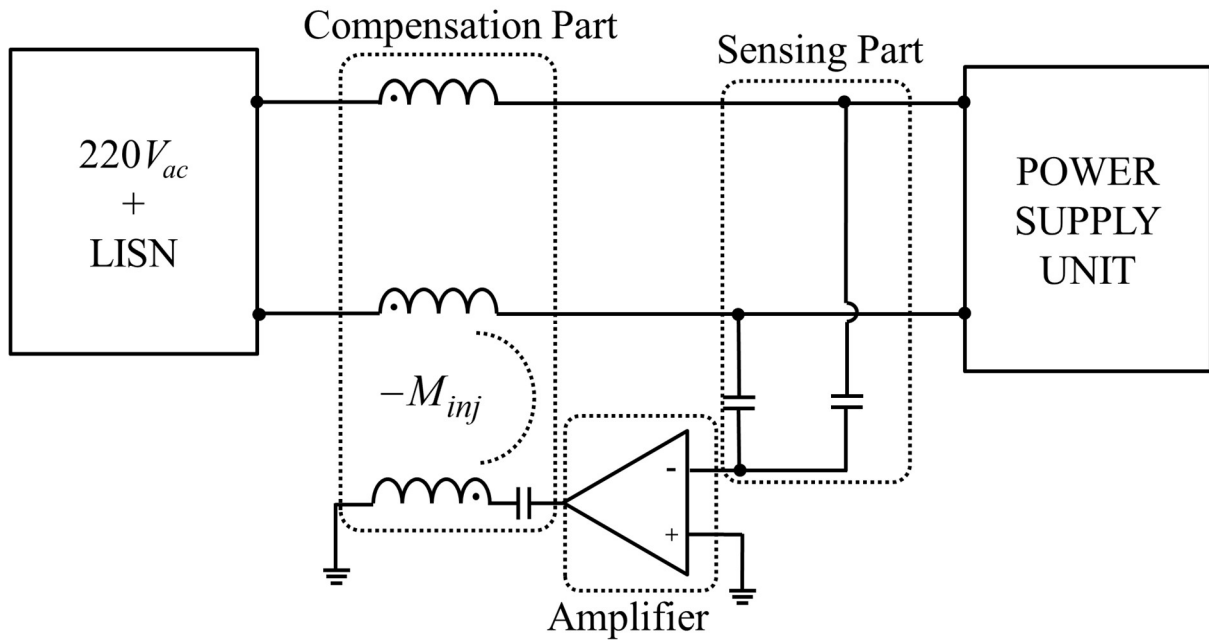


Fig 1-4. The example of the Active EMI filter

### 1.3. Review of the AEF Topologies

The active filter has been utilized to suppress the EMI problems such as the input/output ripple, harmonics and conducted emissions. The basic model of the AEFs using the bipolar junction transistors (BJTs) has been presented in [9]-[10]. The active ripple cancellation circuit, which consists of both operational amplifier (OP-amp) and a push-pull amplifier, has been proposed to suppress the DM noise cancellation and each topology has been explained in [11]. The ripple reduction by the active ripple cancellation filters of [11] has been demonstrated in time domain measurements, but the common-mode noise reduction in the conducted emissions frequency range has not been presented. Y.C Son has shown the general analysis of the active filter for EMI reduction based on the ideal amplifier model in [12]. In [9]-[10], each topology has been classified according to the sensing and compensation types and summarized as shown in Fig1-4. The current sense and voltage compensation are realized using transformers, whereas the voltage sense and current compensation are achieved by using capacitors. On the other hand, the amplifier part in the active EMI filters (AEF) can be implemented with either an OP-amp or a push-pull amplifier.

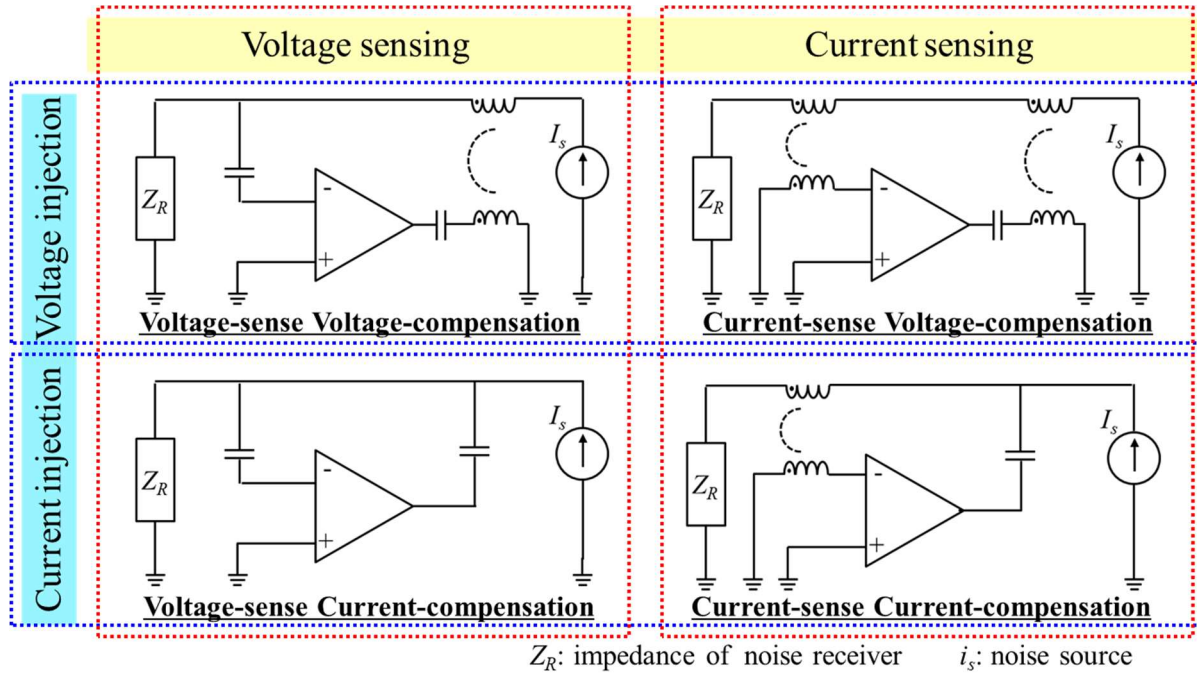


Fig 1-5. The topologies of the Active EMI Filters

Many types of AEFs employing OP-amps have been proposed. The current sense voltage compensation (CSVC) AEF with an OP-amp has been developed in [13]. The loop gain of the AEF were extracted, and the CM conducted emissions attenuated by the AEF has been demonstrated. The concept of the impedance multiplication by the current sense current compensation (CSCC) AEF with an OP-amp has been introduced in [15]. The transformer-less voltage sensing current compensation (VSCC) AEF has been manufactured by designing the OP-amp using several discrete BJTs and diodes in [17], which demonstrates the increased effective capacitance between the power line and the earth GND.

Designing an AEF using the OP-amps provides higher degree of freedom in the amplifier design. Also, the feedback loop gain of the AEF using the OP-amp is easy to solve compared to that using a push-pull amplifier. However, the cost of the OP-amp is higher than a simple push-pull amplifier, and the immunity of the sensitive OP-amp circuits against high voltage transient is difficult to achieve. Since the cost and reliability are critical factors in the house appliance equipment, the AEF using a simple push-pull amplifier is much preferred in those applications.

The AEFs based on a push-pull amplifier for the CM noise reduction in the induction motor system and house appliance have been presented in [19]-[23]. The VSVC AEF with a push-pull amplifier has been proposed in [19], as shown in Fig 1-6, where the supply power for the AEF is directly provided

from the DC link of main power system. The VSVC AEF in [19] captures the CM voltage generated by the motor operation and cancels the CM noise by injecting the compensating signal to the load side. This topology has been improved by changing the turn ratio of the compensation transformer and by using darlington pair push-pull amplifier in [20]. In the VSVC AEF using a push-pull amplifier, the high voltage rating BJTs and high supply voltage are required to generate the sufficient amount of compensating voltage signals.

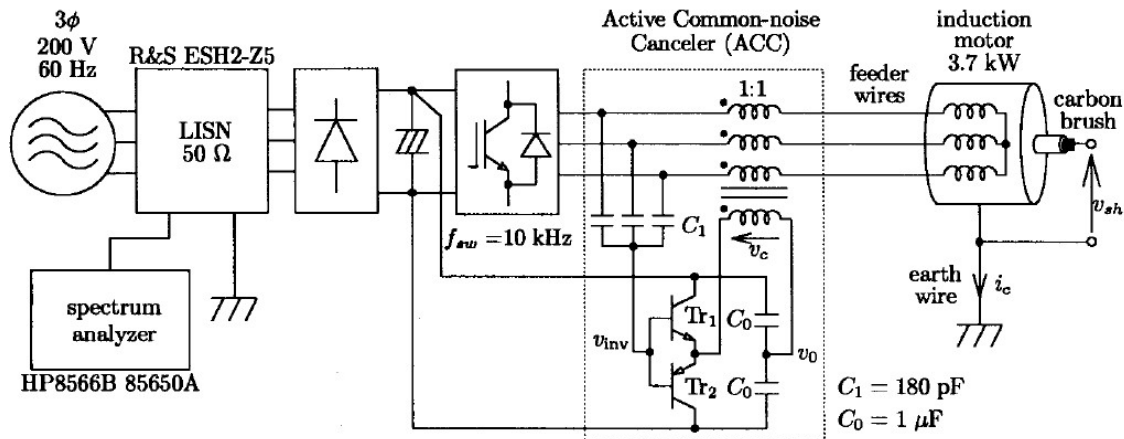


Fig 1-6. The induction motor system configuration with the VSVC AEF in [19]

As shown in Fig 1-7, the CSCC AEF using the push-pull amplifier with the low voltage rating BJTs has been also developed in [23]. The supply for the CSCC AEF has been provided from the dc power of the control board for the inverter. Even with the low-level supply voltage, the CSCC AEF can effectively attenuate the CM conducted emissions if the current gain of the push-pull amplifier is sufficient. All of the active filters in [17]-[21], however, utilize at least one transformer which has a large number of turns for the noise sense or compensation. When the high turns transformer is employed in an AEF, the performance of the active filter can be degraded predominantly due to the parasitic components and/or magnetic saturation of the transformer. Accordingly, an expensive and bulky core transformer is required to avoid the performance degradation.

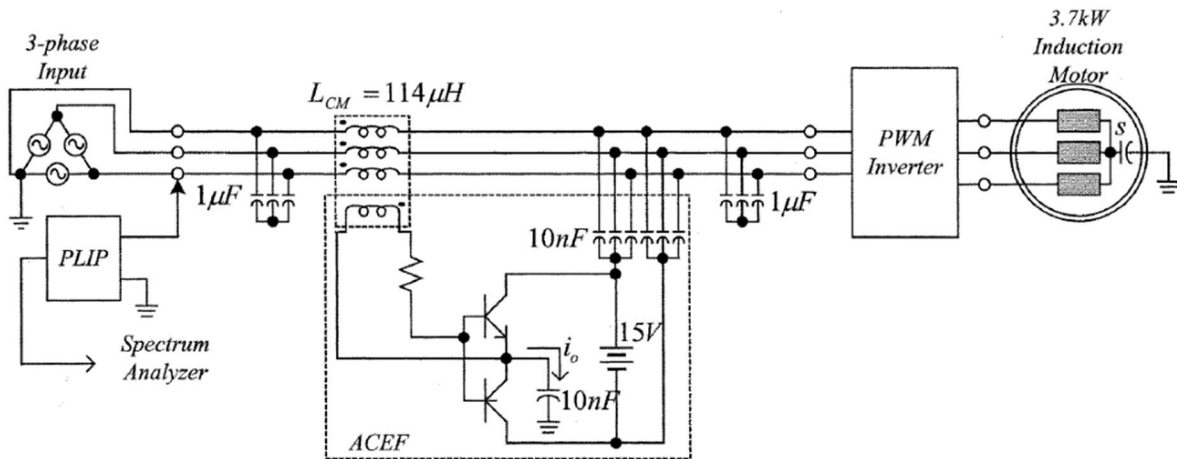


Fig 1-7. The induction motor system configuration with the CSCC AEF in [23]

Another kind of active filters, which generate compensation signals from the digitally controlled signals, has been also proposed in [24]-[28]. The active filters also utilize the push-pull amplifiers, but the inputs to the amplifiers are digitally synthesized based on the direct knowledge of the switching noise pulses, as shown in Fig 1-8. The compensation signal is injected into the power lines through either inductive or capacitive coupling. Although the digital active filter without a transformer can be developed by using only capacitors, the digital control part is much more complicated, expensive, and larger than the analog sensing AEFs.

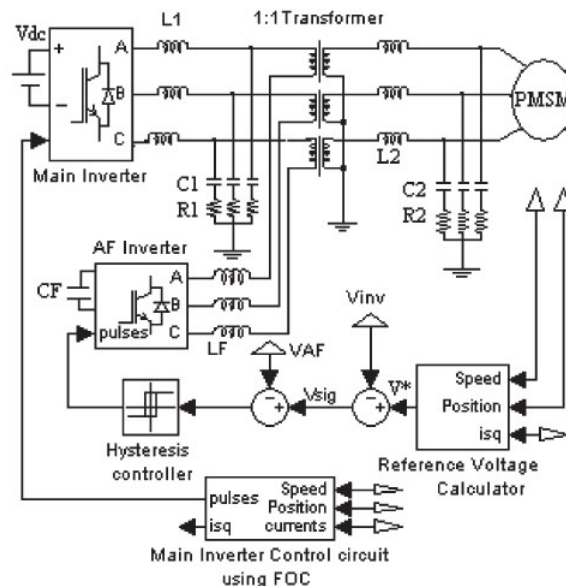


Fig 1-8. The basic structure of the digital AEF in [27]

## 1.4. Objective of This Work

In this thesis, three types of compact AEFs have been proposed to reduce the CM-conducted emissions. The proposed AEFs have been designed as the feed-forward or transformerless configuration to obtain the benefits regarding the size and cost. In the feed-forward configuration, the high noise attenuation can be achieved by using the unity gain amplifier and the transformer with a low number of the turns [29]. Accordingly, the proposed feed-forward AEFs can be manufactured in the compact size, although the transformer is utilized for the noise sense or noise compensation. Each AEF has been rigorously analyzed based on the feedback theory to develop the quantified design guidelines. The developed design guidelines take into account the practical issues related to the performance, stability, and immunity.

In Chapter II, the feed-forward VSVC AEF is composed of the sensing capacitor, injection transformer, and OP amp and analyzed using the half-circuit model regarding the earth GND [16]. The VSVC AEF is manufactured in the compact size by using the proposed design guidelines. The performance of the AEF is explained by the impedance boosting and its loop gain. The power line impedance boosting effect due to the AEF has been validated through the vector network analyzer (VNA). The stability issue in the EMI filter with the AEF has been investigated through the loop gain of the total EMI filter. Furthermore, the limitation of the AEF in regard to the magnetic saturation of the injection transformer has been experientially analyzed.

In Chapter III, the VSCC AEF using the push–pull amplifier has been developed to overcome the degradation of the magnetic saturation [31]. For the analysis, the AEF has been expressed as the equivalent circuit model, and the block diagram of the AEFs has been developed to extract the loop gain. Based on the loop gain, the design guideline of the performance has been established. Also, the stability of the EMI filter has been investigated, and the design rules of the damping circuits have been presented. The protection circuits for the high-voltage transient due to the lightning has been designed for reliability, and the AEF’s immunity against the high-voltage transients is demonstrated by lightning-surge tests.

In Chapter IV, the feed-forward CSCC AEF using the push–pull amplifier has been designed. The sensing transformer with a small number of turns is implemented to avoid the magnetic saturation due to the EUT operating current. The injection capacitors are used for the capacitive coupling between the power lines and the AEF. The EMI filter with the CSCC AEF is designed as the symmetric structure by using the injection capacitors. Based on the equivalent circuit model, a block diagram for the CSCC AEF is constructed. The performance of the AEF is analyzed as the loop gain and

impedance variation. Design rules regarding the performance and the stability are extracted from the loop gain and impedance variation. Also, the asymmetric effects of the EMI filter due to the CSCC AEF have been investigated through VNA measurements. Performance of the AEF is demonstrated through the VNA measurement and the CM-conducted emissions measurement.

## Chapter II

# Analysis and Design of the Feed-Forward Voltage Sensing Voltage Compensation Active EMI filter to Suppress the Common Mode Conducted Emissions

### 2.1. Introduction

A feed forward voltage- sense voltage- compensation (VSVC) CM AEF has been proposed, and manufactured in a compact package. The performance has been demonstrated by installation in a real SMPS board as shown in Fig 2-1. In this topology, the compensation part is fully isolated by the injection transformer, and the touch current at the sensing part is also very small. The VSVC AEF does not need either the high gain amplifier or high turn ratio transformer. The injection transformer with low turn ratio can be implemented in small.

In this chapter, VSVC AEF is analyzed to develop the design and optimization rules. The stability and performance are considered based on the analysis, and the AEF are designed. The performance of the AEF is validated by the vector network analyzer (VNA) and the noise reduction by the AEFs is demonstrated in the conducted emissions experiment.

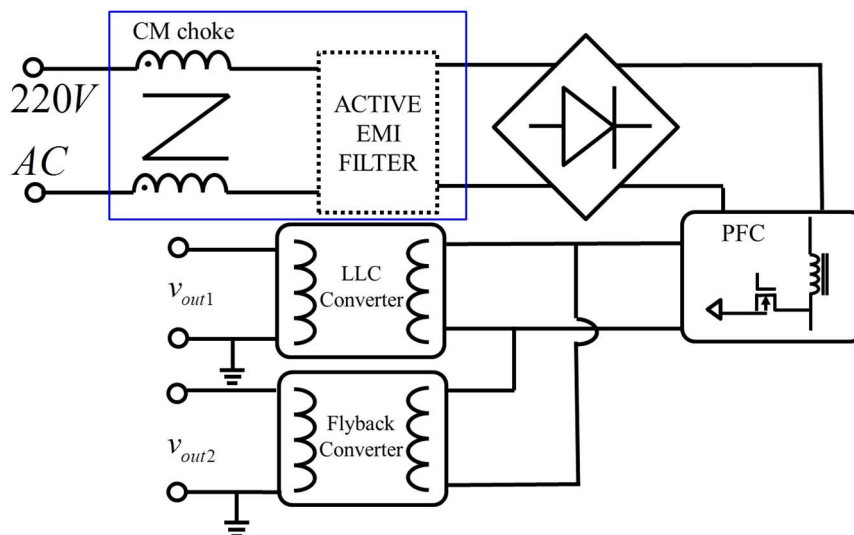


Fig 2-1. An Active EMI filter in a SMPS board



## 2.2. Analysis of Voltage Sensing Voltage Compensation Active EMI Filter

The equivalent circuit model of the feed forward VCVS CM AEF can be depicted, as shown in Fig 2-2 (a). A transformer is installed at the voltage compensation parts and the capacitors are connected to the sensing part. The triangle symbol represents an OP amp, which comprises a low gain inverting amplifier with two resistors  $R_1$  and  $R_2$ . The parasitic resistance and capacitance of the injection transformer are ignored herein for simplicity, however, which will be added later for accurate modeling. The parasitics of the injection transformer only have effects on the high frequency range, and the major operation of the AEF can be well explained and predicted without the parasitics.

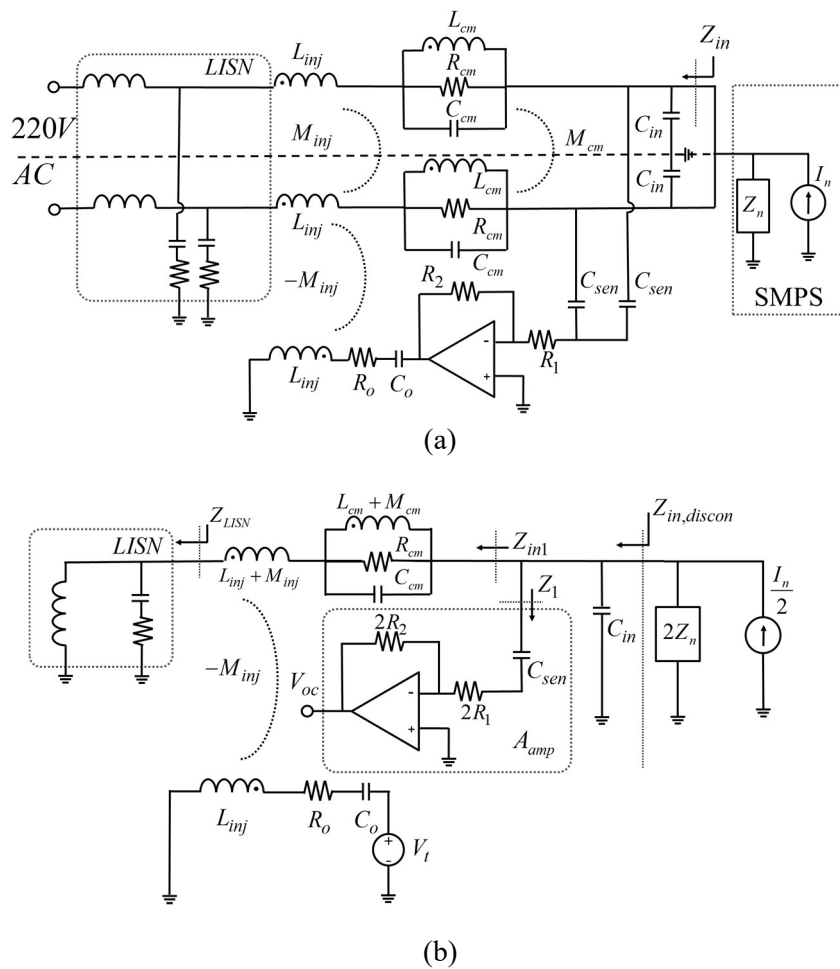


Fig 2-2. (a) Schematic of the VSVC AEF (b) Disconnected circuit model for calculation of the loop gain

The operation of the AEF at the two power lines is symmetric with regard to the earth GND, and



only a half portion can be analyzed. The compensation voltage generated by the AEF output also has recursive effect on the input voltage to the AEF amplifier. The operation of the proposed feed forward AEF can be rigorously analyzed using the feedback theory.

## 2.2.1. Feedback Loop Gain

In analyzing a feedback system, the loop gain is the most important factor in determining the overall gain, input/output impedances, and the system stability. To derive the loop gain, the feedback loop was disconnected at the amplifier output, and a test voltage source has been applied to the disconnected node, as shown in Fig 2-2(b). Only one of the power lines with regard to the earth GND is shown for simplicity.

The loop gain of Fig 2-2 (b) is the ratio of the output voltage  $V_{oc}$  to the test voltage  $V_t$ , which can be solved using the circuit theory as

$$Loop\ Gain = -\frac{V_{oc}}{V_t} = -\frac{Z_1 \parallel \frac{1}{sC_{in}}}{Z_{in1} + Z_1 \parallel \frac{1}{sC_{in}}} A_v \quad (2.1)$$

where

$$Z_{in1} = Z_{L_{cm}} + Z_{L_{inj}} + Z_{LISN}, \quad (2.2)$$

$$Z_{L_{inj}} = s(L_{inj} + M_{inj}) - \frac{2(sM_{inj})^2}{sL_{inj} + R_o + \frac{1}{sC_o}}, \quad (2.3)$$

$$Z_{L_{cm}} = s(L_{cm} + M_{cm}) \parallel \frac{1}{sC_{cm}} \parallel R_{cm}, \quad (2.4)$$

$$Z_1 = \frac{1}{sC_{sen}} + 2R_1, \quad (2.5)$$

$$A_v = -\frac{sM_{inj}A_{amp}}{sL_{inj} + R_o + \frac{1}{sC_o}}, \quad (2.6)$$

$$A_{amp} = \frac{-2A_{op}R_2}{(2R_2 + Z_1) \left(1 + \frac{s}{\omega_{p1}}\right) \left(1 + \frac{s}{\omega_{p2}}\right) + A_{op}Z_1}. \quad (2.7)$$

The  $A_v$  represents the voltage injection gain of the VSVC AEF; and the  $Z_{in1}$  is the impedance looking into the power line at the noise source with the feedback loop disconnected, as shown in Fig

2-2(a). The  $Z_{LISN}$  is the impedance of the noise receiver, such as the line impedance stabilization network (LISN). The  $Z_{Lcm}$  and  $Z_{Linj}$  represent the effective impedances of a CM choke and the injection transformer, respectively. The parasitic capacitance and resistance of the CM choke were also included in the  $Z_{Lcm}$ . The  $A_{amp}$  and  $Z_1$  represent the gain and the input impedance of the inverting amplifier. The  $A_{op}$ ,  $\omega_{p1}$ , and  $\omega_{p2}$  represent the OP amp open loop DC gain, the dominant pole and the non-dominant pole, respectively. The  $C_{in}$  is a small input filter capacitor connected at the side of the noise source. The CM noise source from the SMPS is modeled as a current source  $I_n$  and an impedance  $Z_n$ .

## 2.2.2. Noise Attenuation By Impedance Boosting

The performance of the VSVC AEF is based on the impedance boosting provided by a feedback loop. The input impedance,  $Z_{in,discon}$ , seen at the noise source with the feedback loop disconnected is given as

$$Z_{in,discon} = Z_1 \parallel \frac{1}{sC_{in}} \parallel Z_{in1} \quad (2.8)$$

The input impedance,  $Z_{in}$ , with the feedback loop connected can then be obtained using the loop gain as

$$Z_{in} = Z_{in,discon} \left( \frac{1}{1 + LoopGain} \right) = \frac{\left( Z_1 \parallel \frac{1}{sC_{in}} \right) \frac{Z_{in1}}{1 - A_v}}{Z_1 \parallel \frac{1}{sC_{in}} + \frac{Z_{in1}}{1 - A_v}} = Z_1 \parallel \frac{1}{sC_{in}} \parallel \frac{Z_{in1}}{1 - A_v} \quad (2.9)$$

The equation (2.9) shows that the single power line impedance  $Z_{in1}$ , which is seen from the noise source to the LISN in Fig 2-2(b), is amplified by  $1/(1-A_v)$ . It is also shown that the input impedance of the amplifier  $Z_1$  is connected in parallel with the input filter capacitor  $C_{in}$ . With the voltage injection gain close to 1, most of the CM noise current would flow through the  $Z_1$  and  $C_{in}$ .

The CM noise currents flowing into the LISN without and with the AEF can be expressed respectively as,

$$I_{w/o AEF} = \frac{\frac{1}{sC_{in}} \parallel 2Z_n}{Z_{Lcm} + Z_{LISN} + \frac{1}{sC_{in}} \parallel 2Z_n} I_n \quad (2.10)$$

$$I_{w/AEF} = \frac{Z_1 \parallel \frac{1}{sC_{in}} \parallel 2Z_n}{\frac{Z_{in1}}{1-A_v} + Z_1 \parallel \frac{1}{sC_{in}} \parallel 2Z_n} I_n \quad (2.11)$$

Finally, the noise attenuation ( $NA$ ) factor is calculated as the ratio of the CM currents between the cases with and without the AEF parts.

$$NA = \frac{I_{w/o AEF}}{I_{w/AEF}} = \frac{\frac{Z_{in1}}{1-A_v} + Z_1 \parallel \frac{1}{sC_{in}} \parallel 2Z_n}{\left( Z_{L_{cm}} + Z_{LISN} + \frac{1}{sC_{in}} \parallel 2Z_n \right) \cdot \frac{Z_1}{\frac{1}{sC_{in}} \parallel 2Z_n + Z_1}} \quad (2.12)$$

where the injection transformer has been removed for the case without AEF parts. The  $NA$  of the VSVC AEF is predominantly determined by increase of the term including  $Z_{in1}$ .

### 2.2.3. Stability of the VSVC AEF

The stability analysis is important in the AEF design, since its operation is based on the feedback. The magnitude of loop gain is maximized approximately at the resonance frequency arising from the inductances of CM choke and injection transformer along with the capacitances of  $C_{in}$  and  $C_{sen}$ , since the test voltage,  $V_t$ , is applied to a series connection of ' $Z_1 \parallel 1/(sC_{in})$ ' and ' $Z_{in1}$ ', as shown in Fig 2-2 (b). Also, the phase of the loop gain sharply crosses over -180 degrees at the resonance frequency. When the VSVC AEF is stable, the maximum loop gain at the resonance frequency should be still smaller than 0dB, since the phase is -180 degrees at the frequency. That is, the magnitude of the loop gain for a stable AEF never cross over the 0dB line, and the phase margin cannot be measured. On the other hand, the gain margin can be always and easily found from the gain magnitude at the resonance frequency. Hence, in the design of the VSVC AEF, the gain margin is more suitable to indicate how much stable the system is, although the phase margin is more widely used in checking the stability of a typical feedback amplifier, where the magnitude of loop gain continues to decrease with increasing frequency from a large value at DC. Consequently, the  $GM$  of the AEF is calculated as

$$GM = \frac{1}{|Loop\ Gain|} = \left| \left( 1 + \frac{Z_{Lcm} + Z_{Linj} + Z_{LISN}}{2R_1 \parallel \frac{1}{j\omega_{180}(C_{in} + C_p(\omega_{180}))}} \right) \times \left( \frac{1}{j\omega_{180}C_p(\omega_{180})} \parallel 2R_1 \right) \cdot \frac{R_o + j\omega_{180}L_{inj} + \frac{1}{sC_o}}{j\omega_{180}M_{inj}2R_2} \right| [dB] \quad (\text{at } \omega = \omega_{180}) \quad (2.13)$$

where

$$C_p(\omega) = \frac{C_{sen}}{1 + (2\omega C_{sen} R_1)^2} \quad (2.14)$$

$$\omega_{180} \approx \sqrt{\frac{1}{C_{in}} \frac{1}{(L_{cm} + M_{cm} + L_{inj} + M_{inj})} - \frac{1}{C_{in}} \frac{1}{4C_{sen} R_1^2}} \quad (2.15)$$

In (2.13)-(2.15), the series connection of  $R_1$  and  $C_{sen}$  has been converted to a parallel connection of equivalent resistance and capacitance for effective calculation. The  $C_p(\omega)$  represents the equivalent capacitance of the parallel connection.

## 2.3. Design Guidelines of the VSVC AEF

The design rules for the VSVC AEF is completely analyzed and proposed in this section. It is found that the input filter capacitor, injection transformer, and amplifier output resistance are the most critical in performance and stability of the VSVC AEF.

### 2.3.1. Input Filter Capacitor, $C_{in}$

The impedance of the CM noise source is usually very large in low frequencies since it results from the parasitic capacitance between the switching devices and its heat sink or GND. Without  $C_{in}$ , the noise attenuation factor is written from (2.12) as

$$NA_{w/o\ C_{in}} = \frac{\frac{Z_{in1}}{1 - A_v} + Z_1 \parallel 2Z_n}{(Z_{Lcm} + Z_{LISN} + 2Z_n) \cdot \frac{Z_1}{2Z_n + Z_1}} \quad (2.16)$$

In usual design, the amplifier input impedance  $Z_1$  and the noise source impedance  $Z_n$  are much larger compared to the boosted single power line impedance,  $Z_{in1}/(1-A_v)$ . That is, if  $(Z_1 \parallel 2Z_n) > Z_{in1}/(1-A_v)$ , the  $NA$  in (2.16) is greatly degraded as close to 1, since the  $Z_n$  is also much larger than  $Z_{Lcm}$  and  $Z_{LISN}$  in the low frequency range.

Thus, the input filter capacitor is required to suppress the effect of noise source impedance. By adding the input filter capacitor  $C_{in}$  in parallel with the noise impedance as shown in Fig2-2 (a), the impedance looking into noise source at the power line becomes  $1/(sC_{in}) \parallel Z_1 \parallel 2Z_n$ . If the input filter capacitor is chosen so that  $1/(sC_{in}) \ll (Z_1 \parallel 2Z_n)$ , noise attenuation is simplified as

$$NA_{w/C_{in}} \approx \frac{\frac{Z_{in1}}{1-A_v} + \frac{1}{sC_{in}}}{Z_{Lcm} + Z_{LISN} + \frac{1}{sC_{in}}} \quad (2.17)$$

As the result shown in (2.17), the effect of the large noise source impedance has been removed by employing the input filter capacitor. Finally, the desired range for the input filter can be summarized as

$$(2Z_n \parallel Z_1) \geq \frac{1}{sC_{in}} \geq \frac{1}{sC_Y} \quad (2.18)$$

where  $C_Y$  is the allowable maximum limit of Y-capacitance value.

### 2.3.2. Minimum Operation Frequency $f_o$ , $L_{inj}$ and $R_o$

The injection part consists of the amplifier output resistor  $R_o$ , the DC block capacitor  $C_o$ , and the injection transformer which has the largest portion in the size of the VSVC AEF. From (2.9) and (2.12), the self-inductance of the injection transformer  $L_{inj}$  does not have a significant effect on the overall AEF performance, but the mutual inductance  $M_{inj}$  between the power lines and the amplifier output has a critical impact on the AEF performance. A small change in the mutual inductance can cause a large variation in the voltage injection of (2.6) and therefore the boosting factor,  $1/(1-A_v)$ . In other words, the coupling coefficient ( $k_{inj}=M_{inj}/L_{inj}$ ) significantly influences the overall performance.

With the value of the voltage injection gain  $A_v$  close to 1, the VSVC AEF will show the maximum performance. However, the voltage injection gain varies with frequency. The design goal should be then to achieve the voltage injection gain  $A_v$  close to 1 in the target frequency range. If the DC block

capacitor  $C_o$  is chosen to have negligible impedance in the target frequency range, the voltage injection gain can be rewritten as

$$A_v = -\frac{sM_{inj}A_{amp}}{sL_{inj} + R_o + \frac{1}{sC_o}} \approx -\frac{sM_{inj}A_{amp}}{R_o + sL_{inj}}. \quad (2.19)$$

For convenience, the operation bandwidth of the VSVC AEF is defined as the frequency range where the impedance boosting factor,  $1/(1-A_v)$ , is larger than 2. The voltage injection gain  $A_v$  of (2.19) should be then larger than 1/2 in the operation bandwidth, and the minimum operation frequency,  $f_{op}$ , can be found from the low frequency boundary so that

$$A_v(f_{op}) \approx \frac{2\pi f_{op} M_{inj} A_{amp}}{2\pi f_{op} L_{inj} + R_o} = \frac{1}{2} \quad (2.20)$$

Here, the amplifier gain  $A_{amp}$  can compensate the non-ideal coupling coefficient of the injection transformer ( $k_{inj}=M_{inj}/L_{inj}$ ). Assuming the amplifier gain is designed to be  $|A_{amp}|=(1/k_{inj})=(L_{inj}/M_{inj})$ , the minimum operation frequency is obtained as

$$f_{op} = \frac{R_o}{2\pi L_{inj}} \quad (2.21)$$

From (2.21), once a target minimum operation frequency is set, the relation between  $L_{inj}$  and  $R_o$  is also found.

Now an interesting design guide for the AEF size can be extracted. The necessary self-inductance of the injection transformer predominantly determines its geometrical size, which also occupies most of the total AEF size. For that reason, small inductance is desired for a compact AEF, and then the  $R_o$  also should be small by (2.21) for the given minimum operation frequency.

The impedance of amplifier output, however, should be sufficiently large not to exceed the limit of the supply current for the OP amp as,

$$\frac{V_o}{2\pi f L_{inj} + R_o} \leq I_{\max, OPamp} \quad (2.22)$$

where  $V_o$  and  $I_{\max, OPamp}$  represent the supply voltage and maximum supply current of the OP amp, respectively.

### 2.3.3. Sensing part and Amplifier, $R_1$ , $R_2$ and $C_{sen}$

The sensing part is composed of sensing capacitor  $C_{sen}$  and resistor  $R_1$ . Since the bandwidth of the amplifier is sufficiently wider than the target frequency, the amplifier gain  $A_{amp}$  of (2.7) can be simplified by the ratio of  $R_2$  to the sensing part impedance within the target frequency as

$$A_{amp} \approx -\frac{2R_2}{2R_1 + \frac{1}{sC_{sen}}} \quad (2.23)$$

By the impedance of sensing capacitor, the amplifier gain also varies with the frequency. However, in the operation frequency range, it is required that the amplifier gain  $A_{amp}$  is constant and determined only by  $-(R_2/R_1)$ . Thus,  $R_1$  should be much larger than  $1/sC_{sen}$  even at the minimum operation frequency  $f_{op}$ . A convenient condition can be chosen as

$$R_1 \geq 5 \cdot \frac{1}{2\pi f_{op} C_{sen}}, \quad (2.24)$$

In the condition of (2.24), the amplifier gain  $A_{amp}$  should compensate the non-ideal coupling coefficient, as mentioned in the subsection 2.3.2, as

$$|A_{amp}| \approx \frac{R_2}{R_1} = \frac{1}{k_{inj}} \quad (2.25)$$

Finally, the design rule for  $R_1$  and  $R_2$  can be expressed as

$$R_2 = \frac{R_1}{k_{inj}} \quad (2.26)$$

### 2.3.4. Optimization of Parameters Considering Stability

After designing every parameter using the design rules (2.18), (2.21, 2.22), and (2.24, 2.26), the gain margin should be checked using (2.13) as the last step. It has been found that  $R_1$ ,  $R_2$ , and  $R_o$  are predominantly responsible to the gain margin. For example, in Fig 2-3 (a), the gain margin is plotted according to  $R_1$ , where  $R_2$  also changes with the constant ratio to  $R_1$  from (2.26). All other parameters except for  $R_1$  and  $R_2$  are fixed to the designed values. The gain margin decreases as  $R_1$  increases. As

the minimum operation frequency is rarely affected by  $R_1$ , the smaller  $R_1$  is desired as long as the condition (2.24) is satisfied.

On the other hand, the gain margin is also plotted according to  $R_o$  in Fig 2-3 (b), where all other parameters except for  $R_o$  are fixed to the designed values. The gain margin increases as  $R_o$  increases. However, the minimum operation frequency  $f_{op}$  also significantly increases in proportional to  $R_o$  from (2.21). The value of  $R_o$  should be carefully chosen in optimizing performance and stability of the VSVC AEF, since there is a trade-off relationship between the gain margin and the minimum operation frequency.

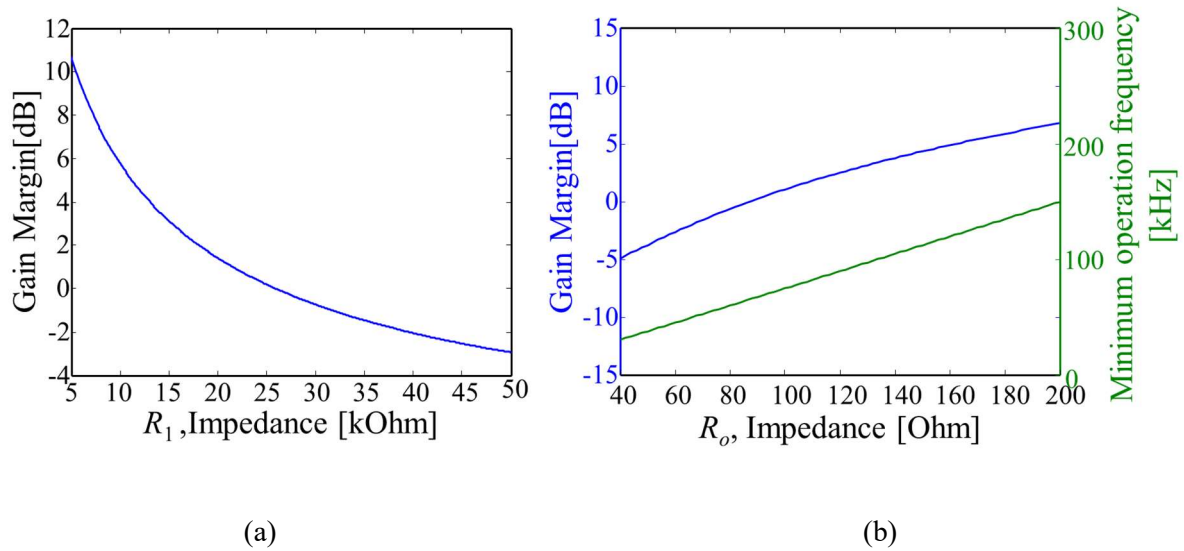


Fig 2-3. (a) Gain margin with variable  $R_1$  (b) Gain margin and minimum operation frequency with variable  $R_o$

The design and optimization flow are summarized in Fig 2-4. The value of each circuit element can be determined from the corresponding design rules. Basically, most design rules have been extracted to meet the target minimum operation frequency in the smallest size. At the final step, the system stability should be confirmed. When the designed AEF violates the stability criterion, the values of  $R_1$  and  $R_o$  should be adjusted in step 2 and step 3 to achieve a positive GM. From Fig 2-3 (a), a smaller  $R_1$  is preferred as long as (2.24) is satisfied. After tuning  $R_1$  into the smallest value at first, the GM can be further increased by increasing  $R_o$ , but it should be carefully adjusted due to the tradeoff between the minimum operation frequency and the GM.



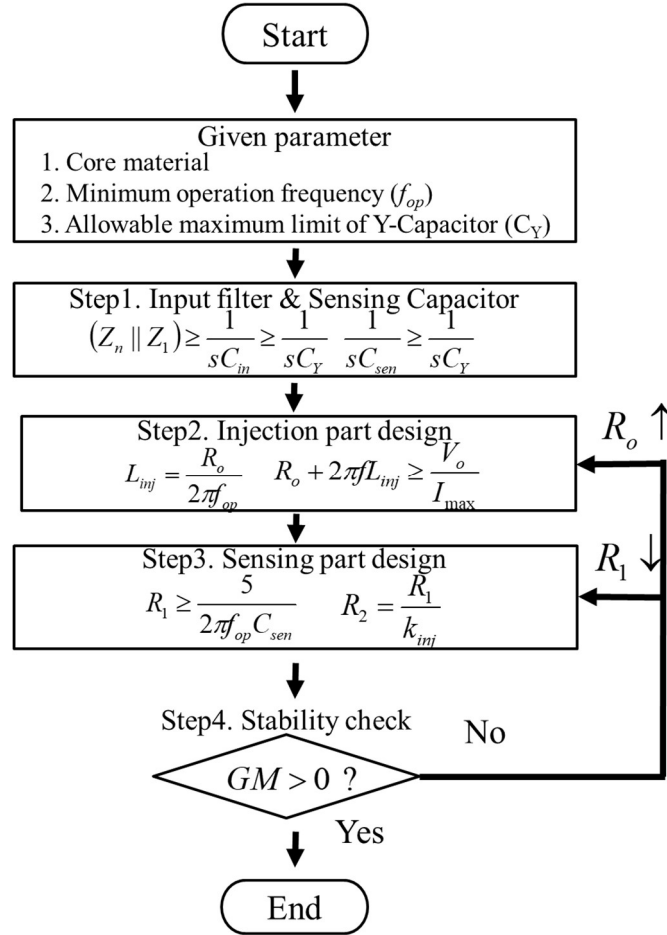


Fig 2-4. Design and optimization flow for the VSVC AEF

## 2.4. Implementation and Validation

In this section, several components used in the VSVC AEF are individually modeled from measurements using the vector network analyzer (VNA). The overall model of the VSVC AEF is then validated as well from the VNA measurements. To verify the CM noise attenuation, the conducted emission is measured in the real SMPS board with the VSVC AEF employed.

### 2.4.1. Characterization of Components

The noise attenuating performance of the VSVC AEF is achieved by boosting the single power line impedance  $Z_{in1}$ , as shown in (2.12). Accordingly, some value of the  $Z_{in1}$  should be maintained. A CM choke can be used to maintain the certain value of power line impedances. The circuit model of a CM choke is approximated as parallel  $R_{cm}$ ,  $L_{cm}$ , and  $C_{cm}$  for each side. The  $L_{cm}$  and  $M_{cm}$  are the self-

inductance and mutual-inductance in a CM choke respectively. The  $R_{cm}$  and  $C_{cm}$  represent the parasitics of a CM choke. It is assumed that the component values at the two sides are identical, since a CM choke should have 1 to 1 winding. From VNA measurements shown in Fig 2-5, all values of the circuit elements have been extracted. The results from the circuit model for CM choke are well matched to the measured results until 10 MHz.

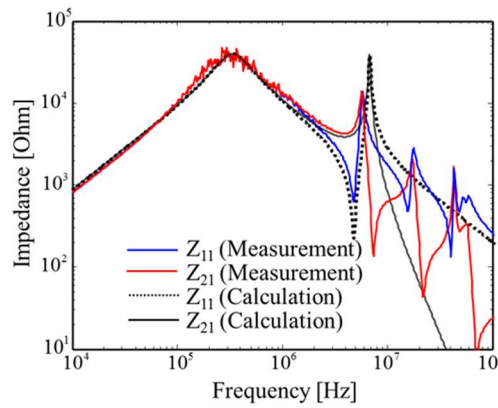
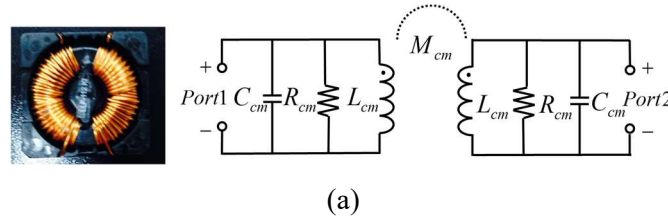


Fig 2-5. Measurements and modeling of the common mode choke (a) the photograph and circuit model ( $L_{cm}=14\text{mH}$ ,  $R_{cm}=80\text{k}\Omega$ ,  $C_{cm}=8\text{pF}$ ) (b) impedance parameters

In the VSVC AEF, the injection transformer has three windings to make the coupling between the amplifier output and the CM current at both power lines. As mentioned in the previous sections, the injection transformer has significant effects on the overall AEF size and the minimum operation frequency. With consideration for both size and minimum operation frequency, the injection transformer has been carefully manufactured using a small ferrite ring with a diameter of 10mm. The number of turns is 9 at each amplifier output and at the two power lines, as shown in Fig 2-6 (a). The injection transformer is also modeled as parallel  $R_{inj}$ ,  $L_{inj}$  and  $C_{inj}$  for each side. The  $R_{inj}$  and  $L_{inj}$  correspond to parasitics in the injection transformer. For simplicity, it is also assumed that component values in all three windings are symmetric due to the same number of turns. In the VNA measurements, only two sides are measured with the other side opened. For accurate validation of both circuit models for the CM choke and injection transformer, the impedance curves are plotted in

the frequency range from 10 kHz to 100 MHz, which is wider than the target frequency range of the designed AEF.

The injection transformer has inductive impedance up to about 10 MHz, as shown in Fig 2-6 (b). Since the injection transformer should provide the compensating signal by mutual inductive coupling, the frequency range of inductive impedance is directly related with the operation bandwidth of the AEF. Thus, it is predicted that the noise attenuation of the VSVC AEF decreases above 10 MHz.

The coupling coefficient can be calculated using the impedance parameters extracted from VNA measurements as

$$\frac{Z_{21}}{\sqrt{Z_{11}Z_{22}}} \approx \frac{M_{21}}{\sqrt{L_{11}L_{22}}} = k \quad (2.27)$$

The equation (2.27) is valid only in the low frequency range where the  $Z_{11}$ ,  $Z_{22}$ , and  $Z_{21}$  has clear inductive impedance curves, and the coupling coefficient is calculated and plotted from 10 kHz to 1 MHz. The extracted coupling coefficients between any two windings are approximated to 0.992.

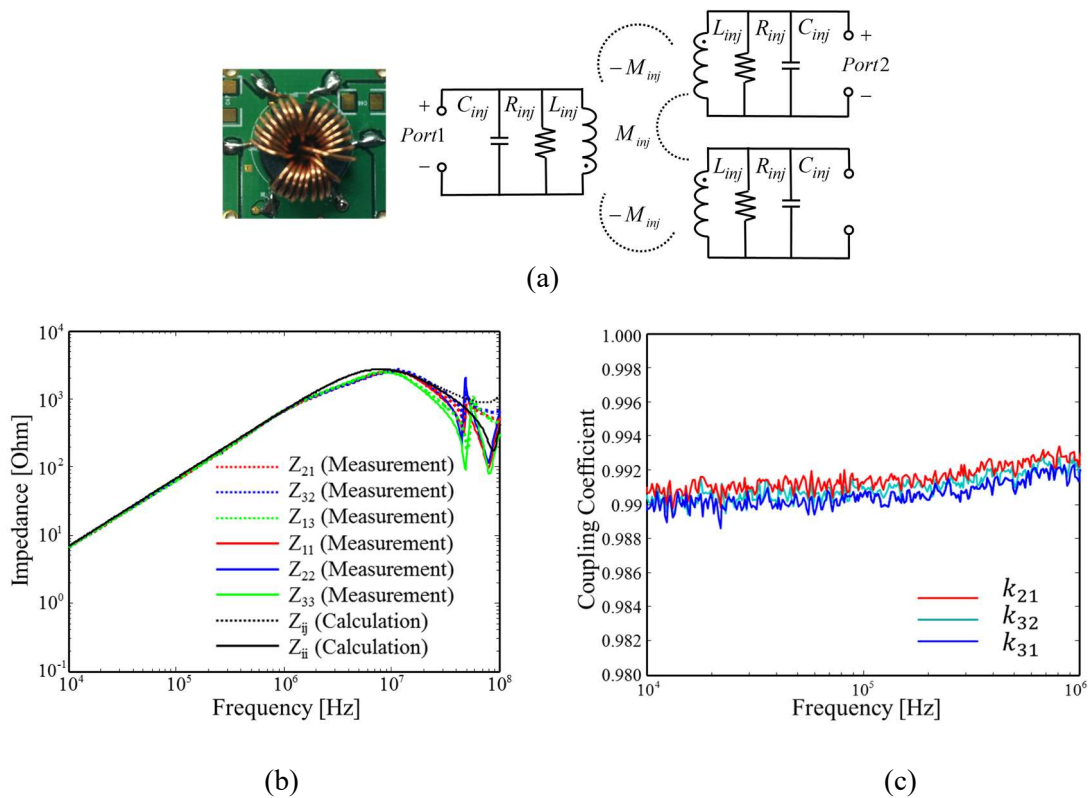


Fig 2-6. Measurements and modeling of the injection transformer; (a) the photograph and circuit model ( $L_{inj}=110\mu\text{H}$ ,  $R_{inj}=5.5\text{k}\Omega$ ,  $C_{inj}=1.8\text{pF}$ ) (b) impedance parameters (c) coupling coefficients extracted from measurements

As an active circuit component, the OP amp has a limited frequency bandwidth and its output is also limited by the supply voltage level. To attenuate the target noise, the output bandwidth should be wider than the target frequency range, and the supply voltage level should be larger than the maximum CM noise level. In this paper, OPA847 was utilized as an inverting amplifier in the VSVC AEF. The OP amp is modeled as a 2-pole system with dominant and non-dominant poles at 10 kHz and 28 MHz, respectively, and the open loop DC gain of 98dB. The input and output sides are connected to each port in the VNA measurement, as shown in Fig 2-7. The measured result agrees well with the simulated result using the circuit model of the amplifier, as shown in Fig 2-7. In addition, the bandwidth of the unity gain amplifier is sufficiently wide to be used for reduction of the low-frequency CM noise.

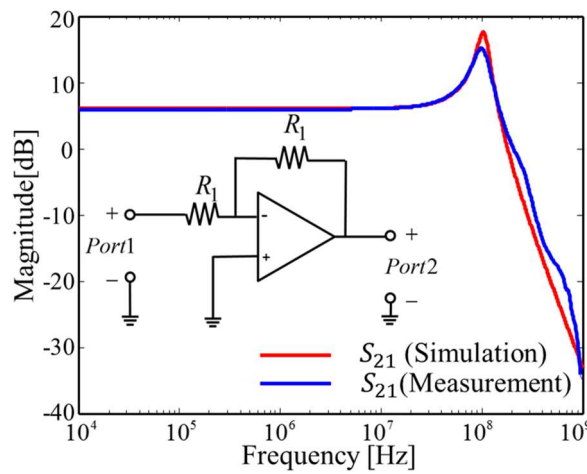


Fig 2-7. Measurements and modeling of the unify gain amplifier ( $R_1=5.6k\Omega$ )

The circuit models of the injection transformer and the amplifier agree well with the measurement up to about 80 MHz and about 1 GHz, respectively. However, since the circuit model of CM choke agrees with the measurements up to just about 10 MHz, the total AEF circuit model would not be accurate above 10 MHz.

## 2.4.2. Designed AEF and Experimental Validation using VNA

The total AEF has been designed and manufactured, and all component values in the AEF are summarized in Table 2-1. The parasitics for the CM choke and the injection transformer have been extracted in 2.3.1.

For more accuracy and better agreements with the measurements, the parasitics of the injection

transformer are also included in the experimental validations. Considering the parasitics of the injection transformer, the loop gain of (2.1) and the feedback input impedance  $Z_{in}$  of (2.9) are modified as

$$\text{Loop Gain} = - \frac{\left( Z_{LISN} + Z_{L_{cm}} + Z_1 \parallel \frac{1}{sC_{in}} \right) \parallel Z_p}{\left( Z_{LISN} + Z_{L_{cm}} + Z_1 \parallel \frac{1}{sC_{in}} \right) \parallel Z_p + Z_{L_{inj}}} \times \frac{Z_1 \parallel \frac{1}{sC_{in}}}{Z_1 \parallel \frac{1}{sC_{in}} + Z_{L_{cm}} + Z_{LISN}} A_{v2} \quad (2.28)$$

$$Z_{in} = Z_1 \parallel \frac{1}{sC_{in}} \parallel \frac{Z_{in1}}{1 - \frac{Z_p}{Z_p + Z_{L_{inj}}} A_{v2}} \quad (2.29)$$

where,

$$A_{v2} = - \frac{Z_p}{R_o + \frac{1}{sC_o} + Z_p} \frac{sM_{inj} A_{amp}}{\left( R_o + \frac{1}{sC_o} \right) \parallel Z_p + sL_{inj}} \quad (2.30)$$

$$Z_p = R_{inj} \parallel \frac{1}{sC_{inj}} \quad (2.31)$$

The  $Z_p$  represents the parasitic impedance of the injection transformer. The magnitude and phase of the loop gain (2.28) with the component values in Table 2-1 are calculated and plotted to confirm the stability, as shown in Fig 2-8. The minimum GM of the designed AEF is about 10 dB at 40 kHz.

Table 2-1. Component Values of The VSVC Active EMI Filter

Components	Value
$C_{sen}, C_o, C_{in}$	1nF, 10 $\mu$ F, 470pF
$R_1, R_2, R_o$	5.6k $\Omega$ , 5.662k $\Omega$ , 130 $\Omega$
$L_{cm}, M_{cm}, R_{cm}, C_{cm}$	14mH, 13.9mH, 80k $\Omega$ , 8pF
$L_{inj}, M_{inj}, R_{inj}, C_{inj}$	110 $\mu$ H, 109 $\mu$ H, 5.5k $\Omega$ , 1.8pF

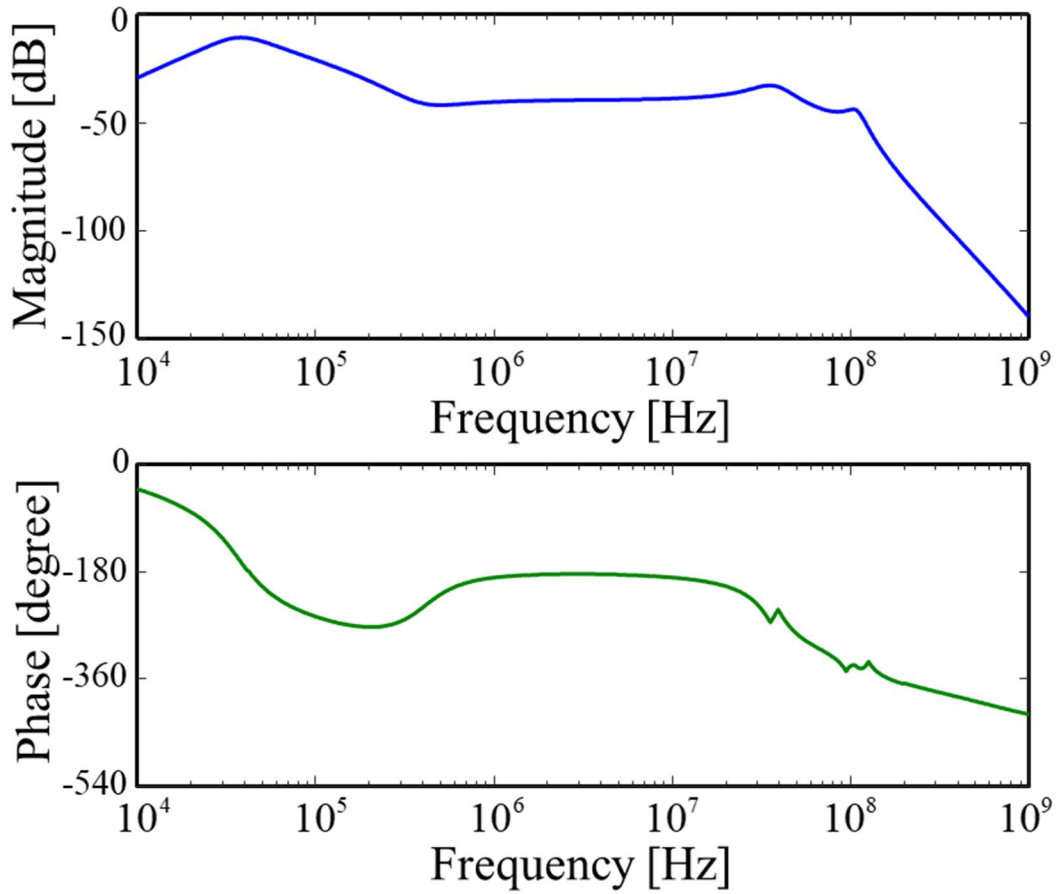


Fig 2-8. The magnitude and phase of the loop gain for the designed AEF

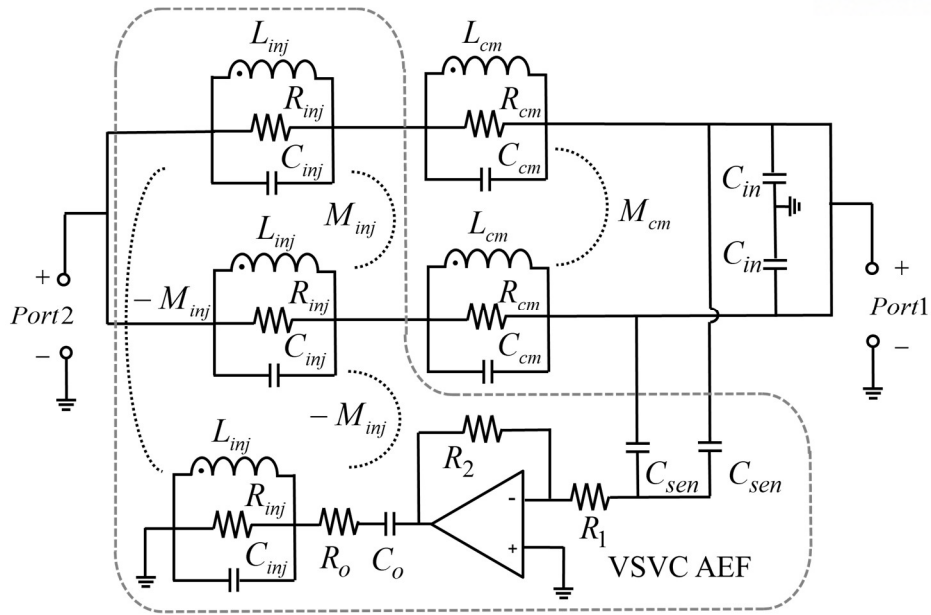
Except that the voltage injection gain is modified to  $A_{v2}$  due to the parasitic impedance of the injection transformer, the overall mechanism is unchanged. The single power line impedance  $Z_{in1}$  is amplified by the boosting factor given as  $(1-(Z_p/(Z_p+Z_{Linj})))A_{v2}$ . To rigorously validate the circuit model of the VSVC AEF and its operation, the impedance of the power line and the transfer characteristics from the noise source to the LISN have been separately calculated, and compared with the measurements. From the feedback input impedance (2.29), it was shown that the VSVC AEF amplifies the  $Z_{in1}$ . The impedance of only the line portion between the LISN and the noise source can be extracted from two-port admittance parameters. If one port is assigned at the noise source and the other assigned at the LISN, as shown in Fig 2-9 (a), the inverse of  $Y_{21}$  parameter corresponds to a half of the single power line impedance, since both power lines are connected in parallel. Without the AEF, the power line between the LISN and the noise source includes only a CM choke and the inverse of  $Y_{21}$  parameter is simply given as

$$\frac{1}{Y_{21}} \Big|_{w/o AEF} = \frac{V_1}{I_2} \Big|_{w/o AEF, V_2=0} = \frac{Z_{Lcm}}{2} \quad (2.32)$$

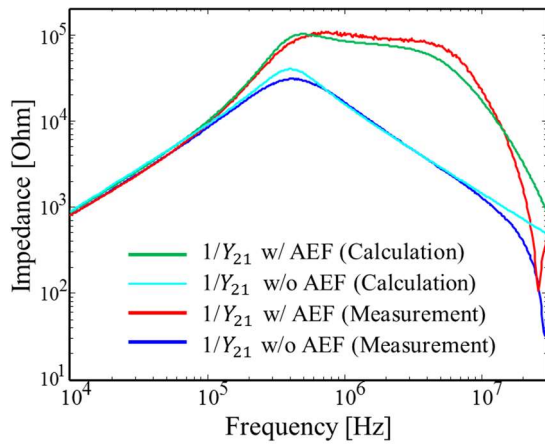
After employing the AEF, the power line impedance including a CM choke and the injection transformer is amplified by  $(1 - (Z_p / (Z_p + Z_{Linj})) A_{v2})$ . The inverse of  $Y_{21}$  parameter is then calculated as

$$\frac{1}{Y_{21}} \Big|_{w/AEF} = \frac{V_1}{I_2} \Big|_{w/AEF, V_2=0} = \frac{1}{2} \frac{Z_{Lcm} + Z_{Linj}}{1 - \frac{Z_p}{Z_p + Z_{Linj}} A_{v2}} \quad (2.33)$$

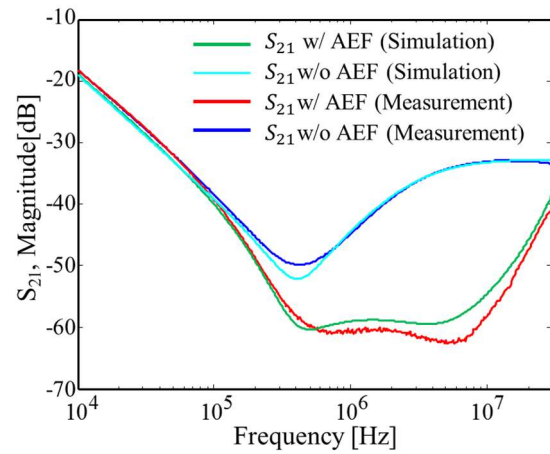
The values of ‘ $1/Y_{21}$ ’ with and without the AEF, given by (2.32) and (2.33), were calculated with the component values in Table 2-1. The measurement and the modeling results of the total AEF are plotted from 10 kHz to 30 MHz in Fig 2-9. As predicted in the section 2.4.1, the modelling results of the total AEF agree quite well with the measurements below 10 MHz. The agreement can be confirmed by the amplitude difference measure (ADM) using the feature selective validation (FSV) technique, which is suggested by the IEEE standard P1597 as a quantitative comparison technique between different datasets [32]-[33]. The associated values of ADM, the GRADE and SPREAD, are the figures of merit for the FSV. The values of GRADE and SPREAD for the  $1/Y_{21}$  with AEF are 3 and 3, respectively. The impedance curves show that the power line impedance is significantly boosted by the VSVC AEF from 100 kHz to 10 MHz. The noise transfer characteristics from the noise source to the LISN can also be investigated from the scattering parameters using the same two-port network in Fig 2-9 (a). The  $S_{21}$  parameter has been calculated and plotted, as shown in Fig 2-9 (c). The agreement of the  $S_{21}$  parameters between the modeling and measurement results is also validated by using the ADM, as GRADE=2 and SPREAD=2. The VSVC AEF greatly reduces the noise transfer characteristics in the target frequency range, and it is then expected that the good  $NA$  would be obtained. Consequently, these experiment results show that the VSVC AEF reduces the signal transmission from 100 kHz to 10 MHz.



(a)



(b)



(c)

Fig 2-9. Calculated and Experiment results (a) Schematic of the two-ports network (b) The  $1/Y_{21}$  between LISN and the noise source with and without the AEF (c)  $S_{21}$  parameter with and without the AEF

### 2.4.3. Conducted Emissions Measurement



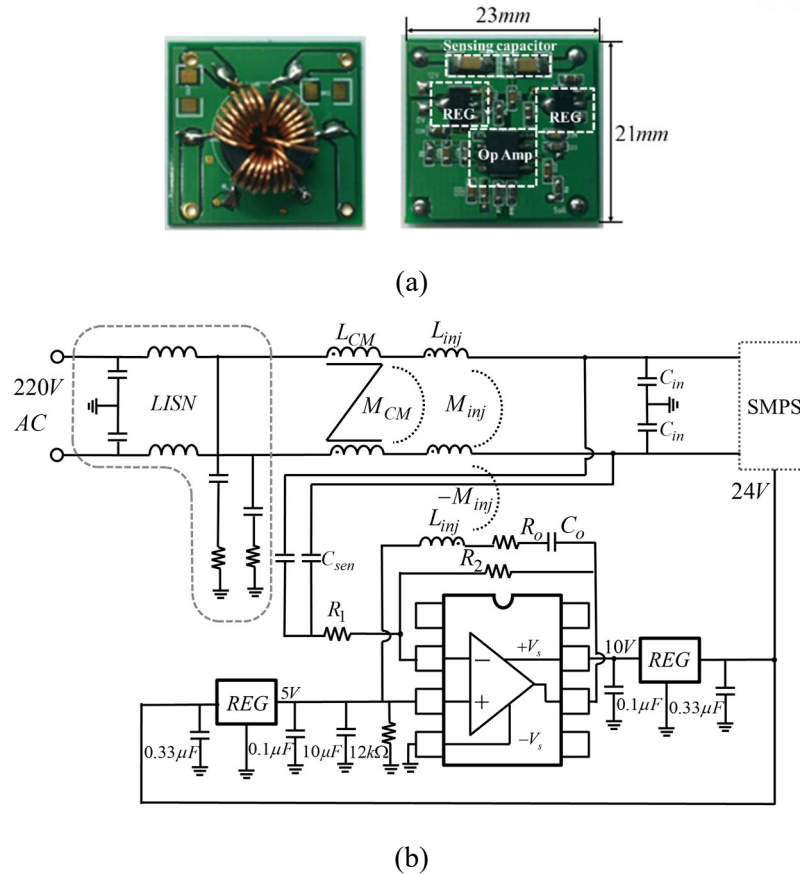


Fig 2-10. (a) Photograph of the implemented AEF in a compact package (b) Schematic of the implemented AEF

The design target is implementing the AEF in a compact package with the good CM noise attenuation in the frequency range from 150 kHz up to 10 MHz. The schematic and photos of the VSVC AEF are shown in Fig 2-10 (a) and (b). To implement the VSVC AEF in the SMPS, two voltage regulators are inserted to convert one of the SMPS dc output into the 10V and 5V for the supply of OP amp. In the VSVC AEF, 10V, 5V and 0V play roles of the supply voltages as potentially positive supply, GND, and negative supply.

The CM conducted emissions according to the CISPR16-1 were measured in the 200W SMPS board with the VSVC AEF installed, as shown in Fig 2-11 (a). The measurement setup consists of the LISN, CM/DM noise separator and spectrum analyzer. In this measurement, only CM noise is measured since the VSVC AEF was designed for CM noise reduction. The target SMPS board includes various power circuits, such as rectifier, power factor correction, Flyback converter, and LLC resonance converter. The switching frequencies used in the power circuits are 64 kHz and 110 kHz,

which are the main sources of the conducted and radiated emissions. As shown in Fig 2-11 (b), the conducted emission of the SMPS with the original three-stages CM chokes was measured, and compared to that with only one CM choke. After employing the AEF in addition to one CM choke, Fig 2-11 (c) shows that the conducted emission is attenuated by 10 dB to 12 dB from 150 kHz to 10 MHz compared to the case with one CM choke. The noise attenuation with the AEF and one CM choke is comparable to the case with three-stage CM chokes in the target frequency, although the size is reduced by 50% as compared with the three-stage CM chokes. Therefore, the VSVC AEF can contribute to reduce the total size and weight of a SMPS.

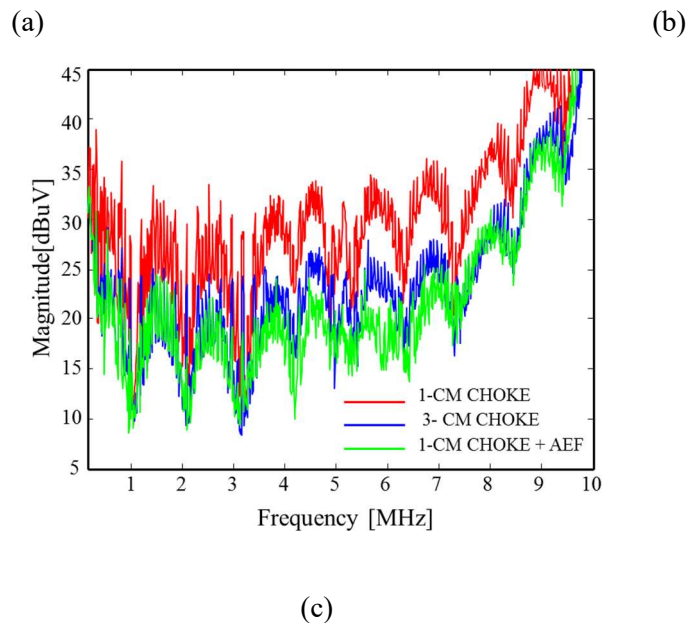
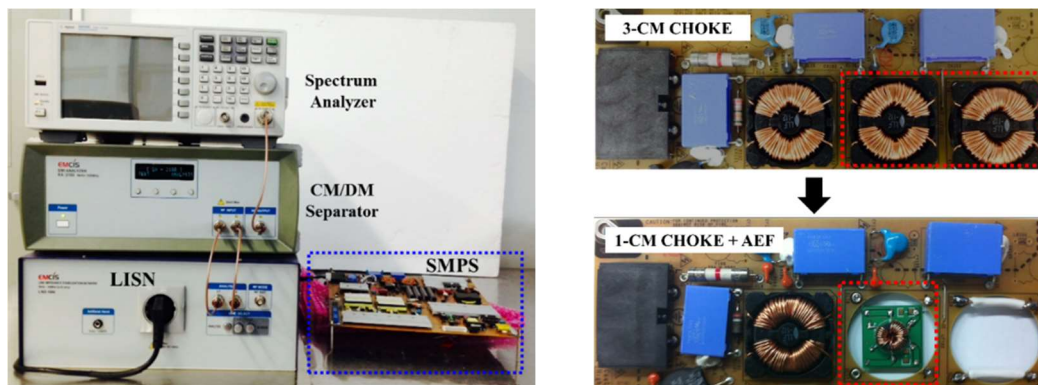
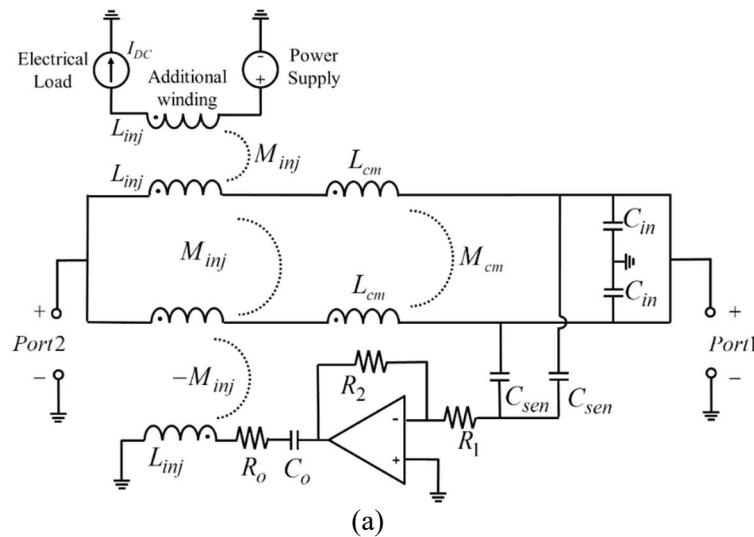


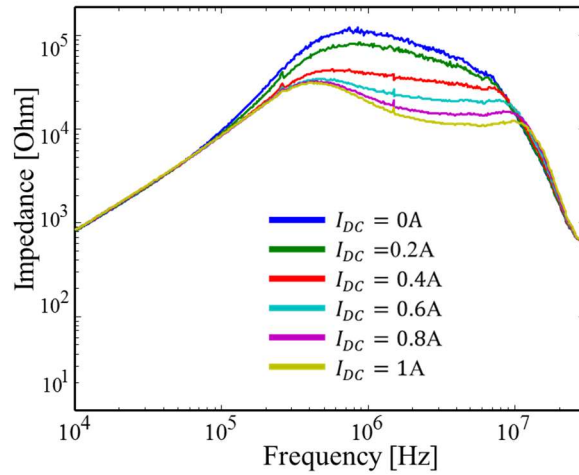
Fig 2-11. (a) The conducted emission measurement setup (b) Photograph of the AEF installed in the real SMPS board (c) Measured CM conducted emissions in the real SMPS board

### 2.4.4. Performance Degradation Due to Magnetic Saturation

Although the VSVC AEF attenuates the conducted emission about 10~12 dB in the SMPS board, the amount of noise reduction is still smaller than that shown in the  $S_{21}$  measurement of Fig 2-9 (c). The reason of the performance degradation is investigated herein. One of reasons for the performance degradation can be explained based on the magnetic saturation effect. In the practical SMPS board, the operation currents at both power lines are not fully balanced. Accordingly, their fluxes caused by each line current does not perfectly cancel out each other. The remaining flux due to the unbalance cause the magnetic saturation in the injection transformer [4]-[5]. With the core saturation, the incremental permeability is greatly decreased, resulting in the decrease of the small signal self- and mutual- inductances of injection transformer. The coupling coefficient is also significantly decreased, since the mutual-inductance decreases more. The decreased coupling coefficient degrades the voltage injection gain and the overall performance of noise attenuation from (2.6) and (2.12). As a result, the noise reduction in the real SMPS board is less than those in the measurements using VNA.

To verify the effect of core saturation experimentally, another winding was added in the injection transformer, and a certain amount of current is drawn through the winding using an electric load, as shown in Fig 2-12 (a). The dc current from the electrical load,  $I_{DC}$ , creates the unbalanced flux in the injection transformer, which can cause magnetic saturation. The amount of core saturation can be adjusted by controlling  $I_{DC}$ . With the adjustment of the  $I_{DC}$ , the  $1/Y_{21}$  with the AEF was measured by VNA. With increasing  $I_{DC}$ , the impedance booting decrease, as shown in Fig 2-12 (b). From these results, it is expected that the performance of the VSVC AFE could be improved by employing a core with less magnetic saturation for the injection transformer.





(b)

Fig 2-12. Experiments to verify the effect of core saturation (a) schematic of the AEF with an additional winding connected to the electrical load (b) the  $1/Y_{21}$  with the AEF by varying the additional current

There is another possible reason of the performance degradation due to the AEF grounding impedance. The GND of the designed AEF is connected to the SMPS GND through a conductor wire, which has predominantly parasitic inductance,  $L_g$ , as shown in Fig 2-11 (a). The  $V_{sen}$  and  $V_g$  represent the sensed CM noise voltage with regard to SMPS GND and the voltage across the wire between SMPS and AEF GNDs, respectively. The  $V_{out}$  represents the amplifier output voltage with regard to the AEF GND. The CM current, which flows along the dashed grey line from the sensing nodes to the SMPS GND, is predominantly responsible for the voltage across the GND inductance  $L_g$ . To analyze the effect of the  $L_g$  on the AEF performance, the common-mode amplifier gain with including the effect of  $L_g$ ,  $A_{amp\ w/wire}$ , has been solved from the ratio of the  $V_{out}$  to the  $V_{sen}$ , as

$$A_{amp\ w/wire} = \frac{V_{out}}{V_{sen}} = \frac{Z_1 + 2R_2}{Z_1 + 2R_2 + 2sL_g(1 - A_{amp})} A_{amp} \quad (2.34)$$

where the expressions for  $Z_1$  and  $A_{amp}$  are already given in (2.5) and (2.7).

It is shown from (2.34) that the  $L_g$  causes the difference between  $A_{amp\ w/wire}$  and  $A_{amp}$ . The deviation of  $A_{amp\ w/wire}$  from  $A_{amp}$  due to the  $L_g$  causes the degradation of AEF performance, since the boosting factor,  $1/(1-A_v)$ , is affected. With varying the value of  $L_g$ , the  $1/Y_{21}$  with the AEF of (2.33) is calculated and plotted in Fig. 2-13 (b). The bandwidth of the proposed AEF decreases with increasing the value of  $L_g$ . The value of  $L_g$  in the designed AEF has been approximately modeled as 0.1  $\mu$ H, which results in further degradation of the AEF performance

above several MHz. As results, in the conducted emission measurement, the CM noise above 10 MHz is little attenuated by the designed AEF.

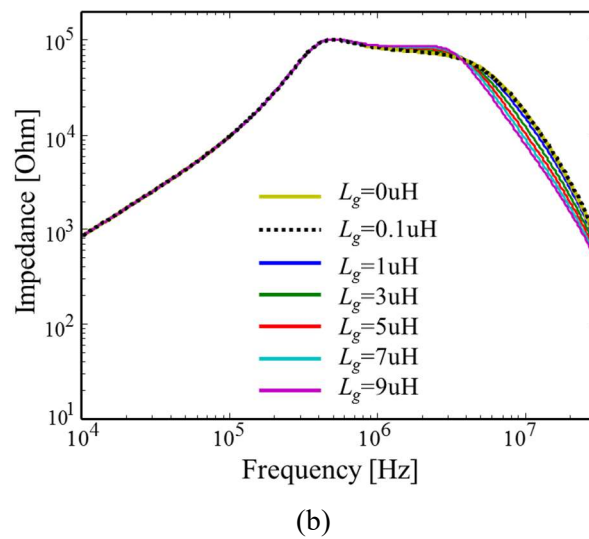
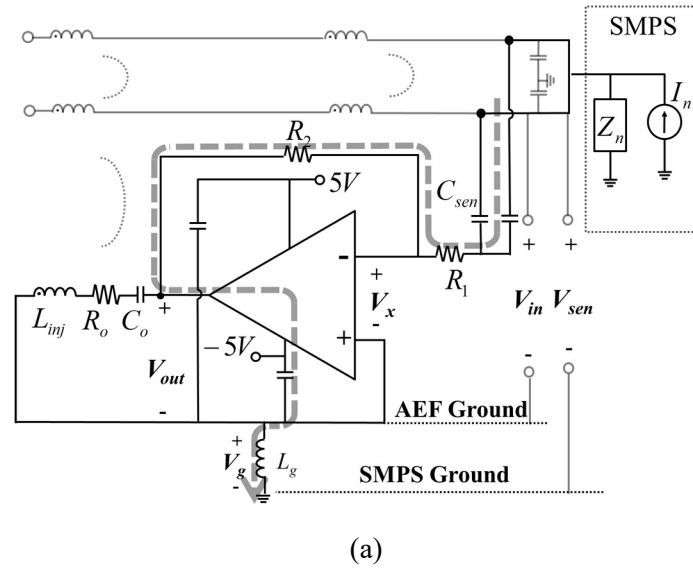


Fig 2-13. (a) the schematic of the VSVC AEF with grounding inductance  $L_g$  (b) the  $1/Y_{21}$  with the AEF by varying the  $L_g$

## 2.5. Summary

A voltage-sense voltage-compensation active (VSVC) EMI filter in the feed forward type has been proposed to achieve good CM noise attenuation in a compact package. The VSVC AEF has been

rigorously analyzed based on feedback theory. Based on the analytical expressions considering both stability and performance, the design and optimization rules for the VSVC AEF have been presented. By using the design rules, the VSVC AEF has been manufactured and optimized. For more accurate design and analysis, each component in the VSVC AEF has been characterized by VNA. Also, the performance of the VSVC AEF was validated in the frequency domain measurements using VNA. Finally, the VSVC AEF installed in the SMPS board attenuates the CM conducted emission by about 10~12dB from 150 kHz to 10 MHz. The noise attenuation with the VSVC AEF and one CM choke is comparable to the case with three-stage CM chokes in the target frequency range, although the size is reduced by 50% as compared with the three-stage CM choke. Furthermore, the VSVC AEF performance degradation due to the magnetic saturation and the grounding impedance has been analyzed and investigated.

## Chapter III

# Quantified Design Guidelines of Compact Transformerless Active EMI filter for Performance, Stability, and High Voltage Immunity

### 3.1. Introduction

The Voltage Sense Current Compensation (VSCC) AEF using a simple push-pull amplifier without any transformers has been proposed in [30] for the first time. As compared to the VSCC AEF with OP-amp in [17], the VSCC AEF using a push-pull amplifier is implemented with much less transistors. The VSCC AEF using a push-pull amplifier can be manufactured in a smaller size than the AEFs with the transformer in [19]-[23]. Also, differently from the AEFs in [19]-[23], the VSCC AEF can provide a sufficient noise reduction even under a low-level supply voltage, and low-cost BJTs with a low-voltage rating can be employed. The low-level supply voltage for the AEF is provided from the dc power of the control board for the main power system.

The AEF can be used alone, but it would more likely be used together with other filter components. Fig 3-1(b) demonstrates a usage example, where the AEF replaces the Y-capacitor of the total filter shown in Fig 3-1(a). Although the circuit analysis of the VSCC AEF has been conducted and its loop gain was derived in [30], it cannot be used in the stability analysis of real applications, since other components in the total EMI filter, such as CM chokes, also significantly affect the overall system stability. In addition, to apply the VSCC AEF to real industrial and commercial products, the immunity against the high voltage transient should be tested and guaranteed.

This chapter completely analyzes the compact transformer-less AEF using a push-pull amplifier. Quantified design guidelines are then rigorously derived from the analysis with consideration for performance and stability. For practical applications, the design rules of protection circuits against the high voltage transient are also proposed. Based on the developed design guidelines, the VSCC AEF is manufactured and employed in the L-C-L EMI filter structure, as shown in Fig 3-1(b). The performance of the VSCC AEF is validated by measurements using a vector network analyzer (VNA). The AEF is applied to a real 2.2 kW current resonant inverter, and the conducted emissions are reduced by 5 dB to 25 dB at the frequency range from 150 kHz to 6 MHz. Also, the immunity of the VSCC AEF against high voltage transients is verified by lightning surge tests.



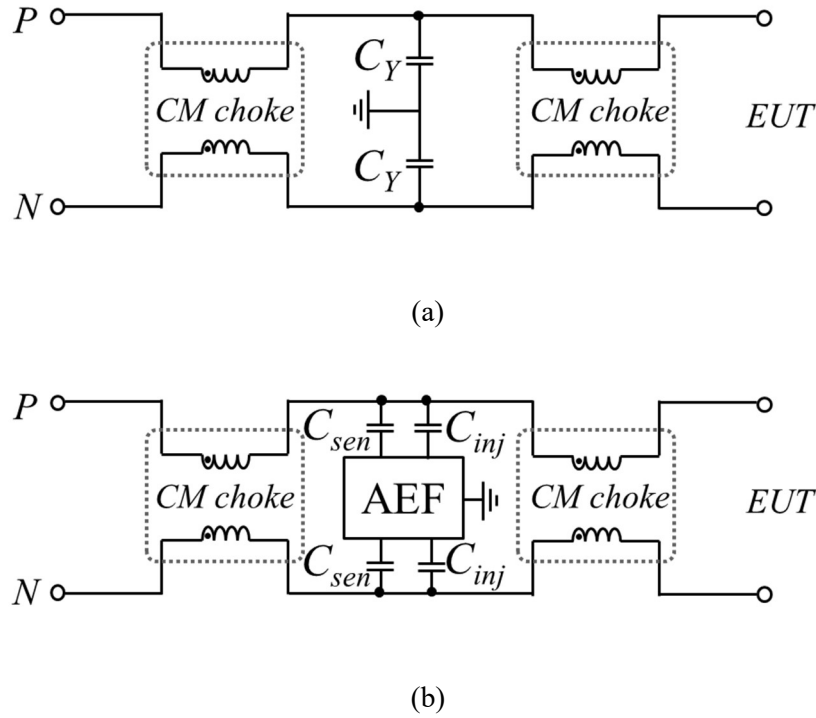


Fig 3-1. (a) A typical CM EMI filter with passive L-C-L configuration (b) The transformerless AEF employed in the the filter configuration

### 3.2. Analysis of the EMI Filter with the VSCC AEF

In this section, the EMI filter with the compact transformer-less AEF is proposed and completely analyzed.

#### 3.2.1. Circuit Model of the Total EMI Filter with the VSCC AEF

The complete circuit model of the proposed L-C-L EMI filter is described in Fig 3-2, where the AEF plays a role as a Y-capacitor. For accurate analysis up to several tens of MHz, the CM chokes are modeled as parallel impedances of  $L_{cm1}$ ,  $M_{cm1}$ ,  $R_{cm1}$ , and  $C_{cm1}$  ( $L_{cm2}$ ,  $M_{cm2}$ ,  $R_{cm2}$ , and  $C_{cm2}$ ), as shown in Fig 3-2. They represent the self-inductance, mutual inductance, equivalent parallel resistance, and equivalent parallel capacitance in the CM chokes, respectively. Additional input filter capacitors,  $C_{inp}$ , are located between CM chokes to suppress the effects of the EUT impedance on the AEF operation. Two X-capacitors,  $C_X$ , are also placed to reduce the differential noises from the EUT.  $I_n$  represents the common mode noise current generated by the EUT. The VSCC AEF block can be divided into the sensing part, the injection part, the amplifier, and the damping circuits. The noise voltage is captured



by the sensing capacitors,  $C_{sen}$ , and applied to the amplifier input. The compensation currents, which are generated by the amplifier, flow into the power lines through the injection capacitors ( $C_{inj}$ ). The push-pull amplifier in the AEF is designed as a class AB amplifier with the output load of  $R_L$  and  $C_L$ . A DC source  $V_{DC}$  are supplied as the power supply for the amplifier. The AC utility voltage and the noise from the EUT can be coupled to the DC supply of the AEF, which can lead to a bias distortion and malfunction of the AEF. Also, if the AEF supply is provided from a control board inside the application product, it can remove the proper isolation between control and power sections. However, after adding the bulk decoupling capacitor,  $C_{DC}$ , with the value of a few  $\mu F$ , the coupled noise voltage is greatly reduced, and the AEF operates properly. The decoupling capacitor is an essential component in the AEF circuit. The BJTs in the amplifier are biased by the resistors,  $R_{bias}$  and  $R_p$ . The degeneration emitter resistors,  $R_e$ , are also added to stabilize the bias. The DC block capacitors,  $C_b$ , are connected in series between the sensing part and the amplifier input to mitigate the electric overstress (EOS) that might be caused by large DC voltage differences. The output current of the VSCC AEF affects the input voltage, and therefore the AEF is a feedback system. For feedback stability, damping circuit elements are added to the input side of the push-pull amplifier. The  $R_{in}$  and  $C_{in}$  in parallel are located between  $C_{sen}$  and  $C_b$ . Also, the  $C_f$ ,  $R_f$ , and  $L_f$  comprise another damping branch from the  $C_{sen}$  to the  $R_e$ . The necessity and behavior of the damping circuits will be analyzed in detail in Section 3.4.

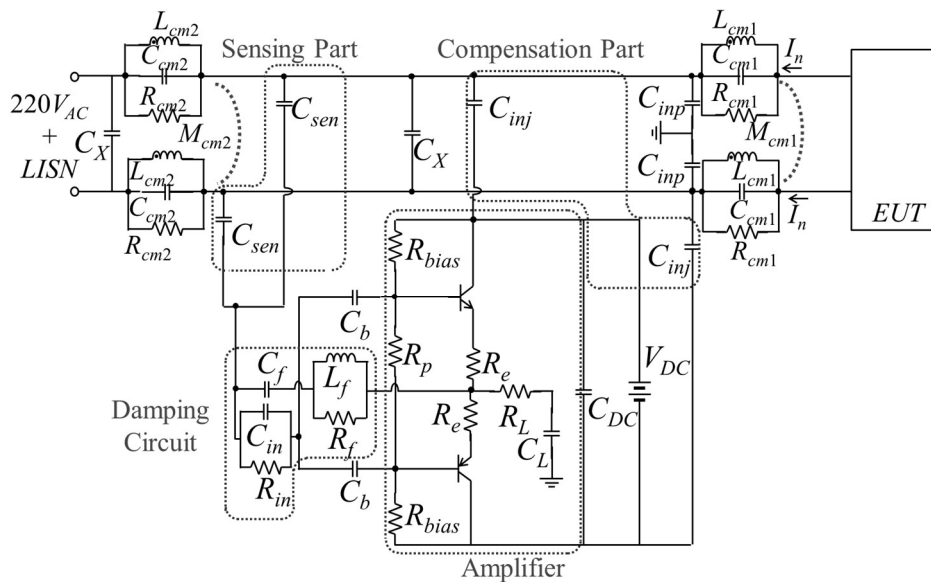
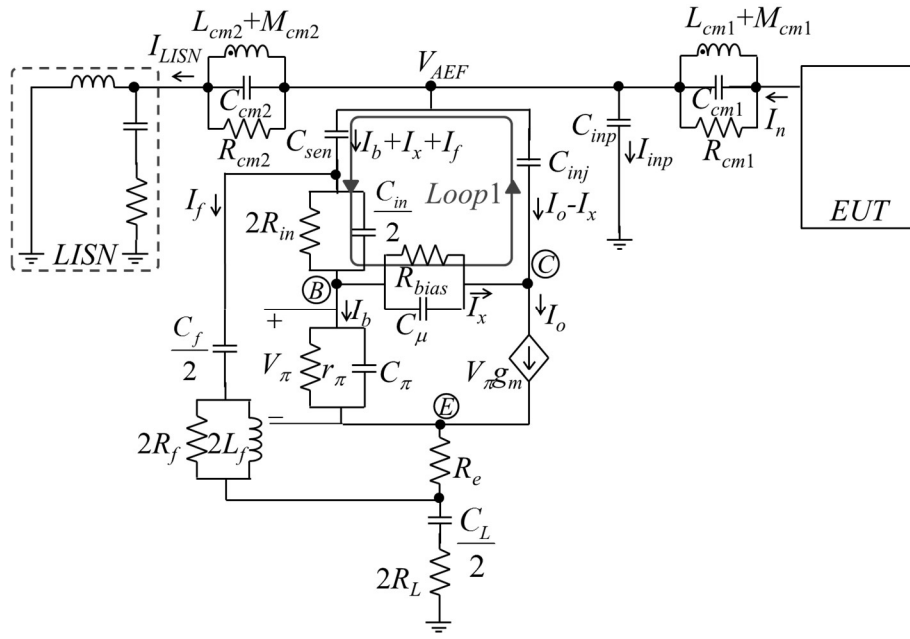


Fig 3-2. Schematics of the L-C-L EMI filter with the VSCC AEF

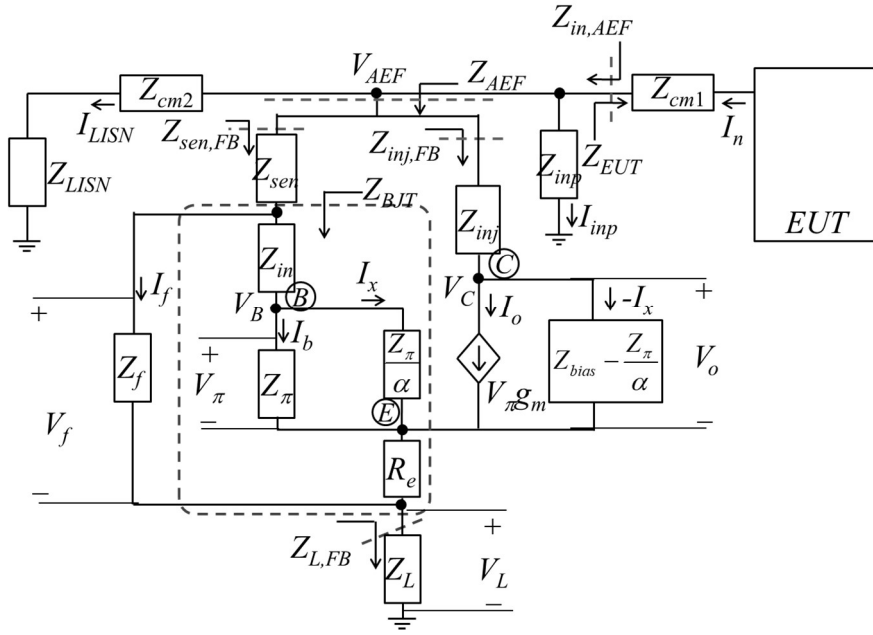
### 3.2.2. Circuit and Block Diagram Analysis

The performance and stability of the EMI filter in Fig 3-2 can be accurately investigated using a detail circuit analysis. The loop gain is the most important factor when analyzing a feedback system. In extracting the loop gain, the circuit analysis should be conducted with consideration for all components in the total EMI filter, since all the components affect the system's stability. The expressions of the circuit model are then converted a block diagram, where the loop gain can be effectively extracted.

The VSCC AEF is predominantly symmetric regarding the earth GND and can be analyzed by using only half of the circuits. The equivalent circuit model of the half portion was developed by applying the small signal model of a BJT, as shown in Fig 3-3(a). The small signal model of a BJT consists of  $r_\pi$ ,  $C_\pi$ ,  $C_\mu$ , and  $g_m$ , which correspond to the input resistance, base-emitter capacitance, base-collector capacitance, and transconductance, respectively.  $I_b$ ,  $I_x$ ,  $I_o$ ,  $I_f$ ,  $I_{inp}$ , and  $I_{LISN}$  represent the base current, the current flowing through  $R_{bias}$  and  $C_\mu$ , the collector current, the current flowing through a damping branch, the current flowing to  $C_{inp}$ , and the current flowing through the line impedance stabilization network (LISN), respectively. The  $V_\pi$  represents the voltage between the base and emitter of the BJT, and the  $V_{AEF}$  represents the noise voltage at the node where the AEF part is connected.  $V_B$  and  $V_C$  indicate the node voltages at base and collector, respectively.



(a)



(b)

Fig 3-3. (a) The equivalent circuit model of the EMI filter with AEF (b) The circuit model after applying the miller's theorem

By applying the KVL along Loop1 in Fig 3-3(a), the ratio of  $I_x$  to  $I_b$ , which is designated as  $\alpha$ , is derived as

$$\frac{I_x}{I_b} = \alpha = \frac{Z_{inj} Z_{\pi} g_m - Z_{sen} - Z_{in} - \frac{Z_{sen}}{Z_f} (Z_{in} + Z_{\pi} + R_e (1 + Z_{\pi} g_m))}{Z_{sen} + Z_{in} + Z_{bias} + Z_{inj} + \frac{Z_{sen}}{Z_f} Z_{in}} \quad (3.1)$$

Where

$$Z_{inj} = \frac{1}{sC_{inj}}, \quad Z_{sen} = \frac{1}{sC_{sen}}, \quad Z_{\pi} = r_{\pi} \parallel \frac{1}{sC_{\pi}}, \quad Z_{in} = 2R_{in} \parallel \frac{2}{sC_{in}},$$

$$Z_{bias} = R_{bias} \parallel \frac{1}{sC_{\mu}} \approx R_{bias}, \quad Z_f = \frac{2}{sC_f} + 2R_f \parallel 2sL_f$$

For simplification, the internal feedback path through  $R_{bias}$  and  $C_{\mu}$  can be disconnected using parameter  $\alpha$ , based on the miller theorem, as shown in Fig 3-3(b). That is, the impedance,  $Z_{\pi}/\alpha$ , is connected between the base and emitter, while the impedance,  $Z_{bias} - Z_{\pi}/\alpha$ , is connected between the collector and emitter. Each current and voltage can be expressed as a function of the  $V_{AEF}$  as,

$$I_n = (I_b + I_x + I_f) + (I_o - I_x) + I_{LISN} + I_{inp} \quad (3.2)$$

$$V_\pi = \frac{Z_f \parallel Z_{BJT}}{Z_{sen,FB}} \frac{Z_\pi \parallel \frac{Z_\pi}{\alpha}}{Z_{BJT}} V_{AEF} \quad (3.3)$$

$$I_b + I_x = \frac{V_\pi}{Z_\pi \parallel \frac{Z_\pi}{\alpha}} = \frac{Z_f \parallel Z_{BJT}}{Z_{sen,FB} Z_{BJT}} V_{AEF} \quad (3.4)$$

$$I_o = V_\pi g_m = \frac{Z_f \parallel Z_{BJT}}{Z_{sen,FB}} \frac{Z_\pi \parallel \frac{Z_\pi}{\alpha}}{Z_{BJT}} g_m V_{AEF} \quad (3.5)$$

$$I_x = \frac{Z_f \parallel Z_{BJT}}{Z_{sen,FB}} \frac{Z_\pi \parallel \frac{Z_\pi}{\alpha}}{Z_{BJT}} \frac{\alpha}{Z_\pi} V_{AEF} \quad (3.6)$$

$$I_f = \frac{Z_f \parallel Z_{BJT}}{Z_{sen,FB}} \frac{1}{Z_f} V_{AEF} \quad (3.7)$$

$$I_{inp} + I_{LISN} = \frac{V_{AEF}}{Z_{inp} \parallel (Z_{cm2} + Z_{LISN})} \quad (3.8)$$

where

$$Z_{inp} = \frac{1}{sC_{inp}} \quad (3.9)$$

$$Z_{cm2} = s(L_{cm2} + M_{cm2}) \parallel \frac{1}{sC_{cm2}} \parallel R_{cm2} \quad (3.10)$$

$$Z_{sen,FB} = \frac{V_{AEF}}{I_b - I_x + I_f} = Z_{sen} + Z_f \parallel Z_{BJT} + Z_{L,FB} \quad (3.11)$$

$$Z_{inj,FB} = \frac{V_{AEF}}{I_o - I_x} = \frac{Z_{sen,FB}}{\left( \frac{Z_f \parallel Z_{BJT}}{Z_{BJT}} \right) \left( Z_\pi \parallel \frac{Z_\pi}{\alpha} \right) \left( g_m - \frac{\alpha}{Z_\pi} \right)} \quad (3.12)$$

$$Z_{BJT} = \frac{V_f}{I_b + I_x} = Z_{in} + Z_\pi \parallel \frac{Z_\pi}{\alpha} + R_e \left( \frac{1 + Z_\pi g_m}{1 + \alpha} \right) \quad (3.13)$$

$$Z_{L,FB} = \frac{V_L}{I_b + I_x + I_f} = \left( \frac{2}{sC_L} + 2R_L \right) \left( \frac{1 + Z_\pi g_m \frac{Z_f \parallel Z_{BJT}}{Z_{BJT}} + \frac{Z_f \parallel Z_{BJT}}{Z_f} \right) \quad (3.14)$$

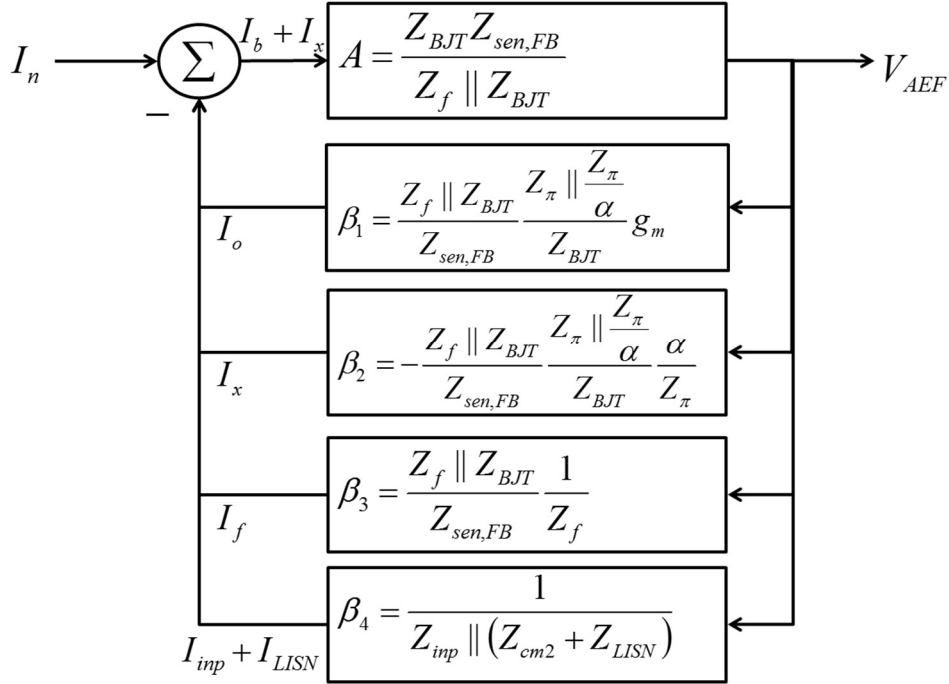


Fig 3-4. The block diagram of the EMI filter with the VSCC AEF

To effectively analyze the EMI filter with AEF, a block diagram can be drawn using the expressions (3.2)-(3.8), as depicted in Fig 3-4. The feedback type of the proposed EMI filter is the shunt-shunt configuration, since the AEF samples a portion of the  $V_{AEF}$  as  $V_\pi$  and converts it to a current [34]. Therefore, the input and output of the block diagram are determined by  $I_n$  and  $V_{AEF}$ . In Fig 4, the  $A$  represents the forward transfer function, which is determined by the ratio of  $V_{AEF}$  to  $(I_b + I_x)$ , and the  $\beta_1$  to  $\beta_4$  correspond to the feedback transfer functions determined by the ratio of each branch current to  $V_{AEF}$ .

### 3.2.3. Loop Gain and Impedance Analysis

The total closed-loop transfer function, which is the ratio of  $V_{AEF}$  to  $I_n$ , corresponds to the impedance seen at the sensing node to the LISN, indicated as  $Z_{in,AEF}$  in Fig 3-3(b). Based on the block diagram reduction rules,  $Z_{in,AEF}$  and the loop gain of the EMI filter with the VSCC AEF can be expressed as,

$$\begin{aligned}
 Z_{in,AEF} &= \frac{V_{AEF}}{I_n} = \frac{A}{1 + A\beta_t} = \frac{1}{\frac{1 + A(\beta_1 + \beta_2 + \beta_3)}{A} + \beta_4} = \frac{A}{1 + A(\beta_1 + \beta_2 + \beta_3)} \parallel \frac{1}{\beta_4} \\
 &= \frac{A}{1 + A(\beta_1 + \beta_2 + \beta_3)} \parallel \frac{1}{\beta_4} = Z_{AEF} \parallel Z_{inp} \parallel (Z_{cm2} + Z_{LISN}) \quad (3.15)
 \end{aligned}$$

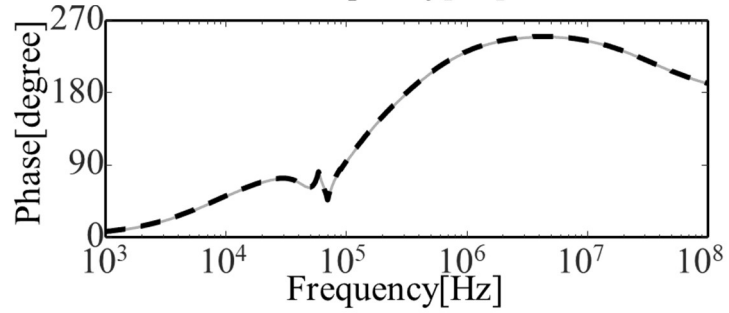
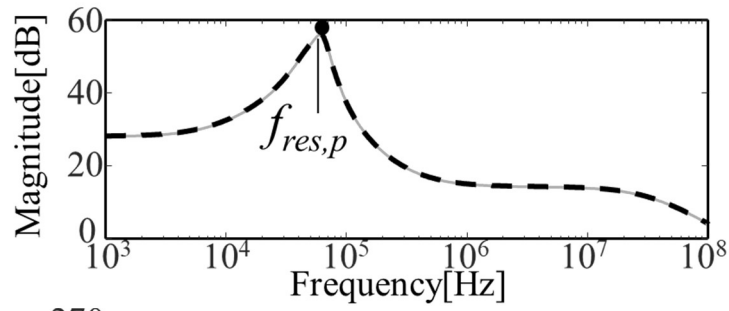
where

$$A\beta_t = \left( Z_\pi \parallel \frac{Z_\pi}{\alpha} \right) \left( g_m - \frac{\alpha}{Z_\pi} \right) + \frac{Z_{BJT}}{Z_f} \left( 1 + \frac{Z_{sen,FB}}{Z_{inp} \parallel (Z_{cm} + Z_{LISN})} \right) + \frac{Z_{sen,FB}}{Z_n \parallel (Z_{cm} + Z_{LISN})} \quad (3.16)$$

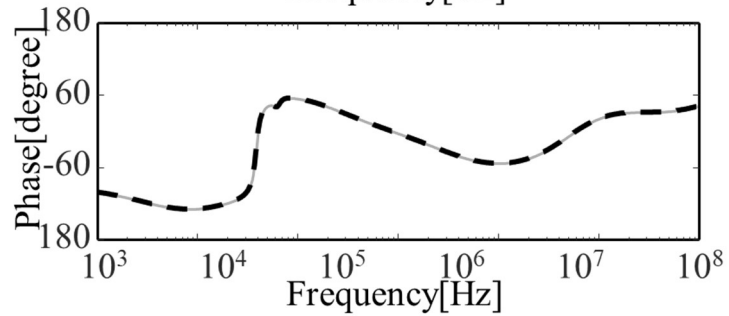
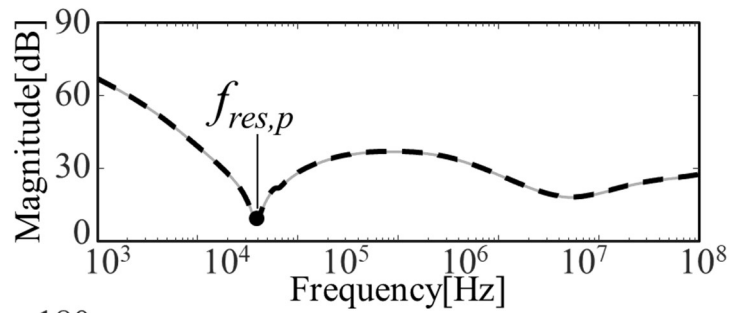
$$Z_{AEF} = \frac{V_{AEF}}{I_b + I_o + I_f} = \frac{A}{1 + A(\beta_1 + \beta_2 + \beta_3)} = \frac{Z_{sen,FB}}{1 + \left( \frac{Z_f \parallel Z_{BJT}}{Z_{BJT}} \right) \left( Z_\pi \parallel \frac{Z_\pi}{\alpha} \right) \left( g_m - \frac{\alpha}{Z_\pi} \right)} \quad (3.17)$$

$\beta_t$  is the sum of the feedback transfer functions from  $\beta_1$  to  $\beta_4$ , and  $A\beta_t$  corresponds to the loop gain of the total EMI filter. The  $Z_{AEF}$  represents the impedance looking at the sensing node in the AEF part, as also indicated in Fig 3-3 (b). Thus, it is verified from (3.15) that the  $Z_{in,AEF}$  consists of the parallel impedance of  $Z_{AEF}$ ,  $Z_{inp}$ , and  $(Z_{cm2} + Z_{LISN})$ , as it can be expected from the circuit structure. The feedback path by  $\beta_4$  is related to the parallel impedance of  $(Z_{cm2} + Z_{LISN})$  and  $Z_{inp}$ , whereas the other feedback paths from  $\beta_1$  to  $\beta_3$  are involved with  $Z_{AEF}$ .

The  $Z_{in,AEF}$  and  $A\beta_t$  are calculated from (3.15) and (3.16) with given circuit parameter values, and validated by SPICE simulations, as shown in Fig 3-5. In Fig 3-5 (a), the peak of  $Z_{in,AEF}$  occurs due to the L-C parallel resonance among  $Z_{cm2}$ ,  $Z_{inp}$  and  $Z_{AEF}$ . The EMI filter might be unstable at the parallel resonance frequency,  $f_{res,p}$ , since the phase of  $A\beta_t$  tends to drastically change at  $f_{res,p}$ , as shown Fig 3-5 (b). The expressions for  $f_{res,p}$  and stability will be further discussed in Section 3.4.



(a)



(b)

Fig 3-5. Calculation (dashed lines) and simulation (solid lines) results (a) Impedance seen at the sensing node to the LISN,  $Z_{in,AEF}$  (b) The loop gain of the EMI filter with AEF,  $A\beta_i$

$Z_{AEF}$  is also calculated from (3.17) and validated by the SPICE simulation, as shown in Fig 3-6(a).  $Z_{AEF}$  is compared to the parallel impedance of ( $Z_{sen}||Z_{inj}$ ) and shows much lower impedance from 6 kHz to 5 MHz. This means that the effective capacitance between the power lines and the earth GND is greatly increased by the AEF operation. Consequently, a large Y-capacitance is achieved by the AEF in the conducted emissions range, which can greatly attenuate the CM-conducted emissions. However, peak  $Z_{AEF}$  occurs due to the series resonance between  $L_f$  and  $C_f$  in the damping circuit. At the series resonance frequency,  $f_{res,s}$ , the impedance of the damping branch is decreased, resulting in a small base-emitter voltage of the BJT. Accordingly, the AEF's performance can be degraded by the damping circuit, which will be further discussed in Section 3.4.

Finally, the effect of the AEF on the noise attenuation ( $NA$ ) of the total EMI filter is investigated. By defining  $I_{LISN,w/oAEF}$  and  $I_{LISN,w/AEF}$  as the LISN current without and with the AEF part, respectively, the  $NA$  due to the AEF is calculated as the ratio of  $I_{LISN,w/oAEF}$  to  $I_{LISN,w/AEF}$  as

$$NA_{AEF} = \frac{I_{LISN,w/oAEF}}{I_{LISN,w/AEF}} = \frac{Z_{cm2} + Z_{LISN} + Z_{AEF} || Z_{inp}}{Z_{AEF} || Z_{inp}} \quad (3.18)$$

The AEF's effectiveness can be verified by comparing it to the EMI filter with passive Y-capacitors in Fig 3-1(a), since the AEF plays the role of the Y-capacitors. To make a fair comparison, the value of the passive Y-capacitor,  $C_Y$ , is set as the sum of  $C_{sen}$ ,  $C_{inj}$  and  $C_{inp}$ , which are utilized in the filter with the VSCC AEF.

The  $NA$  due to the passive Y-capacitor is also calculated as

$$NA_{Y-cap} = \frac{I_{LISN,w/oY-cap}}{I_{LISN,w/Y-cap}} = \frac{Z_{cm2} + Z_{LISN} + Z_{sen} || Z_{inj} || Z_{inp}}{Z_{sen} || Z_{inj} || Z_{inp}} \quad (3.19)$$

where the  $I_{LISN,w/oY-cap}$  and  $I_{LISN,w/Y-cap}$  represent the LISN current without and with the passive Y-capacitors, respectively.

$NA_{AEF}$  and  $NA_{Y-cap}$  have been calculated with given circuit parameter values and compared in Fig 3-6(b).  $NA_{AEF}$  is significantly higher than  $NA_{Y-cap}$  from 100 kHz to 5 MHz, which is attributed to the smaller impedance of the AEF in Fig 3-6(a). That is, the effective capacitance increased by the AEF results in an increase in the  $NA$  of CM-conducted emissions.

The effects of the increased capacitance on the safety requirements should be also investigated. The touch or leakage current flowing through a human body is limited by the regulations such as UL101-2002 and IEC60990. In the 'let-go' measurement condition imposing the worst leakage current for the AEF, the measuring network has a low-pass filter characteristic below 1kHz, and the leakage current is predominantly generated by the low-frequency voltage or currents below 1kHz [2]. As shown in



Fig 3-6 (a), the VSCC AEF increases the effective capacitance between the power lines and the earth GND predominantly in the conducted emissions frequency range above 150kHz. Since the impedance below 1kHz is rarely affected by the AEF, the influence of the AEF on the safety requirements for the leakage current is very limited. The AEF can attenuate the conducted emissions without sacrificing the safety, which is the great advantage of using the AEF.

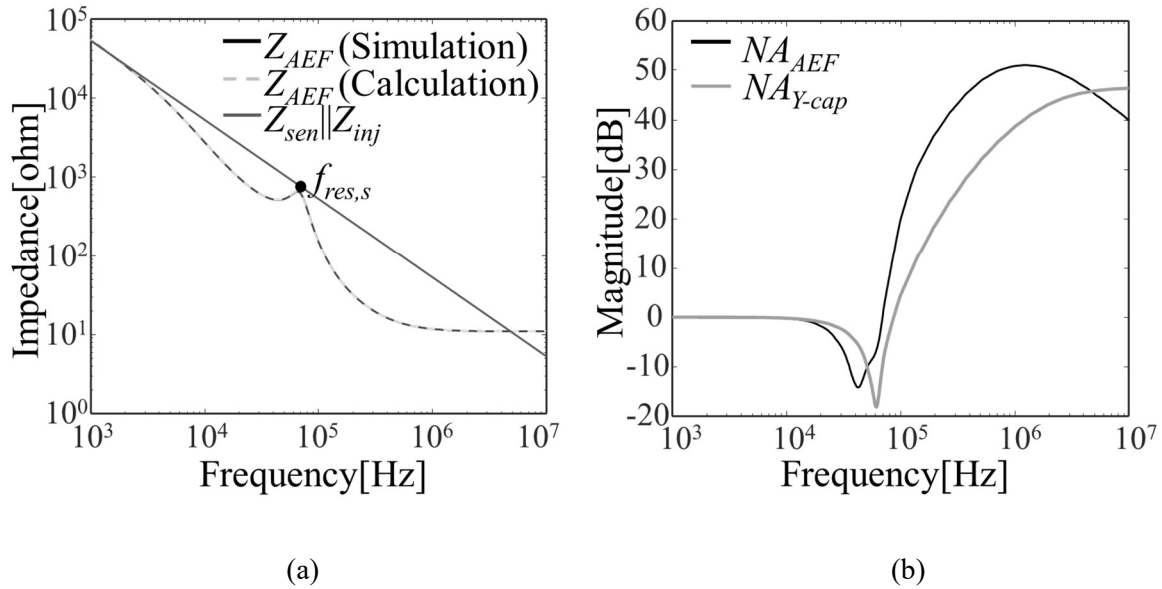


Fig 3-6(a) The impedance of the AEF part,  $Z_{AEF}$  (b)  $NA$  due to the AEF and passive Y-capacitor

### 3.3. Design Guidelines of the VSCC AEF For the Performance

In this section, the design guidelines for optimized performance are derived from an investigation into the AEF impedance,  $Z_{AEF}$ . Although the push-pull amplifier in the VSCC AEF is quite simple, the push-pull amplifier should be carefully designed since the bandwidth of a BJT and bias circuit affect AEF performance.

#### 3.3.1. The Selection of $C_{inp}$ , $C_{sen}$ , $C_{inj}$ , $C_{DC}$

The AEF performance is also affected by the impedance looking from the sensing node into the noise source, which is indicated as  $Z_{EUT}$  in Fig 3-3(b). Its value depends on the CM choke and impedance of the noise source. The impedance of CM noise source is typically related to the parasitic capacitance,  $C_n$ , among the switching components, heat sink, and earth GND [6]. Since the  $C_n$  is generally quite small, in tens of pF, the value of  $Z_{EUT}$  is predominantly determined by  $C_n$ . To eliminate

the effect of  $Z_{EUT}$  on the AEF performance, the input filter capacitors,  $C_{inp}$ , are used to screen out the  $Z_{EUT}$ . Thus, the value of  $C_{inp}$  should be sufficiently larger than  $C_n$ . A convenient guideline can be chosen as

$$C_{inp} \geq 5C_n \quad (3.20)$$

Expressions (3.1)-(3.17) have already neglected the effect of  $Z_{EUT}$ .

As shown in Fig 3-6, the variation of  $Z_{AEF}$  is the most responsible for the  $NA$  of the AEF, and the main design factors can be extracted from its expression. However, the expression of (3.17) is too complicated due to the damping circuits. The damping circuits are designed only for feedback stability, and their effects on the performance can be ignored by a proper design, which will be discussed in the next section. In drawing the design guidelines for optimum performance, the  $Z_{AEF}$  and  $\alpha$  are calculated again without the damping circuits for simplification.  $Z_{AEF0}$  and  $\alpha_0$ , which represent the  $Z_{AEF}$  and  $\alpha$  without the damping circuits, can be expressed as

$$Z_{AEF0} = \frac{Z_{sen} + Z_{\pi} \parallel \frac{Z_{\pi}}{\alpha_0} + (R_e + Z_L) \left( Z_{\pi} \parallel \frac{Z_{\pi}}{\alpha_0} \right) \left( g_m - \frac{\alpha_0}{Z_{\pi}} \right)}{1 + \left( Z_{\pi} \parallel \frac{Z_{\pi}}{\alpha_0} \right) \left( g_m - \frac{\alpha_0}{Z_{\pi}} \right)} \approx \frac{Z_{sen}}{Z_{\pi} g_m} \alpha_0 + \frac{1}{g_m} + R_e + \frac{2}{sC_L} + 2R_L \quad (3.21)$$

where,

$$\alpha_0 = \frac{I_x}{I_b} = \frac{Z_{inj} Z_{\pi} g_m - Z_{sen}}{Z_{sen} + Z_{bias} + Z_{inj}} \quad (3.22)$$

The  $Z_{AEF0}$  can be further simplified at low-frequency and high-frequency ranges, respectively. At the low frequency,  $Z_{sen} + Z_{inj} > Z_{bias}$ ,  $Z_{AEF0}$  can be simplified as

$$Z_{AEF0,low} \approx Z_{sen} \parallel Z_{inj} = \frac{1}{s(C_{sen} + C_{inj})} \quad (3.23)$$

Oppositely, at the high frequency,  $Z_{sen} + Z_{inj} < Z_{bias}$ ,  $Z_{AEF0}$  can also be simplified as

$$Z_{AEF0,high} \approx \frac{Z_{sen} Z_{inj}}{Z_{bias}} + \frac{1}{g_m} + R_e + \frac{2}{sC_L} + 2R_L \quad (3.24)$$

$Z_{AEF0,low}$  and  $Z_{AEF0,high}$  are overlapped with  $Z_{AEF0}$  at the relatively lower and higher frequency ranges, respectively, as shown in Fig 3-7.

The boundary frequency between the two ranges,  $f_{op}$ , can be found from  $Z_{sen} + Z_{inj} = Z_{bias}$ , which is calculated as

$$f_{op} = \frac{C_{sen} + C_{inj}}{2\pi C_{sen} C_{inj} R_{bias}} \quad (3.25)$$

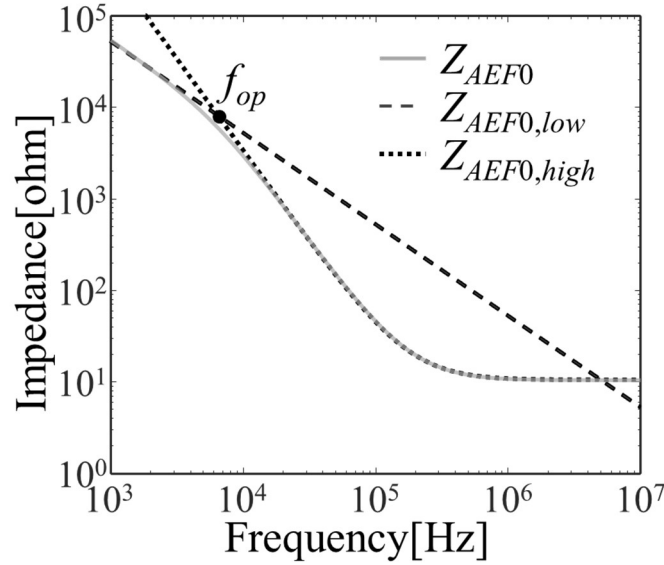


Fig 3-7. Impedance of the AEF without the damping circuits,  $Z_{AEF0}$  (solid lines), The impedance is approximated to  $Z_{AEF0,low}$  (dashed lines) and  $Z_{AEF0,high}$  (dotted lines) at the low and high frequency ranges, respectively.

Although a higher Y-capacitance results in a higher reduction of CM-conducted emissions, the high capacitance also causes a larger leakage current to the earth GND, which is strictly limited by safety regulations. When applying the AEF, however, the Y-capacitance is effectively enlarged in the conducted emission frequency range, but the safety regulation on the leakage current is still satisfied by maintaining the low capacitance at lower frequency range. In the EMI filter employing the AEF, the Y-capacitance at the low-frequency is determined by the sum of  $C_{inp}$  and the capacitance produced by (3.23). Accordingly, the design target of the AEF reduces the values of  $Z_{AEF0,high}$  and  $f_{op}$  as much as possible while maintaining the sum of  $C_{inp}$ ,  $C_{sen}$ , and  $C_{inj}$  to be under the maximum allowable Y-capacitance,  $C_{Y,max}$ .

Therefore, the optimized solution for  $C_{sen}$  and  $C_{inj}$  is given as

$$(C_{sen} = C_{inj}) \leq 0.5(C_{Y,max} - C_{inp}) \quad (3.26)$$

On the other hand, as aforementioned, the AC utility voltage and differential-mode noises from the EUT can be coupled to the DC supply of the AEF through the two  $C_{inj}$  capacitors. When the decoupling capacitor,  $C_{DC}$ , is employed, the coupling transfer function from the power lines to the

AEF supply at low frequencies is approximately given as  $C_{inj}/(C_{inj} + 2C_{DC})$ . Since the noise coupling due to the AC utility voltage is usually predominant, a guideline for the value of  $C_{DC}$  can be constructed as

$$\frac{C_{inj}}{C_{inj} + 2C_{DC}}V_{AC} < 0.01V_{DC} \quad (3.27)$$

where  $V_{AC}$  and  $V_{DC}$  are the amplitudes of the AC utility voltage and the DC level of the AEF supply, respectively. The equation (3.27) represent that the coupled noise voltage due to of the AC utility voltage should be less than 1% of the  $V_{DC}$  to avoid the malfunction of the AEF or control board. The noise tolerant level can be adjusted as required.

### 3.3.2. BJT Selection and Push-pull Amplifier Design

The BJTs in the push-pull amplifier should have an operational bandwidth higher than the conducted emissions frequency. Also, the maximum output current of a BJT should be sufficiently larger than the CM noise current  $I_n$  for compensation. The small signal current gain of the BJT,  $g_m$ , also contributes to the expression of  $Z_{AEF,high}$ , as shown in (3.24); however, the term for  $1/g_m$  may be negligible compared to the other terms in a proper design. Therefore, the necessary conditions for BJT specification can be simply summarized as

$$f_T \gg f_H \quad (3.28)$$

$$I_{c,max} \gg I_n \quad (3.29)$$

$f_T$  and  $f_H$  represent the unity current gain bandwidth of a BJT and the high frequency boundary of the conducted emissions, respectively.  $I_{c,max}$  indicates the maximum limit of the BJT collector current. It is shown in (3.24) that  $R_e$  increases  $Z_{AEF0,high}$  and thus degrades AEF performance, but it is necessary to stabilize the BJT bias. The thermal runaway of a BJT also can be prevented by  $R_e$ . The typical value of  $R_e$  is chosen as 1~4Ω.

When the maximum noise voltage is applied to the input of the push-pull amplifier, the collector-emitter voltage,  $V_{ce}$ , may approach the saturation region voltage,  $V_{ce(sat)}$ , and the voltage at the BJT emitter becomes  $\pm(V_{DC}/2 - V_{ce(sat)})$ . The maximum output current of the push-pull amplifier,  $I_{o,max}$ , is then generated as  $|V_{DC}/2 - V_{ce(sat)}|/(R_e + 2R_L)$ . For proper operation,  $I_{o,max}$  should be adjusted to a setting lower than  $I_{c,max}$  by using  $R_L$ . From the relation of  $(V_{DC}/2 - V_{ce(sat)})/(R_e + 2R_L) \leq I_{c,max}$ , the design guideline of  $R_L$  can be extracted as

$$R_L \geq \frac{1}{2I_{c,max}} \left( \frac{V_{DC}}{2} - V_{ce,sat} \right) - \frac{R_e}{2} \quad (3.30)$$

As shown in (3.24), the magnitude of  $Z_{AEF0,high}$  is directly influenced by  $R_L$ . Therefore,  $R_L$  should be designed as small as possible while satisfying (3.30). Also, expression (3.30) indicates that a higher  $I_{c,max}$  of BJT allows a smaller  $R_L$  value, which can improve AEF performance. Accordingly, the current capacity of BJTs and the value of  $R_L$  should be considered simultaneously in the selection of BJTs and  $R_L$ .

Next, the bias components of BJTs,  $R_{bias}$ , and  $R_p$ , are designed. The value of  $R_{bias}$  is determined first using (3.25) with the target  $f_{op}$  as

$$R_{bias} = \frac{C_{sen} + C_{inj}}{2\pi C_{sen} C_{inj} f_{op}} \quad (3.31)$$

The value of  $R_p$  can then be obtained by the DC bias analysis of BJTs. Since the push-pull amplifier is designed as a class AB amplifier, the bias point of each BJT is located slightly above the cutoff. By carrying out KVL from the base to the emitter for a half portion of the push-pull amplifier, the equation can be derived as,

$$\frac{\frac{R_p}{2}}{R_{bias} + \frac{R_p}{2}} \frac{V_{DC}}{2} = I_B \left( R_{bias} \parallel \frac{R_p}{2} \right) + V_{BE} + (I_C + I_B) R_e \quad (3.32)$$

where,

$$V_{BE} = V_T \ln \frac{I_c}{I_s} \quad (3.33)$$

$I_C$ ,  $I_B$ , and  $V_{BE}$  represent the DC collector current, the base current, and the base-emitter voltage, respectively. The value of  $I_c$  is selected first to achieve a slight forward bias for each BJT based on the I-V curve of the BJTs. The value of  $R_p$  can then be extracted by solving (3.32).

The output of the push-pull amplifier may have a difference DC level from the earth GND, and the  $C_L$  is inserted at the amplifier output as a DC block. Since  $Z_{AEF0,high}$  is directly affected by  $C_L$ , as shown in (3.24), the impedance from  $C_L$  should be also negligible. If  $2/(sC_L) \leq Z_{sen} Z_{inj} / Z_{bias}$  is in the target frequency range, (3.24) can guarantee that the effects of  $C_L$  on the AEF performance are negligible. Thus, a convenient quantitative boundary for  $C_L$  can be decided as

$$C_L \gg 4\pi f_L C_{sen} C_{inj} R_{bias} \quad (3.34)$$

where  $f_L$  represents the low frequency boundary of the conducted emissions.

### 3.4. Design Guidelines of the AEF For Stability and Immunity

The stability and immunity of the VSCC AEF should be guaranteed to apply to a real product. As aforementioned, the damping circuits are essential for feedback stability. The damping circuits are already included in expressions (3.1)-(3.17). In this section, the design guidelines of the damping circuits are developed step-by-step by investigating their effects on the total loop gain and the AEF impedance,  $A\beta_i$  and  $Z_{AEF}$ . Also, the transient immunity standards require that any product should continue to operate correctly after a transient immunity test, such as the lightning surge test. Since the surge test is applied to AC power lines, the components in the AEF can be directly affected by the high voltage transient through the sensing and injection parts. The protection circuits are designed herein to prevent damage from lightning surges.

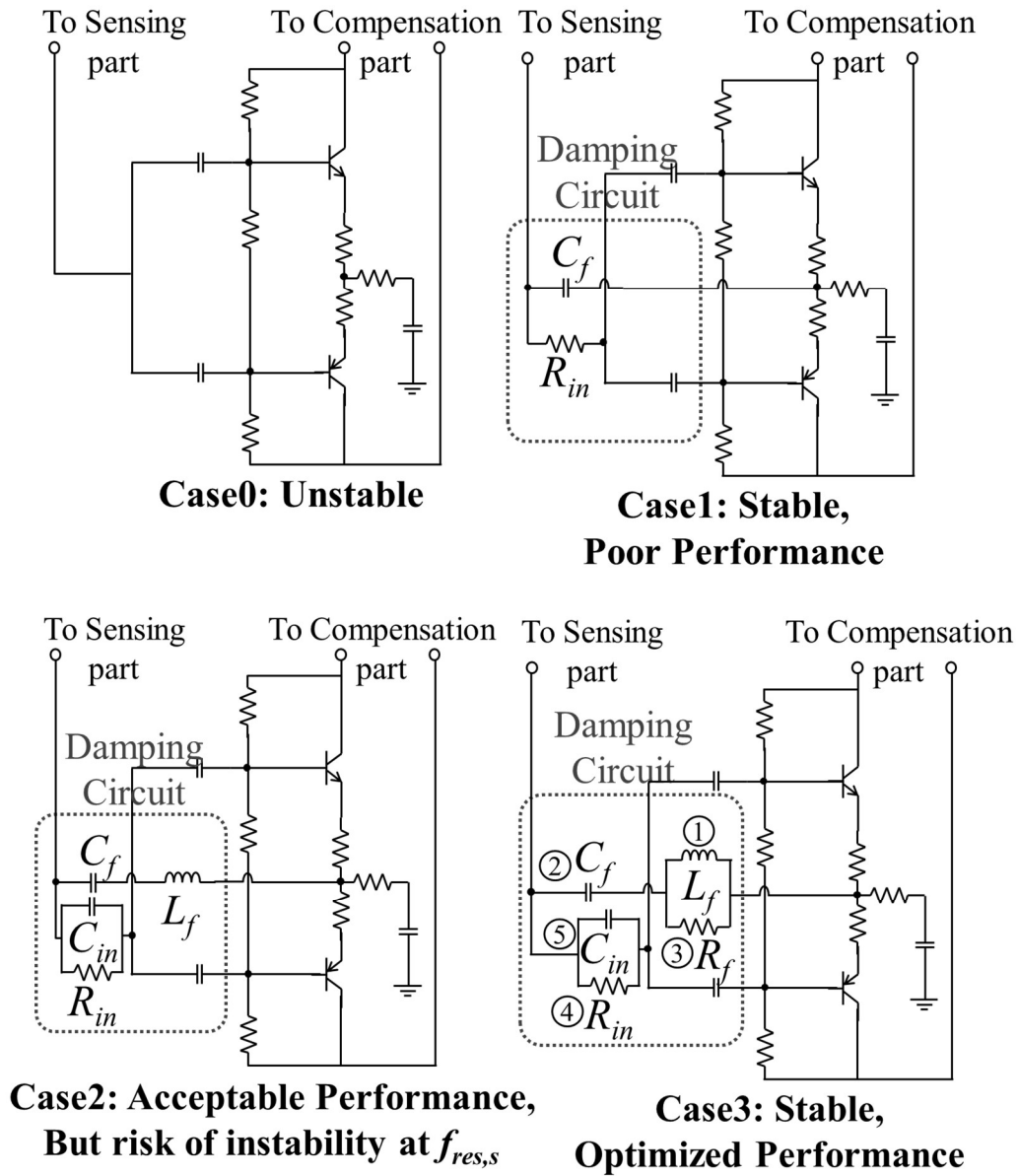
#### 3.4.1. Damping Circuit Design for System Stability

The design of the damping circuits is the most challenging part of the AEF design. As mentioned in Section 3.2.3, system instability of the EMI filter employing the AEF may occur due to the parallel resonance among  $Z_{AEF}$ ,  $Z_{inp}$ , and  $Z_{cm2}$ , since the phase of the loop gain,  $A\beta_i$  in (3.16), greatly changes at the resonance frequency,  $f_{res,p}$ . That is, for the system to be stable, the  $A\beta_i$  phase should remain below  $180^\circ$  even at  $f_{res,p}$ , as the magnitude of  $A\beta_i$  is larger than 0dB, as shown in Fig 3-5(b).

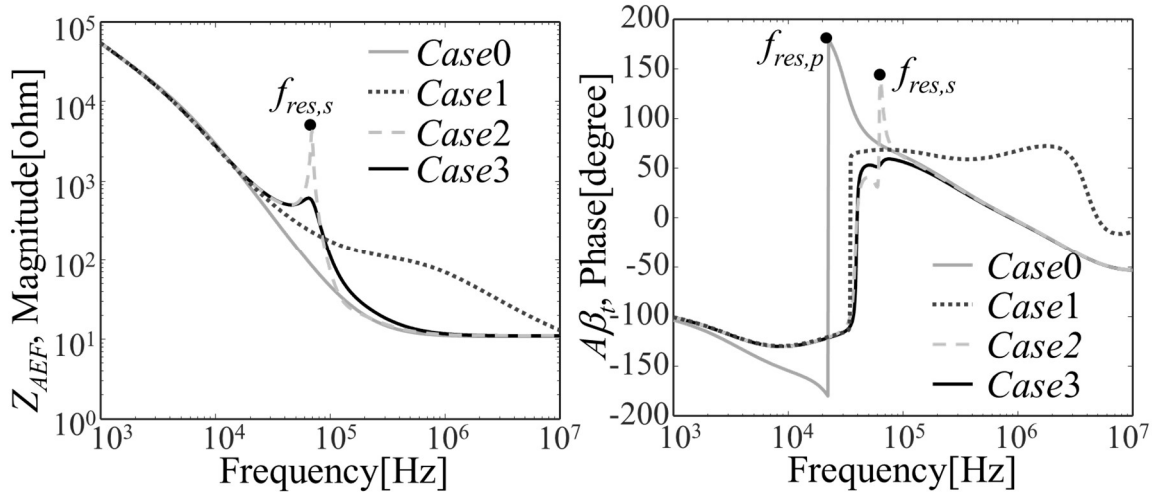
Herein, damping circuits are employed to resolve the feedback stability issue. The proper damping circuits should make the EMI filter stable, while maintaining the NA performance. To investigate the role and necessity of each damping circuit element step-by-step, four different cases are tested, as shown in Fig 3-8, where only the AEF parts are drawn for simplicity. Note that all other components in the EMI filter remain exactly the same.

Each case in Fig 3-8(a) has different configurations of the damping circuits. Starting from the case without any damping circuits, Case0, the stability or performance problems of the AEF are resolved by adding required circuit components. Initially, the EMI filter of Case0 is most likely unstable. Thus, the damping circuits made of  $C_f$  and  $R_{in}$  are added in Case1, and the filter becomes stable; however, its NA performance is significantly degraded. To recover the NA performance of the filter,  $L_f$  and  $C_{in}$  are inserted at each damping branch, as shown in Case2. In Case2, however, a risk of instability arises due to the series resonance between  $L_f$  and  $C_f$  at the resonance frequency,  $f_{res,s}$ . Therefore,  $R_f$  is also added to suppress the Q-factor of the series resonance in Case3. Finally, both stability and performance of the AEF are optimized in Case3.

The stability and performance of the AEF can be accurately identified by observing the AEF impedance and loop gain,  $Z_{AEF}$  and  $A\beta_t$ . Those parameters for each case are calculated using (3.16) and (3.17) and are plotted in Fig 3-8(b). The effects of each damping circuit part, which are explained above, can be clearly observed.



(a)



(b)

Fig 3-8. Investigation of four different configurations of the damping circuits (a) Circuit schematics (only the AEF parts are drawn for simplicity) (b) the impedance of the AEF part and the total loop gain,  $Z_{AEF}$  and  $A\beta_t$

To extract quantitative design guides of the damping circuits, rigorous mathematical analysis is performed. The expressions of  $A\beta_t$  and  $Z_{AEF}$  in (3.16)-(3.17) can be approximated to simpler forms. In the low frequency range up to  $f_{res,p}$ ,  $A\beta_t$  in (3.16) can be expressed as

$$A\beta_t \approx Z_\pi \parallel \frac{Z_\pi}{\alpha} g_m + \left( 1 + \frac{Z_{in}}{Z_f} \right) \left( \frac{Z_{sen}}{Z_{cm2} + Z_{LISN}} \right) \quad (3.35)$$

Also, in the frequency range from  $f_L$  to  $f_H$  for the conducted emissions, the  $Z_{AEF}$  in (3.17) can be approximated as

$$Z_{AEF} \approx \frac{Z_{sen} + Z_f \parallel Z_{BJT,A}}{1 + \left( \frac{Z_f}{Z_f + Z_{BJT,A}} \right) \left( Z_\pi \parallel \frac{Z_\pi}{\alpha} \right) \left( g_m - \frac{\alpha}{Z_\pi} \right)} + \frac{2}{sC_L} \parallel 2R_L \quad (3.36)$$

where

$$Z_{BJT,A} = Z_{in} + Z_\pi \parallel \frac{Z_\pi}{\alpha} (1 + R_E g_m) \quad (3.37)$$

$Z_{BJT,A}$  indicates the approximated expression for  $Z_{BJT}$  of (3.13) in the conducted emissions frequency range.

The damping circuit components are included in  $Z_{in}$  and  $Z_f$ . When the damping circuits are not



applied, as in Case0, the second term of (3.35) becomes simply  $Z_{sen}/(Z_{cm2}+Z_{LISN})$ . The phase of  $A\beta_i$  in Case0 is close to  $180^\circ$ , as shown in Fig 3-8(b), since  $A\beta_i$  of Case0 includes a second order system response due to  $Z_{sen}/(Z_{cm2}+Z_{LISN})$ . Accordingly, an AEF without any damping circuits would be basically unstable.

Proper damping circuits should make the second term in the loop gain expression (3.35) be the first order system to avoid the phase of  $180^\circ$  at the  $f_{res,p}$  frequency. By placing  $C_f$  and  $R_{in}$  as shown in Case1 of Fig 3-8(a),  $Z_f=1/(sC_f)$  and  $Z_{in}=R_{in}$ . If  $R_{in}/(1/(2\pi f_{res,p}C_f))>1$ , then the second term of (3.35) behaves as the first order system by cancelling the effect of  $Z_{sen}$  using  $Z_f$ . Therefore, in Case1, the phase of the loop gain,  $A\beta_i$ , does not reach  $180^\circ$  and the EMI filter with AEF can stay stable. As a result, the relationship between  $C_f$  and  $R_{in}$  can be extracted from the condition for stability,  $R_{in}/(1/(2\pi f_{res,p}C_f))>1$  at  $f_{res,p}$ , as

$$R_{in} \geq \frac{1}{2\pi f_{res,p} C_f} \quad (3.38)$$

where,

$$f_{res,p} \approx \frac{1}{2\pi \sqrt[3]{C_{sen} C_{inj} R_{bias} (L_{cm2} + M_{cm2})}} \quad (3.39)$$

Another design rule of  $C_f$  will be presented later using Case2 of Fig 3-8(a), since the design rule of  $C_f$  is associated with other parameters in the damping circuits.

The effects of the damping circuits in Case1 on  $Z_{AEF}$  also should be investigated. The  $Z_{BJT,A}$  of (3.37) is increased by  $R_{in}$  compared to that without damping circuits. Then, the denominator of the first term in (3.36) approaches '1' because the  $Z_f$  is much smaller than  $Z_{BJT,A}$  in the conducted emissions frequency range. Accordingly, the  $Z_{AEF}$  in Case1 maintains a high impedance close to  $(Z_{sen}+Z_f+(2/(sC_L))\|2R_L)$  in the target frequency range. In other words, the effective capacitance of  $Z_{AEF}$  is not increased when the damping circuits,  $C_f$  and  $R_{in}$ , are employed, as shown in Fig 3-8(b).

To resolve the  $NA$  performance degradation due to the damping circuits,  $Z_f$  should remain greater than  $Z_{BJT,A}$ . Also,  $Z_{in}$  should be smaller than the other term in  $Z_{BJT,A}$  of (3.37) to suppress the effect of  $R_{in}$  on the  $Z_{AEF}$ . For these reasons,  $L_f$  is added in series at the impedance  $Z_f$ , and  $C_{in}$  is added in parallel at  $Z_{in}$ , as shown in Case2 of Fig 3-8(a). By adjusting the values of  $L_f$  and  $C_{in}$ , the increased effective capacitance of  $Z_{AEF}$  can be achieved in the frequency range of the conducted emissions, as shown in Case2 of Fig 3-8(b).

Quantitatively, the impedance of  $L_f$  should be larger than  $Z_\pi$  to achieve the condition of ( $Z_f > Z_{BJT,A}$ ), since the  $L_f$  and  $Z_\pi$  have dominant impedances in  $Z_f$  and  $Z_{BJT,A}$ , respectively. The design rule for  $L_f$  can be found at the low frequency limit for the conducted emissions,  $f_L$ , as

$$L_f > \frac{1}{4\pi f_L} \left( r_\pi \parallel \frac{1}{2\pi f_L C_\pi} \right) \quad (3.40)$$

Similarly, the impedance of  $C_{in}$  should be smaller than  $Z_\pi$  at the frequency  $f_L$ , as  $1/(2\pi f_L C_{in}) < r_\pi \parallel (1/(2\pi f_L C_\pi))$ .

For the stability to still be retained, the effects of the  $L_f$  and  $C_{in}$  at the frequency  $f_{res,p}$  should be negligible. That is, the impedance of  $C_f$  at  $f_{res,p}$  should be sufficiently larger than that of  $L_f$ . For convenience sake, a design guide can be drawn from  $1/(2\pi f_{res,p} C_f) \geq 5 \cdot (2\pi f_{res,p} L_f)$ , as

$$C_f \leq \frac{1}{20\pi^2 f_{res,p}^2 L_f} \quad (3.41)$$

Also, the impedance of  $C_{in}$  should be sufficiently larger than  $R_{in}$ , as  $1/(2\pi f_{res,p} C_{in}) \geq 5R_{in}$ . Considering both conditions for  $C_{in}$  regarding the performance ( $1/(2\pi f_L C_{in}) \leq r_\pi \parallel (1/(2\pi f_L C_\pi))$ ) and the stability ( $1/(2\pi f_{res,p} C_{in}) \geq 5R_{in}$ ), the design guideline of  $C_{in}$  can be summarized as

$$\frac{1}{2\pi f_L (r_\pi \parallel 1/(2\pi C_\pi f_L))} \leq C_{in} \leq \frac{1}{10\pi f_{res,p} R_{in}} \quad (3.42)$$

When the damping circuit components are designed based on (3.38), (3.40), (3.41), and (3.42), a stable AEF system with acceptable performance can be achieved in the conducted emissions frequency range, as shown in Case2 of Fig 3-8(b).

A final trim is still needed in the damping circuit design, however. A series resonance occurs between  $L_f$  and  $C_f$ . At the resonance frequency,  $f_{res,s}$ , the magnitude of  $Z_f$  is minimized and the phase abruptly changes. If the minimum  $Z_f$  at  $f_{res,s}$  is much smaller than  $Z_{BJT,A}$ , a peak of  $Z_{AEF}$  occurs, as shown in Fig 3-8(b), since the denominator of the first term in (3.37) is close to '1'. Also, the phase of the loop gain,  $A\beta_i$ , abruptly increases at  $f_{res,s}$  through a rapid phase variation of  $Z_f$ . Accordingly, the variation of  $Z_f$  at the  $f_{res,s}$  frequency should be mitigated by adjusting the quality factor of the series resonance. Hence,  $R_f$  is added in parallel with  $L_f$  to adjust the quality (Q) factor, as shown in Case3 of Fig 3-8. Both the performance degradation and the instability risk at  $f_{res,s}$  can be mitigated by designing the Q factor, which is expressed as  $R_f/(2\pi f_{res,s} L_f)$ , to be smaller than 10. The purpose of the  $R_f$  is only to reduce the Q-factor without affecting the roles of other damping circuit components. Thus,  $R_f$  should be sufficiently larger than the impedance of  $L_f$  at  $f_{res,p}$ , such that  $R_f \geq 5 \cdot (2\pi f_{res,p} L_f)$ . In

summary, the design guides for  $R_f$  can be extracted as,

$$10\pi f_{res,p} L_f \leq R_f \leq 20\pi f_{res,s} L_f \quad (3.43)$$

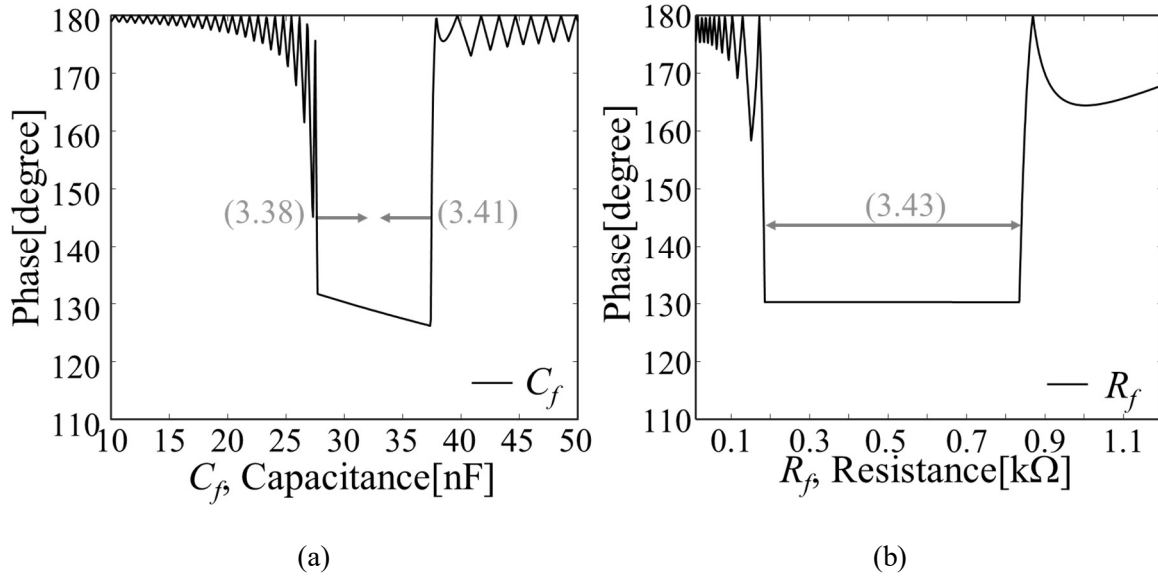
where

$$f_{res,s} = \frac{1}{2\pi\sqrt{L_f C_f}} \quad (3.44)$$

Finally, after  $R_f$  is designed based on (3.43) and applied in the damping circuits, both stability and performance are optimized, as shown in Case3 of Fig 3-8(b).

Physically, the role of each damping circuit component so far can be summarized as follows. The amplifier input voltage is attenuated by  $R_{in}$  at the  $f_{res,p}$  frequency for stability. The noise voltages in the conducted emissions frequency range can be still applied well to the amplifier input through  $C_{in}$  for performance. The  $C_f$  is the phase compensation capacitor for stability. The large impedance of  $R_f$  and  $L_f$  make the phase compensation path invisible in the conducted emissions frequency range for performance.

In practical designs, all the values of the damping circuit components can be easily designed by selecting the  $L_f$  value first, since the  $L_f$  in (3.40) is only a function of the BJT parameters. The most convenient order for selecting component values is denoted by the numbers in circles in the figure for Case3 in Fig 3-8(a).



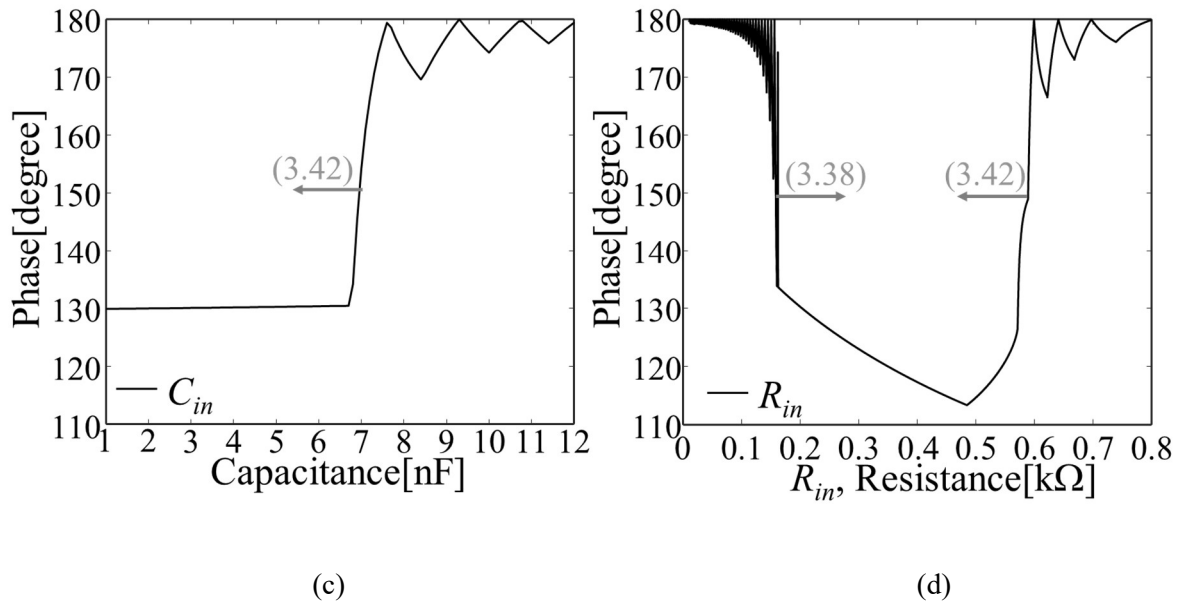


Fig 3-9. The maximum phase of the loop gain,  $A\beta_i$ , while sweeping the value of (a)  $C_f$ , (b)  $R_f$ , (c)  $C_{in}$ , and (d)  $R_{in}$

The maximum phase of the loop gain over the whole frequency range is calculated using (3.16), and is plotted by sweeping the value of each damping circuit component, as shown in Fig 3-9. The values of all other components except for the swept value are fixed to the designed values. In Fig 3-9(a), a  $C_f$  value smaller than 27 nF or larger than 38 nF can cause system instability by violating design rule (3.38) or (3.41). The unstable ranges due to the value of  $R_f$  in Fig 3-9(b) are attributed to (3.43). Although there are both low and high limits in choosing the value of  $C_{in}$ , as (3.42), system instability occurs only at a large  $C_{in}$  exceeding the high boundary, as shown in Fig 3-9(c), since the low boundary is due to  $NA$  performance. In the case of  $R_{in}$ , system instability is caused by violating design rules (3.38) and (3.42), as shown in Fig 3-9(d). The increase of  $C_f$  and  $R_{in}$  allows the AEF to be more stable by decreasing the maximum phase in the whole frequency range, as shown in Fig 3-9(a) and (d). When  $R_{in}$  and  $C_f$  are adjusted for system stability, all other components in the damping circuits also should be re-designed according to the design guides, since all the damping circuit components are related to each other.

The effects of the damping circuits on the stability can be demonstrated by measuring the CM noise at the LISN side after removing the damping circuits in the AEF. Fig 3-10 (a) and (b) show the results measured in both time and frequency domains using oscilloscope and spectrum analyzer, respectively. In the measurements, the EUT was turned off while only the AEF turned on. Without the damping

circuits, the oscillation due to the instability occurs, creating the peaks at its harmonics in the frequency spectrum. After applying the damping circuits, all the oscillations and harmonic peaks disappear, as shown in Fig 3-10. The damping circuits are an essential part in the VSCC AEF.

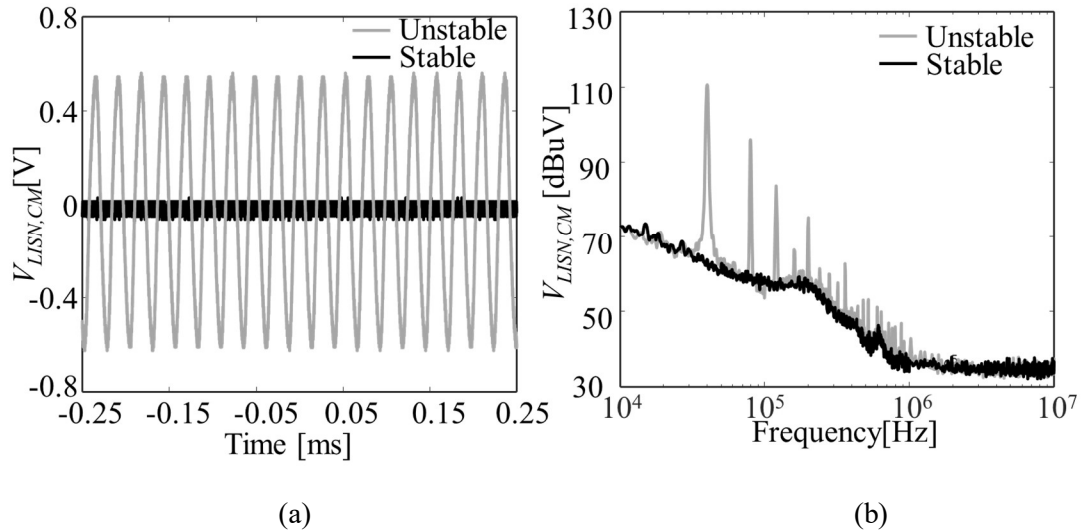


Fig 3-10. The CM noise with and without the damping circuits (a) in the time-domain measurements (b) in the frequency-domain measurements

### 3.4.2. Surge Protection Circuit Design

The high voltage transient caused by a lightning surge can physically damage the components of power converters inside appliances. Generally, protectors such as metal oxide varistor and gas discharge tubes are additionally installed prior to the EMI filter for overvoltage clamping, as denoted as  $M_1$ ,  $M_2$ , and GDT in Fig 3-11. However, the clamping voltage of the varistor and GDT in front of the EMI filter are usually very high – as much as several kV – to avoid interrupting the normal operation of the power system. Hence, despite the presence of those protectors, an overvoltage of several kV can be still generated and applied to the AEF.

When the lightning surge occurs, the overvoltage between collector and emitter nodes can damage the BJTs. Furthermore, an overcurrent can flow between the power lines and earth GND through  $R_e$ ,  $R_L$ ,  $R_{in}$ ,  $R_f$ , and BJTs. The passive components in the AEF should also be protected from the high-power transient, requiring additional protection circuits in the AEF side. The protection circuits are implemented using the varistor at the input side of the AEF,  $M_3$ , and the transient voltage suppression (TVS) diodes,  $T_1$  and  $T_2$ , along both NPN and PNP BJTs, respectively, as shown in Fig 3-11. The TVS diodes for protecting the BJTs are chosen to have a lower clamping voltage and a faster response

compared to the varistor; whereas, the varistor,  $M_3$ , at the amplifier input is chosen to dissipate a high current and high energy. The varistor at the amplifier input can be also replaced by a TVS diode if a fast response is required.

The bidirectional TVS diodes,  $T_1$ , protect the BJTs and passive components from the high voltage transient. Since the voltage across the  $T_1$  is limited by the clamping voltage of  $T_1$ ,  $V_{T1}$ , the  $V_{T1}$  should be lower than the maximum collector-emitter voltage tolerance,  $V_{CE,max}$ , but higher than  $V_{DC}$  in order not to interrupt the normal AEF operation. Accordingly, the condition for choosing the  $V_{T1}$  can be simply written as

$$V_{DC} < V_{T1} < V_{CE,max} \quad (3.45)$$

The  $M_3$  protects the passive components at the amplifier input side against the high voltage transient. The DC block capacitor,  $C_M$ , is also added between  $C_{sen}$  and  $M_3$  to avoid any unwanted operation of  $M_3$  due to a DC voltage difference between the sensing node and the earth GND. If the high voltage transients are generated, the  $M_3$  should operate below the rating voltage of the passive components that are placed at the amplifier input. Assuming the lowest rating voltage in the passive components is  $V_{passive,rate}$ , the condition for the clamping voltage of  $M_3$ ,  $V_{M3}$ , is conveniently given as

$$V_{M3} < V_{passive,rate} \quad (3.46)$$

The parasitics in the varistor and TVS diode can degrade the performance of the VSCC AEF. The characteristics of the protection devices at the idle state in the conducted emissions frequency range should be dominated by parasitic capacitance. Thus, the parasitic capacitance in the varistor and TVS should be also considered in selecting the protection devices. By naming the parasitic capacitance of  $M_3$  and  $T_1$  as  $C_{para,M3}$  and  $C_{para,T1}$ , respectively, the impedance of the protection devices can be written as

$$Z_{para,M3} = \frac{1}{sC_{para,M3}}, \quad Z_{para,T1} = \frac{1}{sC_{para,T1}}$$

Also, the impedances looking at the input and the collector nodes of the push-pull amplifier with reference to the earth GND are named as  $Z_B$  and  $Z_C$ , respectively, as shown in Fig 3-11. In the conducted emissions frequency range,  $Z_{in}$  and  $C_L$  are negligible, and the  $Z_B$  and  $Z_C$  can be expressed as,

$$Z_B = \frac{V_B}{I_b + I_x + I_f} = Z_{BJT} \parallel Z_f + Z_{L,FB} \approx \left( 1 + \frac{2R_L g_m}{1 + R_E g_m} \right) \left( R_f \parallel \frac{Z_\pi}{1 + \alpha} (1 + R_E g_m) \right)$$

$$Z_C = \frac{V_C}{I_o - I_x} \approx -\left(Z_{bias} - \frac{Z_\pi}{\alpha}\right) \frac{I_x}{I_o - I_x} \approx -Z_{inj}$$

where the  $\alpha$  given in (3.1) also can be approximated to  $(Z_{inj}Z_\pi g_m / Z_{bias})$ .

To avoid the performance degradation of the AEF, the currents flowing through the  $M_3$  and  $T_1$  should be smaller than the currents into the base and the collector of the BJTs, respectively, in the conducted emissions frequency range. Accordingly,  $Z_B$  and  $Z_C$  should be sufficiently smaller than  $Z_{para,M3}$  and  $Z_{para,T1}$ , respectively, until the upper boundary of the conducted emissions frequency range,  $f_H$ . From these conditions, the boundaries for the  $C_{para,M3}$  and  $C_{para,T1}$  can be extracted as,

$$C_{para,M3} < \frac{1}{2\pi f_H \left(1 + \frac{2R_L g_m}{1 + R_E g_m}\right) \left(R_f \parallel \frac{Z_\pi}{1 + \alpha} (1 + R_E g_m)\right)} \quad (3.47)$$

$$C_{para,T1} < C_{inj} \quad (3.48)$$

The boundaries of (3.47) and (3.48) are calculated as 500pF and 1.5nF for the designed AEF circuit, respectively. To validate the effects of  $C_{para,M3}$  and  $C_{para,T1}$  on the AEF performance, the  $NA$  was calculated with varying the value of each parasitic capacitance from 0.25 nF to 2.25 nF, as shown in Fig 3-12. When the values of  $C_{para,M3}$  and  $C_{para,T1}$  approach the boundaries of (3.47) and (3.48), the performance of the VSCC AEF is actually degraded.  $C_{para,T1}$  has a larger effect on the performance degradation than  $C_{para,M3}$ , and the protection circuit in the collector side should be more carefully selected.

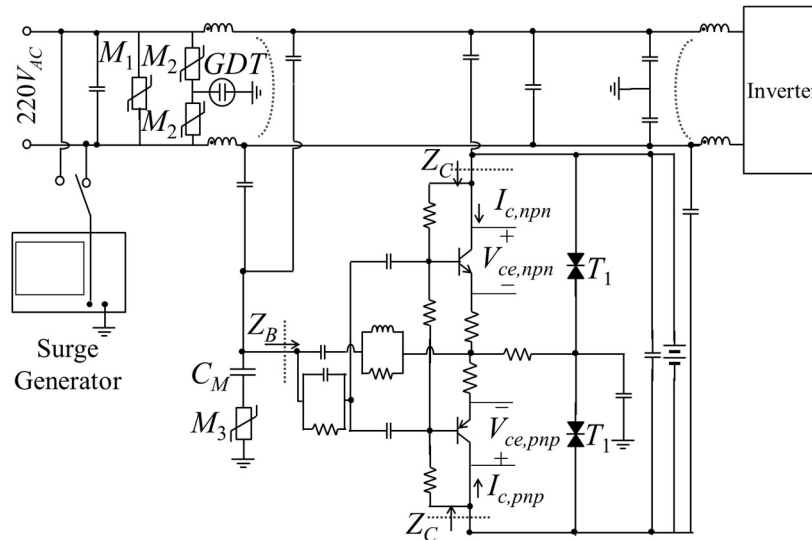


Fig 3-11. The proposed surge protection circuits for the AEF



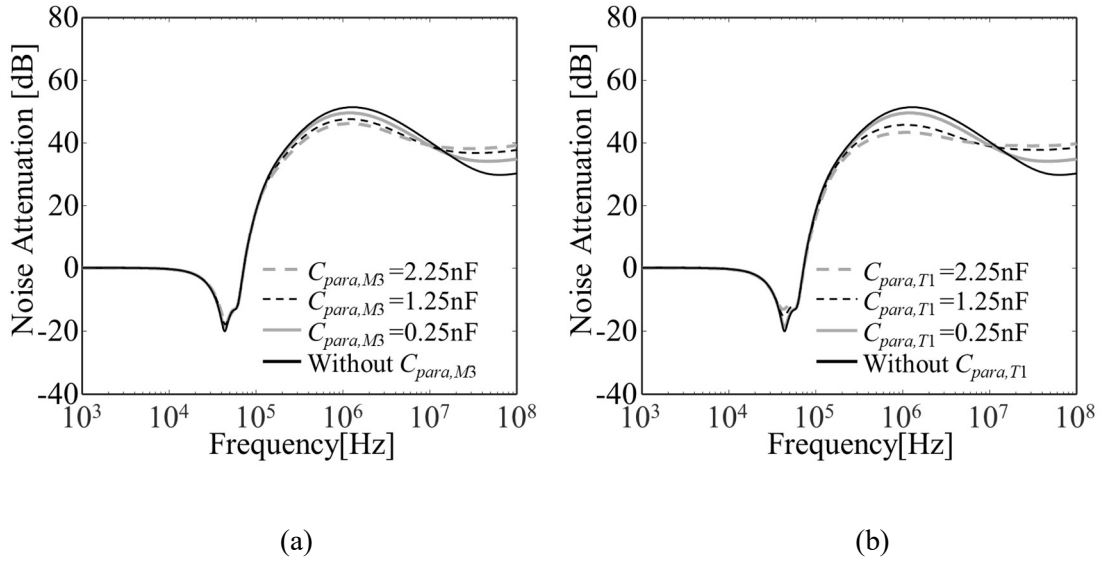


Fig 3-12. The  $NA$  according to the parasitic capacitance in the (a) varistor,  $M_3$  and (b) TVS diode,  $T_1$

## 3.5. Implementation and Measurements of the VSCC AEF

### 3.5.1. Design Flow and Implementation

The design flow for the VSCC AEF is summarized in Fig3-13. Assume that maximum allowable Y-capacitance,  $C_{Y,max}$ , and the CM chokes to be used are given prior to the design of AEF. The  $f_{op}$  frequency is just chosen to be sufficiently lower than the low boundary of the conducted emissions frequency range. The equivalent capacitance of the CM noise source,  $C_n$ , can be extracted from the measured conducted emissions of the EUT [35]-[37]. At Step1 of Fig 3-13, the  $C_{inp}$ ,  $C_{sen}$ ,  $C_{inj}$ , and  $C_{DC}$  are designed from (3.20), (3.26) and (3.27). At Step2, the BJTs are chosen based on (3.28) and (3.29), and the bias and output components of the AEF,  $R_{bias}$ ,  $R_p$ ,  $R_L$ , and  $C_L$ , are determined using (3.30)-(3.32). The damping circuits are then designed at Step3. The parallel resonance frequency  $f_{res,p}$  is calculated first, with the designed values of  $L_{cm2}$ ,  $C_{sen}$ ,  $C_{inj}$ , and  $R_{bias}$  using (3.39). The damping branch composed of  $L_f$ ,  $R_f$ , and  $C_f$  are designed using (3.40), (3.41), and (3.43). Then, the other damping branches for  $R_{in}$  and  $C_{in}$  are determined using (3.38) and (3.42). After the prototype design of the damping circuits, the stability of the overall filter with the VSCC AEF should be confirmed by checking the phase of the loop gain. If the VSCC AEF is unstable, the damping circuits should be re-designed after increasing  $R_{in}$  or  $C_{in}$ . At Step4, the surge protection circuits are employed according to the design rules of (3.45)-(3.48).



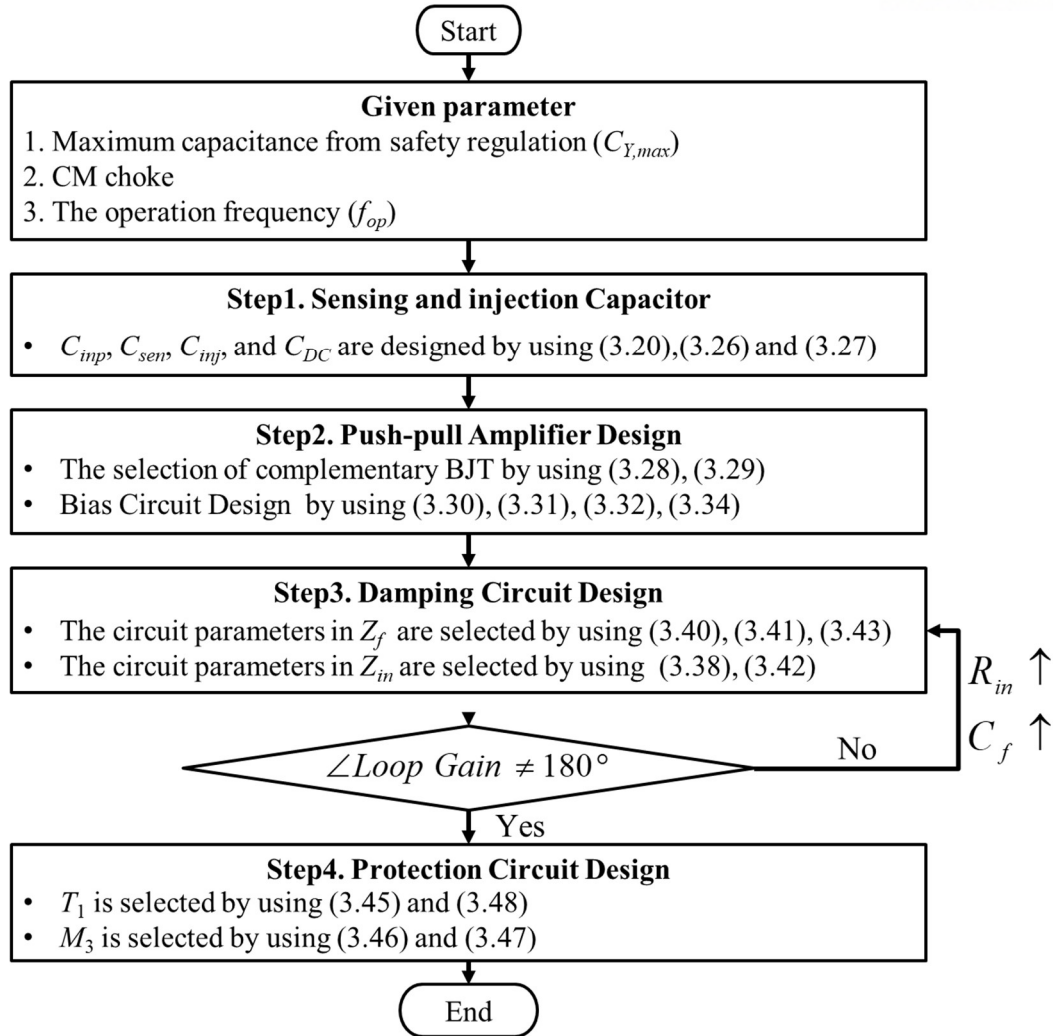


Fig 3-13. Design flow of the VSCC AEF

The total EMI filter with the VSCC AEF has been designed according to the design flow, and then manufactured in a printed circuit board (PCB) at a size of 53 mm by 53 mm, as shown in Fig 3.14. All component values in the VSCC AEF are summarized in Table 3-1. In the VSCC AEF, the high voltage rating Y-type capacitors were used for the capacitors connected to the power lines,  $C_{inj}$ ,  $C_{sen}$ , and  $C_{inp}$ , which have a relatively large tolerance. It has been validated by simulations that the performance and stability are rarely affected by the change of Y-capacitor values within 20% tolerance. They are not main contributors to the performance or stability of the AEF. The circuit models of the CM choke are extracted using the VNA measurements. The BJTs, KSA473 and KSC1173, and the surge protection circuits, P6KE22CA and V05E95P, have been used, respectively. The  $V_{T1}$  and  $V_{M3}$  of the protection circuits are 22V and 150V, respectively. The  $C_M$  is set as  $1\mu\text{F}$ . In

the product example, a DC 18V supply voltage for the VSCC AEF was available from the control board of the main power system, which is usually the case in real products. Otherwise, a proper DC power supply should be separately implemented for the AEF. When a DC 18V is supplied for the power of the AEF, the average operating current of the VSCC AEF is measured as 16mA. Accordingly, the total power consumption of the operating AEF is about 288mW in average. The power loss due to all passive resistors in the AEF was also found by measuring the applied voltages at each resistor, which was calculated as 12.4mW. As results, the power loss due to the passive resistors is quite small as about 4.3% of the total power consumption of the AEF.

Table 3-1. Components Values of The VSCC Active EMI Filter

Components	Values
$C_{sen}, C_{inj}, C_b, C_{inp}, C_{DC}$	1.5 nF, 1.5 nF, 1 $\mu$ F, 0.47nF 2.2 $\mu$ F
$R_{bias}, R_p$	33 k $\Omega$ , 7.7 k $\Omega$
$R_e, R_L, C_L$	2 $\Omega$ , 2.2 $\Omega$ , 140 nF
$R_{in}, C_{in}$	200 $\Omega$ , 5 nF
$R_f, C_f, L_f$	330 $\Omega$ , 30 nF, 200 $\mu$ H
$L_{cm1}, R_{cm1}, C_{cm1}$	8 mH, 80 k $\Omega$ , 10 pF
$L_{cm2}, R_{cm2}, C_{cm2}$	1 mH, 4 k $\Omega$ , 16 pF

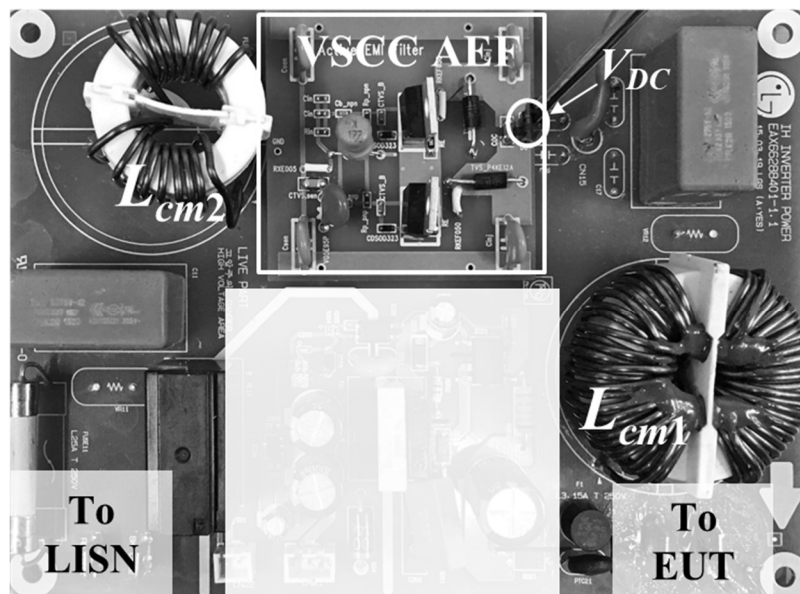


Fig 3-14. Photograph of the total EMI filter with the VSCC AEF

### 3.5.2. VNA Measurements for Performance Validation

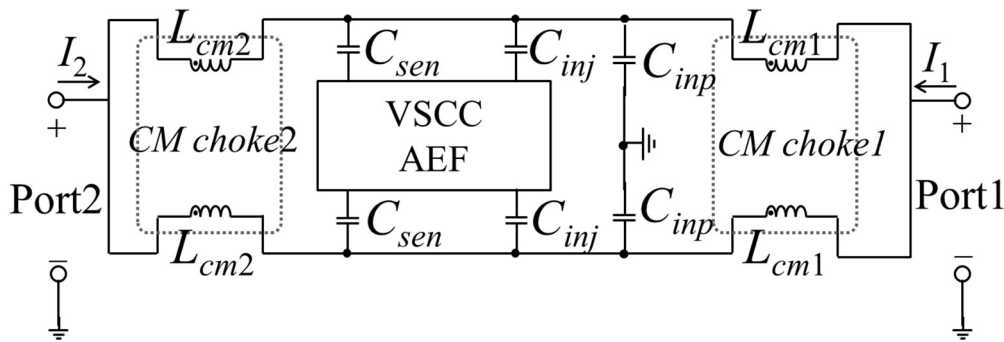
The performance of an EMI filter can be estimated from VNA measurements. The EMI filter with the VSCC AEF is compared to the filter with passive Y-capacitors. The value of the passive Y-capacitor,  $C_Y$ , is set as the sum of  $C_{sen}$ ,  $C_{inj}$ , and  $C_{inp}$ , which are utilized in the filter with the VSCC AEF.

In the VNA measurements, the noise source and noise receiver are assigned as Port1 and Port2, respectively, as shown in Fig 3-15(a). The  $S_{21}$  parameters representing the propagated signal from Port1 to Port2 are measured and plotted in Fig 3-15(b). The  $S_{21}$  simulated by SPICE is also plotted, validating the modeling accuracy up to 10 MHz. By employing an AEF in the EMI filter instead of the passive Y-capacitor, the  $S_{21}$  is reduced by about 10~20 dB in a frequency range from 100 kHz to 6MHz, as shown in Fig 3-15(b).

The  $NA$  can also be extracted from the Z-parameters measured by the VNA as

$$NA = -\frac{I_1}{I_2} = -\frac{Z_{LISN} + Z_{11}}{Z_{12}} \quad (3.49)$$

where the  $I_1$  and  $I_2$  represent the input currents at Port1 and 2, respectively. The  $NA$  extracted from the VNA measurement is also compared to that which was simulated by SPICE in Fig 3-15(c). The simulated  $NA$  is exactly the same as those calculated using (3.18) and (3.19). The  $NA_{AEF}$  is higher than  $NA_{Y-cap}$  by about 10~20 dB in a frequency range from 100 kHz to 6 MHz, which correlates with the  $S_{21}$  comparison.



(a)

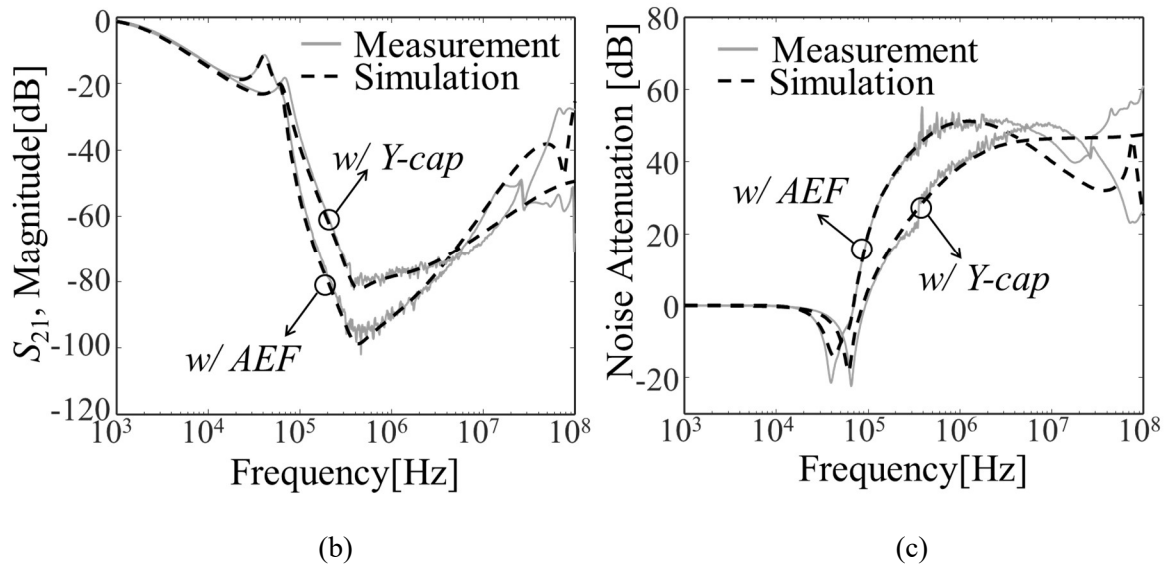


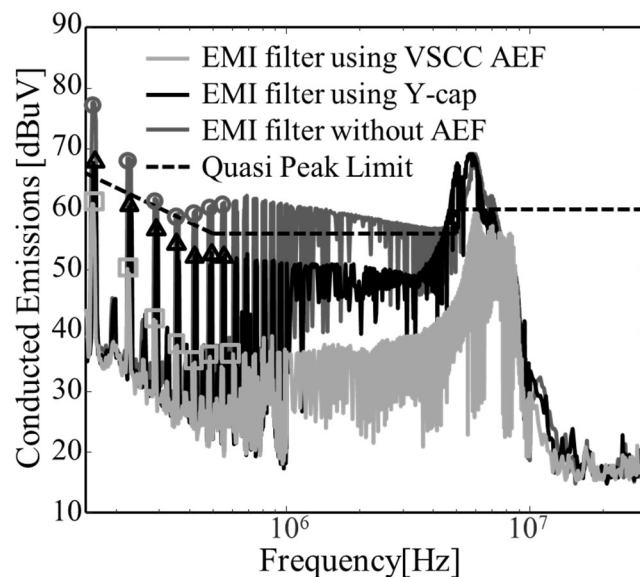
Fig 3-15. (a) Schematic of a VNA measurement (b)  $S_{21}$  parameter with the prospected AEF and with the PEF (c) Measured  $NA$  with the VSCC AEF and with the PEF

### 3.5.3. Measurement in a Real Application in a Product

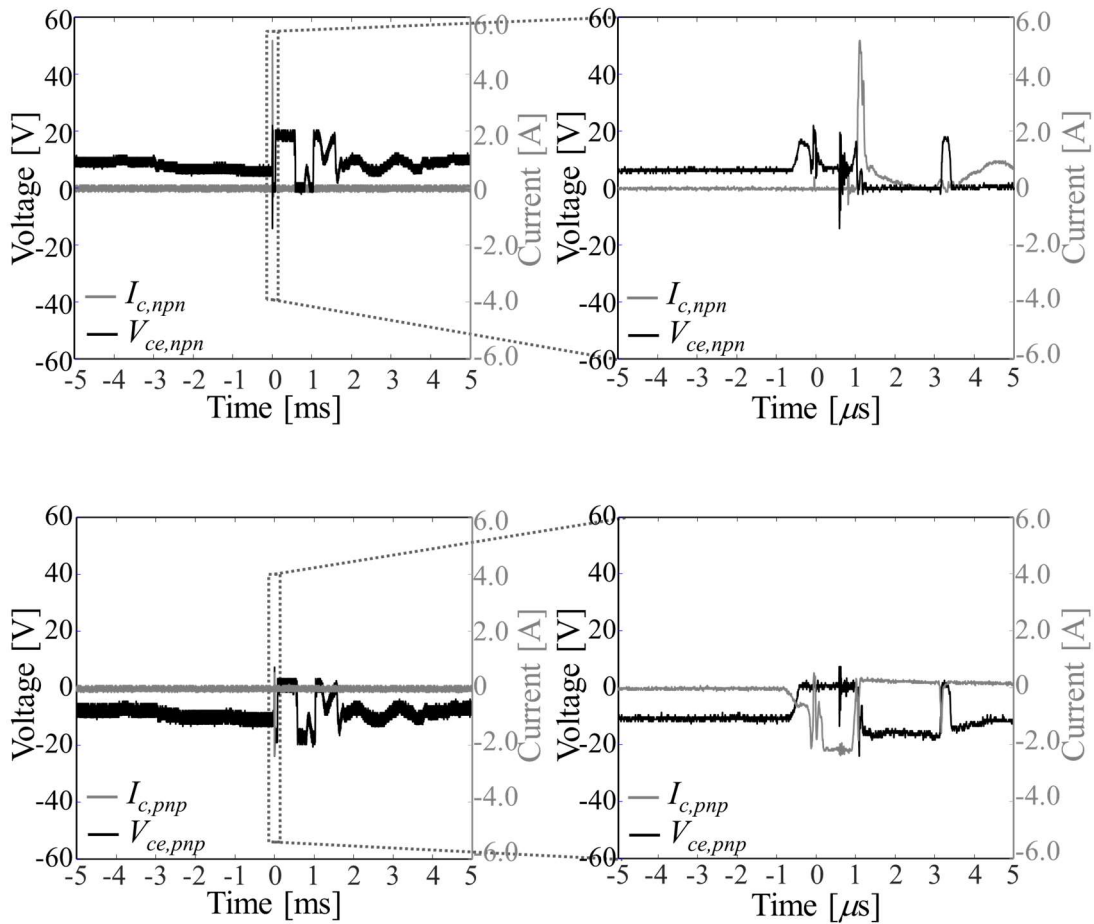
The EMI filter with the VSCC AEF was installed in front of the 2.2 kW current resonance inverter in a commercial product. For comparison, the filter with the passive Y-capacitors and the filter without either the AEF or Y-capacitors have also been tested in the same setup. The CM-conducted emissions for all cases are measured by using LISN, CM/DM separator, and spectrum analyzer in the frequency range from 150 kHz to 30 MHz, as shown in Fig 3-16(a). After applying the EMI filter with the VSCC AEF to the real product, the conducted emissions are attenuated by about 5 to 25 dB in the frequency range from 150 kHz to 6 MHz as compared to the case without any filter. The case of the EMI filter with the AEF also shows less conducted emissions than that with the Y-capacitors by about 5 to 15 dB from 150 kHz to 6 MHz, which is consistent with the results from VNA measurements. The EMI filter with the VSCC AEF has effectively reduced the CM conducted emissions below the quasi-peak limit of the CISPR- Class B regulation, as shown in Fig 3-16(a). However, the EMI peaks at about 7MHz are not much decreased by the AEF. The high EMI peaks at a narrow frequency band above several MHz are usually attributed to the resonance between the noise source impedance and a shunt capacitance to the GND. Thus, the EMI filter can rarely suppress the resonance, but is involved in the resonance. Accordingly, an additional method should be necessary to suppress the 7-MHz conducted emissions under the regulations with a sufficient margin.

At the resonance frequency between the noise source impedance and the EMI filter, the conducted emissions are highly related to the quality factor of the resonance path. Therefore, a damping component suppressing the resonance can effectively reduce the EMI peaks. A ferrite bead is commonly utilized as the damping component [1]. An impedance mismatching filter consisting of a CM choke and a resistor has also been introduced in [38]. Furthermore, adding a Y-capacitor at the LISN side is also a possible solution to improve the noise attenuation at the high-frequencies, which modifies the total EMI filter topology of the L-C-L configuration to the double L-C filter.

The low frequency CM conducted emissions are usually more difficult to reduce when using the passive EMI filters, which require larger and expensive CM chokes. Hence, the VSCC AEF has been designed in the purpose to demonstrate the reduction of conducted emissions predominantly in the low frequency range. As result, the conducted emissions have been effectively attenuated by the AEF without increasing the leakage current and adding any bulky CM chokes.



(a)



(b)

Fig 3-16. (a) CM conducted emissions measurement result (b) BJT voltages and currents measured during the lightning surge test

To demonstrate the protection circuits, the BJT voltages and currents were measured while the CM surge test was being performed, as shown in Fig 3-11. The 2 kV peak,  $1.2 \mu\text{s} / 50 \mu\text{s}$  open-circuit voltage and the  $8 \mu\text{s} / 20 \mu\text{s}$  short-circuit current is generated by the surge generator (UCS 500N) [39]. After the CM surge voltage is excited, the voltages between collector and emitter at each BJT,  $V_{ce,npn}$ , and  $V_{ce,pnp}$  fluctuate but do not exceed  $V_{T1}$  due to the behavior of  $T_1$ , as shown in Fig 3-16(b). The BJT collector currents,  $I_{c,npn}$  and  $I_{c,pnp}$ , are also induced but do not exceed the rate of the BJTs.

Also, when the BJT collector current flows, the  $V_{ce,npn}$  or  $V_{ce,pnp}$  decreases near 0V due to the voltage drop at  $R_e$ , as shown in Fig 3-16(b). Accordingly, the power dissipation at the BJTs are quite low, falling below the safe operating area. Thus, the VSCC AEF can withstand the high-voltage transient

and behaved well after the surge tests.

### 3.6. Summary

The novel features of the VSCC AEF can be characterized as 1) the push-pull amplifier with the low voltage rating BJTs, 2) transformer-less, and 3) direct analog noise sensing. The AEF was completely analyzed and expressed by the block diagram based on a circuit analysis. The loop gain has been effectively extracted from the block diagram to determine the system stability.

Quantified practical design guidelines were rigorously derived from the analysis with considerations for both performance and stability. For practical applications in commercial products, immunity to high voltage transient also was taken into account, and the design rules of the protection circuits were presented. The design flow of the AEF was built based on the extracted design rules. The total EMI filter with the VSCC AEF was designed according to the design flow and implemented in a compact size PCB. The performance of the filter with AEF was verified with VNA measurements. The AEF was applied to a commercial product with the 2.2 kW current resonance inverter, and the CM conducted emissions were effectively attenuated by about 5 - 25 dB from 150 kHz to 6 MHz without increasing the leakage current or adding any bulky CM chokes. The immunity of the VSCC AEF was also demonstrated with the 2 kV CM surge tests.

Structurally, the transformer-less AEF is free from the magnetic saturation caused by a high current, and can be easily built in a compact size. The VSCC AEF shows promise in resolving the size and cost problems of the EMI filter due to CM chokes, especially in high power applications. Since immunity against high voltage transients was also verified, the VSCC AEF is ready to be applied in real-world fields.



## Chapter IV

# Design Guide of the Feed-Forward Current Sense Current Compensation Active EMI filter

### 4.1. Introduction

The current sense current compensation (CSCC) AEF using the sensing transformer designed as a small number of turns has been suggested in [40]. By utilizing the low-turns sensing transformer, the degeneration due to the parasitic capacitance in the sensing transformer and the core magnetic saturation can be suppressed. However, the total EMI filter with the CSCC AEF in [40] is not practical structure since the other passive filters corresponding to CM chokes and Y-capacitors at the utility side were not included, and their effects were not investigated. In addition, the high-voltage BJTs are required since the rectified AC voltage is utilized for the DC supply voltage of the CSCC AEF in [40]. For the practical application and high noise attenuation, the other passive components at the utility size should be employed, and the low-voltage BJTs should also be available for the push-pull amplifier to reduce the cost of the total EMI filter. Furthermore, the effect of the CSCC AEF on the total system should be examined regarding the stability when the CSCC AEF is implemented in the real product.

In this chapter, the proposed CSCC AEF is employed in the practical structure as L-C-L structure. The amplifier of the proposed CSCC AEF is designed through the low-voltage BJTs. Moreover, the total EMI filter with the proposed CSCC AEF is complete analyzed regarding the performance and stability. The design factors are extracted from the circuit analysis with reasonable assumptions, and then the proposed CSCC AEF is manufactured by using the design guidelines. The performance of the proposed CSCC AEF is demonstrated in the measurements using the vector network analyzer and the CM conducted emissions measurements.

### 4.2. Analysis of the EMI Filter with the CSCC AEF

#### 4.2.1. The limitation of the Standalone feed forward CSCC AEF

The EMI filter should be designed as the symmetric structure regarding the earth GND. The asymmetric structure due to the tolerance of Y-capacitor or the inductance difference between power



line can cause the transformation from the DM noise to the CM noise [41]. It can also lead the EMI filter to over design by increasing the number of CM chokes or Y-capacitor. Accordingly, the designers should have an effort to design the symmetric EMI filter as possible as to avoid the unbalance problem.

The Standalone type CSCC AEF in [40] has been designed as the directed connect to the part of power lines for the DC supply voltage as shown in Fig 4-1(a). The compensation behavior is carried out at the connected power lines by injecting the compensating current  $i_{inj}$  as shown in Fig 4-1(a). Accordingly, the unbalance problem can occur between the connected and disconnected power lines with the CSCC AEF in Fig 4-1(a) and cause the DM noise to convert the CM noise [41].

For the balanced structure, the sensing noise and compensation signal should be performed to all of the power lines simultaneously. Therefore, the sensing parts and compensation part have be associated with all of the power lines through the inductive or capacitive coupling. The injection capacitors,  $C_{inj}$ , are implemented between the BJT collector and each power line. The additional DC power supply is used for the supply voltage of the push-pull amplifier, as shown in Fig 4-1(b).

Although the AEF is separated from the power lines in the low-frequency range due to the high-impedance of  $C_{inj}$ , the noise compensation can be performed at all power lines through  $C_{inj}$  and the operation of the CSCC has effects on all power lines in the conducted emissions frequency range. Hence, the symmetric EMI filter with the feed-forward CSCC AEF can be achieved by using the capacitive coupling. For the more investigation, the issue about the asymmetric EMI filter due to AEF will be experimentally analyzed in the single-phase system in Section 4.4.4.

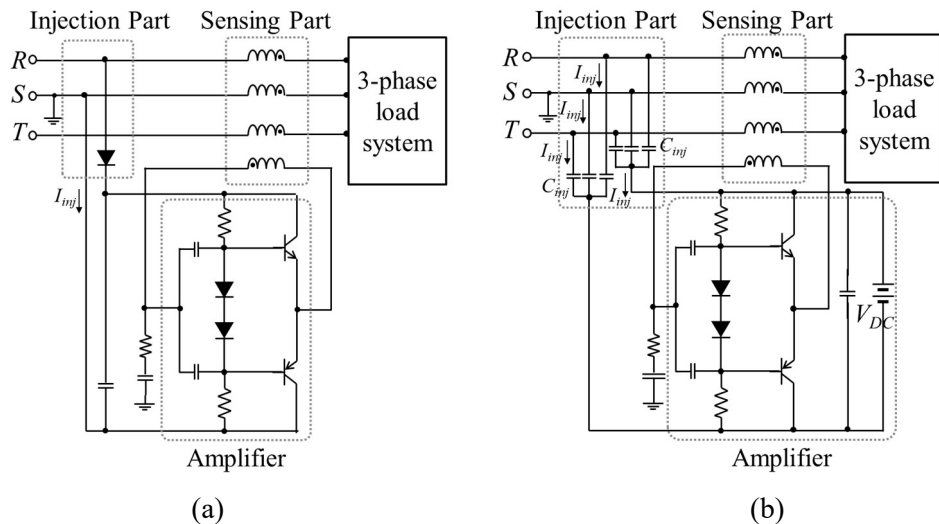


Fig 4-1. Comparison between (a) the standalone type AEF in [40] and (b) the proposed CSCC AEF with  $C_{inj}$

### 4.2.2. Circuit analysis of the CSCC AEF

The total EMI filter with the proposed AEF is designed for the single-phase power system as the L-C-L filter which is one of the general structures in the EMI filter as shown in Fig 4-2(a). For the analysis of the proposed AEF, the CM chokes are modeled as the parallel resistance, capacitance, and inductance.  $L_{cm1}$ ,  $M_{cm1}$ ,  $C_{cm1}$ , and  $R_{cm1}$  ( $L_{cm2}$ ,  $M_{cm2}$ ,  $C_{cm2}$ , and  $R_{cm2}$ ) correspond to the self-, mutual inductance, equivalent parallel capacitance, and equivalent parallel resistance, respectively. The injection capacitor, Y and X-capacitor are designated as  $C_{inj}$ ,  $C_Y$ , and  $C_X$ , respectively.  $C_b$ ,  $C_e$ , and  $C_o$  represent the DC block capacitor at the base side, the bypass capacitor at the emitter, and the load capacitor, respectively.  $R_{bias}$ ,  $R_e$ , and  $R_o$  indicate the bias resistor, degeneration emitter resistor, and load resistor, respectively. The push-pull amplifier is biased as the class AB to avoid the crossover distortion through two diodes  $D_1$  and  $R_{bias}$ . The damping resistor  $R_d$  is inserted between  $L_{sen}$  and  $C_b$  to prevent the system instability.

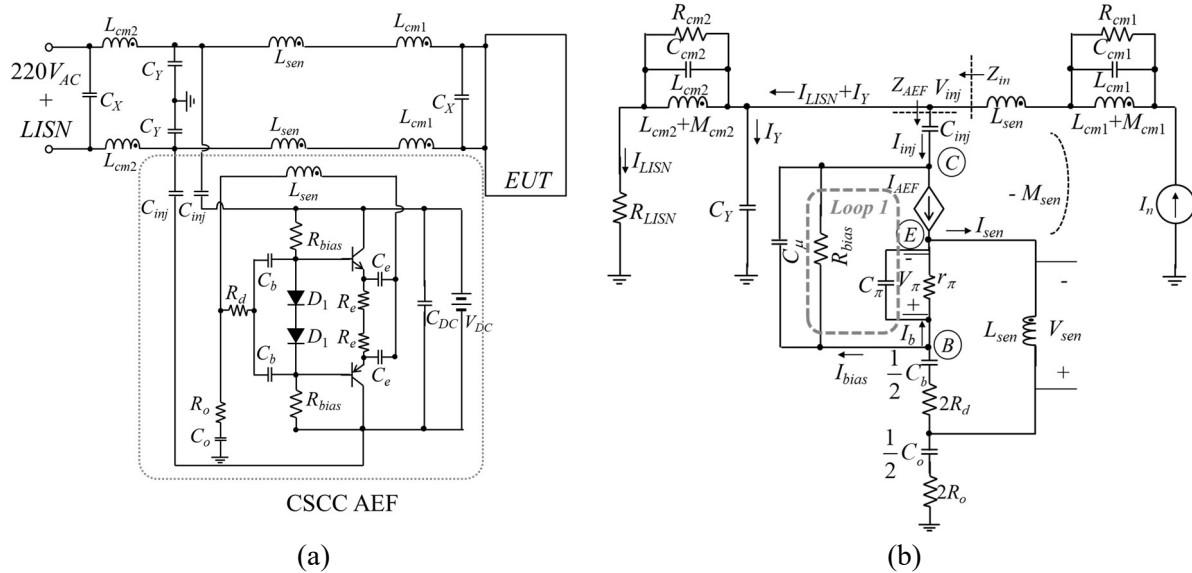


Fig 4-2. (a) L-C-L EMI filter with the proposed CSCC AEF (b) the equivalent circuit model of the EMI filter with the AEF

The analysis of the EMI filter with the AEF can be carried out by the half portion regarding the earth GND due to the symmetric structure concerning the earth GND. The equivalent circuit model of the EMI filter with the AEF is established by applying to the circuit model of each component including active components as shown in Fig 4-2(b).

In the analysis, the BJTs are modeled as the voltage controlled current source, base resistor,

junction capacitors. For the simplification, the effects of parasitic resistance and capacitance in the sensing transformer can be ignored in the conducted emissions frequency range, because, the impedance determined by the  $L_{sen}$  and  $M_{sen}$  is much smaller than  $R_{sen}$  and  $C_{sen}$  due to the negative inductive coupling, as  $s(L_{sen}-M_{sen})$ . The impedance by the  $L_{sen}$  and  $M_{sen}$  is predominantly responsible to the sensing transformer impedance in the conducted emissions.

By using KCL along *Loop1*, and KVL from the connecting node with  $C_{inj}$  to the earth GND in Fig 4-2(b), the ratio of  $I_{bias}$  to  $I_b$ , which designated as  $\alpha$ , is expressed as

$$\frac{I_{bias}}{I_b} = \alpha = \frac{Z_\pi + Z_d - sM_{sen}Z_\pi g_m + sL_{sen}(1 + Z_\pi g_m) + sM_{sen} \frac{Z_d - (Z_{inj} + Z_o)Z_\pi g_m}{(Z_{LISN} + Z_{cm2}) \parallel Z_Y}}{- (sM_{sen} + Z_d) - sM_{sen} \frac{(Z_{inj} + Z_{bias} + Z_d + Z_o)}{(Z_{LISN} + Z_{cm2}) \parallel Z_Y}} \quad (4.1)$$

Where

$$Z_\pi = r_\pi \parallel \frac{1}{sC_\pi}, \quad Z_d = \frac{2}{sC_d} + 2R_d, \quad Z_{inj} = \frac{1}{sC_{inj}}, \quad Z_o = 2R_o + \frac{2}{sC_o}, \quad Z_\pi = r_\pi \parallel \frac{1}{sC_\pi},$$

$$Z_Y = \frac{1}{sC_Y}, \quad Z_{cm2} = R_{cm2} \parallel s(L_{cm2} + M_{cm2}) \parallel \frac{1}{sC_{cm2}}, \quad Z_{bias} = R_{bias} \parallel \frac{1}{sC_\mu}.$$

By solving the equivalent circuit model in Fig 4-2 (b), each current can be expressed through  $I_b$  and  $\alpha$  as,

$$I_n = I_{inj} + I_{LISN} + I_Y \quad (4.2)$$

$$I_{inj} = (Z_\pi g_m - \alpha) I_b \quad (4.3)$$

$$I_e = Z_\pi g_m I_b \quad (4.4)$$

$$I_{LISN} + I_Y = \frac{V_{inj}}{Z_Y \parallel (Z_{cm2} + Z_{LISN})} \quad (4.5)$$

$$V_{inj} = (Z_{inj} + Z_o) I_{inj} - (Z_{bias} + Z_d) I_{bias} - Z_d I_b \quad (4.6)$$

The block diagram of the EMI filter with the AEF can be constructed based on (4.2)-(4.5) for the effective investigation of the performance and the loop gain extraction, as shown in Fig 4-3. The EMI filter with the AEF can be considered as series-shunt feedback system since the summing and sampling are realized by the current through  $C_{inj}$  and the sensing transformer. Accordingly,  $I_n$  and  $I_{inj}$  are set as the input and output in the block diagram, respectively. The  $A$  corresponds to the forward transfer function, which is the ratio of  $I_{inj}$  to  $(I_{LISN}+I_Y)$ .

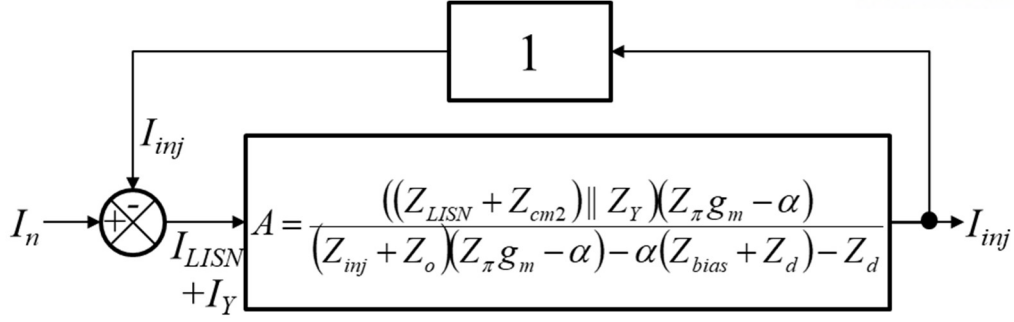


Fig 4-3. The block diagram of the EMI filter with the AEF

### 4.2.3. The Effective Capacitance of the CSCC AEF

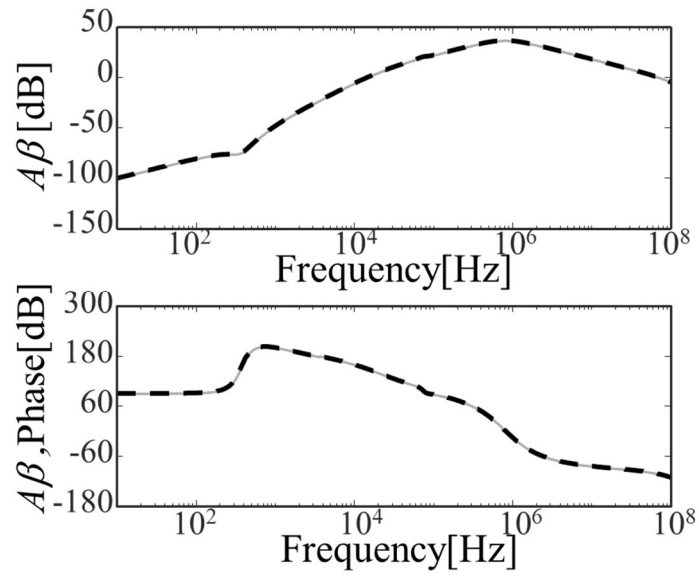
The closed-loop gain of the block diagram in Fig 4-3 can be expressed as

$$A_{i,fb} = \frac{I_{inj}}{I_n} = \frac{A}{1 + A\beta} \quad (4.7)$$

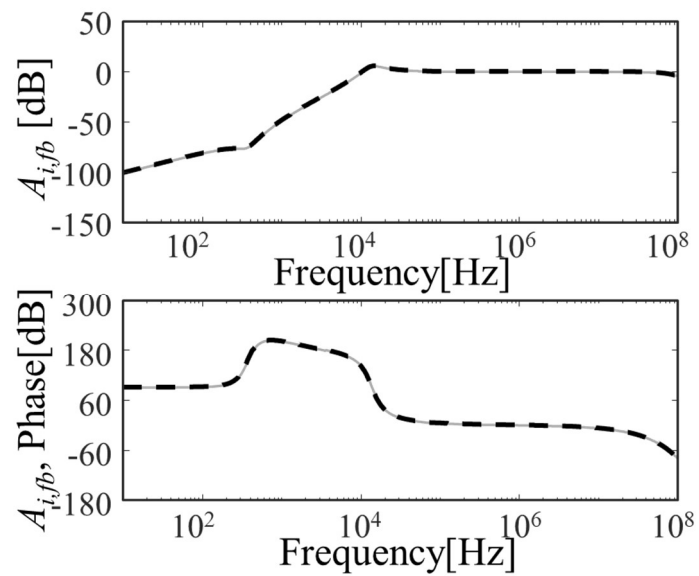
Where

$$A\beta = A = \frac{I_{inj}}{I_{LISN} + I_Y} = \frac{((Z_{LISN} + Z_{cm2}) \parallel Z_Y)(Z_{\pi} g_m - \alpha)}{(Z_{inj} + Z_o)(Z_{\pi} g_m - \alpha) - \alpha(Z_{bias} + Z_d) - Z_d} \quad (4.8)$$

$A_{i,fb}$  and  $A\beta$  represent the closed-loop gain and the loop gain of the EMI filter with the AEF, respectively.  $A\beta$  is determined by the  $A$  since the feedback transfer function,  $\beta$  is '1' as shown in Fig 4-3.  $A_{i,fb}$  and  $A\beta$  are extracted from the SPICE simulation and compared with (4.7) and (4.8) as shown in Fig 4-4. When the  $A\beta$  is much larger than '1',  $A_{i,fb}$  is close to '0 dB' which means that overall amount of  $I_n$  flows into the earth GND through the proposed CSCC AEF and the conducted emissions can be much decreased. There is the risk of the system instability since the phase of  $A\beta$  is crossing at  $180^\circ$ . Accordingly, the designers should confirm the system stability at the end of the design procedure. The system stability of the EMI filter with the AEF can be investigated through gain or phase margin which are calculated based on the  $A\beta$ . The system stability will be explained more in Section 4.3.5.



(a)



(b)

Fig 4-4. Calculation (dotted or dashed) and simulation (solid) results (a) the loop gain (b) the close-loop gain of the EMI filter with the AEF

The loop gain of the total EMI filter affects the input and output impedance variation in the feedback system. Based on the feedback theory, the feedback input impedance can be expressed as

$$Z_{in,fb} = \frac{Z_{in,dis}}{1 + A\beta} = (Z_{LISN} + Z_{cm2}) \parallel Z_Y \parallel Z_{AEF} \quad (4.9)$$

where

$$Z_{in,dis} = (Z_{LISN} + Z_{cm2}) \parallel Z_Y \quad (4.10)$$

$$Z_{AEF} = \frac{V_{inj}}{I_{inj}} = \frac{Z_{in,dis}}{A\beta} = Z_{inj} - \frac{\alpha Z_{bias}}{(Z_{\pi} g_m - \alpha)} \quad (4.11)$$

$Z_{in,dis}$ , and  $Z_{in,fb}$  are designated as the feedback input impedance looking at the injection node without and with the AEF, respectively.  $Z_{AEF}$  represents the impedance seen at the injection node into the GND through the AEF.  $Z_{in,fb}$  and  $Z_{AEF}$  are determined by  $Z_{in,dis}$  and  $A\beta$  in (4.9), and significantly reduced when the  $A\beta$  is much larger than '1'. The operation of the AEF can generate the low-impedance path of the noise current from the power lines to the earth GND if  $A\beta$  has sufficiently large value.  $Z_{in,f}$  and  $Z_{AEF}$  are calculated and plotted in Fig 4-5 (a). After 1kHz,  $Z_{AEF}$  is much decreased as compared to  $Z_{inj}$ . It means that the effective capacitance of  $Z_{AEF}$  is amplified by the operation of the AEF.  $Z_{in,fb}$  is also much smaller than  $Z_{in,dis}$  when  $Z_{AEF}$  screens out  $(Z_{LISN} + Z_{cm2})$ , as shown in Fig 4-5 (a). Accordingly, the CM noise current path can be determined by  $Z_{AEF}$  in the CM conducted emissions frequency range.

The  $f_{res,LC}$  represents the parallel resonance frequency due to  $Z_{cm2}$  and  $C_Y$  in  $Z_{in,dis}$ . Since  $Z_{in,fb}$  and  $Z_{AEF}$  depend on  $Z_{in,dis}$ , the parallel resonance of  $Z_{in,dis}$  can produce the impedance peak in  $Z_{in,fb}$  and  $Z_{AEF}$ . This resonance can also cause the performance of the AEF to degrade at  $f_{res,LC}$  by increasing  $Z_{AEF}$ .

To verify the performance of the EMI filter with the AEF, the noise attenuation, which is the criteria of the filter performance, is calculated as

$$NA_{AEF} = \frac{I_{LISN,w/oAEF}}{I_{LISN,w/AEF}} = \frac{Z_{cm2} + Z_{LISN} + Z_{AEF} \parallel Z_Y}{Z_{AEF} \parallel Z_Y} \quad (4.12)$$

$I_{LISN,w/oAEF}$  and  $I_{LISN,w/AEF}$  correspond to  $I_{LISN}$  without and with the EMI filter including the AEF.  $NA_{AEF}$  represents the noise attenuation of the proposed AEF.

For the evaluation of the AEF performance, the noise attenuation by the EMI filter composed of the passive components only in Fig 4-2, is also calculated as

$$NA_{PEF} = \frac{I_{LISN,w/PEF}}{I_{LISN,w/oPEF}} = \frac{Z_{cm2} + Z_{LISN} + Z_{inj} \parallel Z_Y}{Z_{inj} \parallel Z_Y} \quad (4.13)$$

$NA_{PEF}$  indicates the noise attenuation of the PEFs composed of CM chokes,  $C_Y$  and  $C_{inj}$ .  $I_{LISN,w/oPEF}$  and  $I_{LISN,w/PEF}$  are indicated as  $I_{LISN}$  with and without the PEFs.  $NA_{AEF}$  is much higher than  $NA_{PEF}$  when  $Z_{in,fb}$  is determined by  $Z_{AEF}$ . The performance of the EMI filter with the AEF depends on the

impedance variation of  $Z_{AEF}$  as shown in Fig 4-5. Thus, the design guideline of the AEF related to the performance can be extracted from the investigation of  $Z_{AEF}$ .

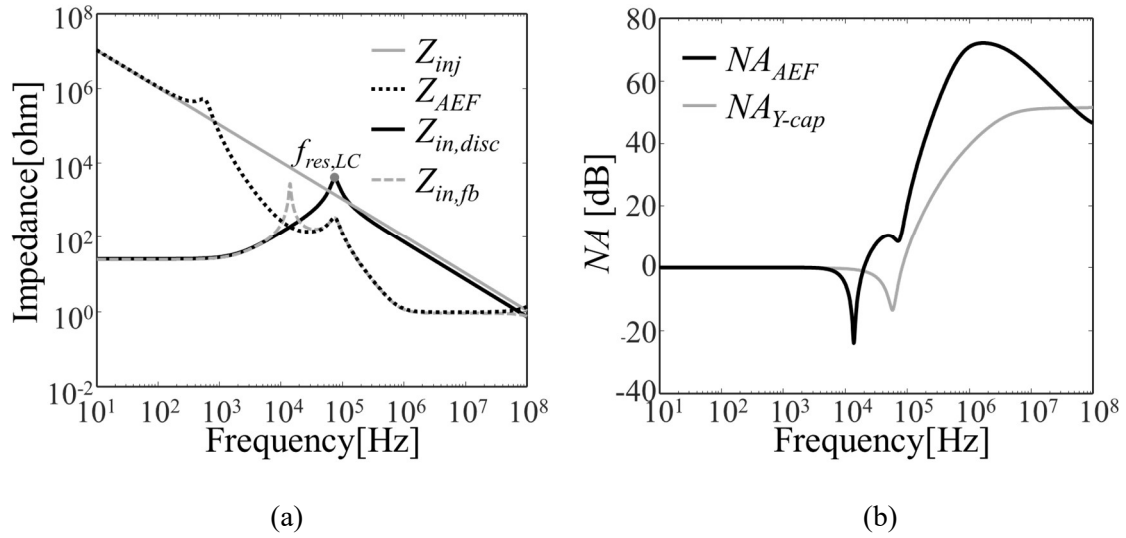


Fig 4-5. (a) The feedback input impedance,  $Z_{in,fb}$  and the impedance of the AEF part,  $Z_{AEF}$  (b) The  $NA$  with the AEF and with Y-capacitors

### 4.3. Design Guidelines of the CSCC AEF

In this section, the equations are simplified to develop the design guidelines by the reasonable assumption, and the useful design rules for each component has been extracted. The damping circuit is also included in the design guidelines for the stable system based on the stability analysis of the EMI filter with the AEF.

#### 4.3.1. Approximation of the Expressions and $f_{op}$

Although each current and impedance can be expressed by the circuit parameters as shown in (4.2)-(4.11), it is quite hard to develop the selection rules of components in the AEF due to the complexity. Accordingly, the approximated equations are necessary to extract the useful design guidelines from the circuit analysis. The sensing transformer is designed as 1 by 1 turn ratio, and  $R_{bias}$  is predominately responsible to  $Z_{bias}$  in the conducted emissions range. For simplification, the much smaller value of  $C_{inj}$  than  $C_o$  is employed in order that the touch current and overall operation in the AEF is predominantly determined by  $C_{inj}$  as compared to  $C_o$ .

By considering as  $L_{sen} \approx M_{sen}$ ,  $Z_{bias} \approx R_{bias}$  and  $Z_{inj} \gg Z_o$ ,  $\alpha$  can be simplified by  $\alpha_{app}$  as,

$$\alpha_{app} = \frac{sM_{sen} Z_{inj} Z_{\pi} g_m}{Z_d ((Z_{LISN} + Z_{cm2}) \parallel Z_Y) + sM_{sen} (Z_{inj} + Z_{bias} + (Z_{LISN} + Z_{cm2}) \parallel Z_Y)} \quad (4.14)$$

$Z_{AEF}$  can be simplified by replacing  $\alpha_{app}$  for  $\alpha$  as,

$$Z_{AEF,app} = Z_{inj} \left( \frac{Z_d ((Z_{LISN} + Z_{cm2}) \parallel Z_Y)}{R_{bias} sM_{sen} + Z_d ((Z_{LISN} + Z_{cm2}) \parallel Z_Y)} \right) \quad (4.15)$$

$Z_{AEF,app}$  corresponds to approximated  $Z_{AEF}$ .

When  $Z_{inj} \ll R_o$  at the high frequency range,  $Z_{AEF}$  can be simplified as,

$$Z_{AEF,high} \approx \frac{1}{g_m k_{sen}} \frac{C_{\pi}}{C_Y} \quad (4.16)$$

$Z_{AEF,app}$  can be overlapped with  $Z_{AEF}$  in the low-frequency range and the value of  $Z_{AEF}$  approaches to  $Z_{AEF,high}$  as shown in Fig 4-7.

The operation frequency,  $f_{op}$  of the AEF is defined as the frequency at  $Z_{AEF,app} = 0.5Z_{inj}$ . From this condition,  $R_{LISN} \gg Z_{cm2}$  and (4.15),  $f_{op}$  can be expressed as

$$f_{op} = \frac{1}{2\pi} \sqrt{\frac{3R_{LISN}}{C_b R_{bias} k_{sen} L_{sen}}} \quad (4.17)$$

Oppositely,  $Z_{cm2} \ll R_{LISN}$ ,  $f_{op}$  can be written as

$$f_{op} = \frac{\sqrt{3}}{2\pi} \frac{L_{cm2} (1 + k_{cm2})}{C_b R_{bias} k_{sen} L_{sen}} \quad (4.18)$$

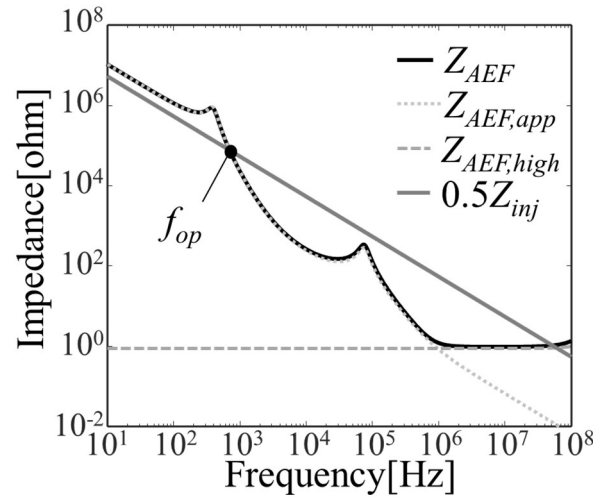


Fig 4-7. Comparison between  $Z_{AEF}$  and  $Z_{AEF,app}$



### 4.3.2. Design Guideline for the sensing transformer

The sensing transformer should be carefully designed since the noise sense depends on the performance of the sensing transformer. The design of the sensing transformer is affected by the EUT operating current in which the EMI filter with the AEF is employed.

The magnetic fluxes in the core of the sensing transformer, which generated by the EUT operating current, cancel out each other. However, the magnetic flux can remain due to the leakage inductance which is the difference between  $L_{sen}$  and  $M_{sen}$ . The magnetic saturation can occur by the remaining magnetic flux [3]-[5]. To prevent the magnetic saturation, the maximum allowable differential current flowing into the sensing transformer should be larger than the EUT operating current as,

$$I_{EUT} < I_{dm,max} \quad (4.19)$$

where

$$I_{dm,max} = \frac{B_m N A_c}{L_{sen,leak}} \quad (4.20)$$

$$L_{sen,leak} = 2(L_{sen} - M_{sen}) = \frac{\mu_{eff} 0.4 N^2 A_c \cdot 10^{-8}}{l_e \sqrt{\theta/360 + \sin(\theta/2)}/\pi} \quad (4.21)$$

$I_{EUT}$  and  $I_{dm,max}$  correspond to the EUT operating current and the maximum allowable differential current without the magnetic saturation.  $B_m$ ,  $A_c$ , and  $N$  are designated as the material saturation flux density, the cross-sectional area of core and the number of turns on the core, respectively.  $\mu_{eff}$ ,  $\theta$  and  $l_e$  are indicated as the effective permeability for leakage flux, winding angle, and effective mean length of the core, respectively. The leakage inductance of the sensing transformer denoted as  $L_{sen,leak}$  can be measured and calculated by (4.21) according to [5].

When the sensing transformer is designed as a large number of turns to obtain high inductance,  $I_{dm,max}$  is more decreased since  $L_{sen,leak}$  is increased by squared  $N$ . Also, the sensing transformer with a large number of turns has the lower bandwidth due to the increase of the parasitic capacitance between wires. Although  $L_{sen}$  and  $k_{sen}$  are included in  $Z_{AEF}$  and  $f_{op}$ , the high inductance of the sensing transformer is not necessary since  $Z_{AEF}$  and  $f_{op}$  can be controlled by other circuit parameter based on (4.15), (4.17) and (4.18). Therefore, each side of the sensing transformer is designed as a small number of turns about 1~5 to avoid the magnetic saturation. Based on the design requirement regarding the AEF size and weight, the core size and weight should be considered as the highest priority since the sensing transformer takes a large portion of the size and weight in the AEF. In addition, the core size is high related with  $I_{dm,max}$  as shown in (4.20).  $A_c$  and  $l_e$  can be determined by

the target AEF size, then, the core material can be selected using desired  $B_m$  and  $i_{dm,max}$ .

### 4.3.3. The selection rule of $C_{inj}$ , $C_Y$ and $C_o$

The large value of the Y-capacitor can result in the electric shock since the touch current, which is the flowing current from power lines to the chassis of a product, rise due to the large value of the Y-capacitor. Accordingly, the Y-capacitors are limited by the safety regulation to avoid the electric shock.

Since the rated voltage from the utility and Y-capacitors are predominantly responsible to the touch current, the maximum value of the Y-capacitor can be expressed as,

$$C_{Y,max} = \frac{I_{touch,limit}}{2\pi f_R V_R} \quad (4.22)$$

$C_{Y,max}$  corresponds to the maximum allowable Y-capacitor in the EMI filter under the touch current limit. The touch current limit, rated frequency, and rated voltage are denoted as  $I_{touch,limit}$ ,  $f_R$ , and  $V_R$ .

When  $f_{op}$  is designed much larger than  $f_R$ , total value of the Y-capacitors in the EMI filter with the AEF is the sum of  $C_{inj}$  and  $C_Y$ . Accordingly, the sum of  $C_{inj}$  and  $C_Y$  should be lower than  $C_{Y,max}$  to avoid the safety issue due to the touch current. From  $C_{Y,max}$ ,  $C_{inj}$  and  $C_Y$  can be selected as,

$$C_Y + C_{inj} < C_{Y,max} \quad (4.23)$$

The resonances of the CM choke and  $C_Y$  at  $f_{res,LC}$  cause the performance of the AEF to degrade by increasing  $Z_{in,dis}$ . The designer should set the  $f_{res,LC}$  lower than the lower boundary of the conducted emissions range,  $f_L$ , to avoid the degradation due to the resonance at  $f_{res,LC}$ . Therefore, the value of  $C_Y$  should be selected as follow

$$C_Y \gg \frac{1}{(2\pi f_L)^2 (L_{cm2} + M_{cm2})} \quad (4.24)$$

As mentioned in the previous section,  $C_o$  is set as quite larger vale than  $C_{inj}$  for the simplification. To satisfy  $Z_o \ll Z_{inj}$ ,  $C_o$  should be chosen as

$$C_o > 10C_{inj} \quad (4.25)$$

### 4.3.4. Design of the push-pull amplifier

The  $f_{op}$  in both (4.17) and (4.18) can be adjusted by  $C_b$ ,  $R_{bias}$  and  $L_{sen}$ .  $C_b$  is much easier to adjust  $f_{op}$  than other parameter since  $L_{sen}$  and  $R_{bias}$  are associated with the magnetic saturation and the BJT biasing. Accordingly,  $C_b$  are utilized to control  $f_{op}$  as,

$$C_b = \begin{cases} \frac{3R_{LISN}}{(2\pi f_{op})^2 R_{bias} k_{sen} L_{sen}}, & R_{LISN} \geq Z_{cm2} \\ \frac{\sqrt{3} L_{cm} (1 + k_{cm})}{2\pi f_{op} R_{bias} k_{sen} L_{sen}}, & R_{LISN} \leq Z_{cm2} \end{cases} \quad (4.26)$$

The push-pull amplifier in the AEF is designed by the complementary BJTs as a class AB to avoid the cross-over distortion. The bandwidth of each BJT should cover the conducted emissions range. In addition, the output current of the BJTs should be larger than the maximum CM current. To satisfy these conditions, the BJT should be selected as,

$$f_T \gg f_H \quad (4.27)$$

$$I_{c,max} \gg I_{n,max} \quad (4.28)$$

The  $f_T$  and  $f_H$  represent the BJT's unity current gain bandwidth and the high boundary of the conducted emissions range frequency, respectively. The  $I_{c,max}$  and  $I_{n,max}$  correspond to maximum output current of the BJT and maximum CM noise current, respectively.

For the class AB amplifier, each BJT in the AEF is biased above the cutoff. Using the forward voltage of  $D_1$ , the push-pull amplifier can be designed as the class AB amplifier. For the BJT biasing, the forward voltage of  $D_1$ ,  $V_F$  should be same or slightly higher than base-emitter on a voltage of the BJT. Accordingly, the selection rule of  $D_1$  can be expressed as

$$V_F \geq V_{BE(ON)} \quad (4.29)$$

The base-emitter on voltage of the BJT is denoted as  $V_{BE(ON)}$ .

The base dc current can be negligible as compared to the flowing dc current into  $D_1$  and  $R_{bias}$ , and the flowing dc current into  $R_{bias}$  and  $D_1$  then can be expressed as

$$I_{BLAS} \approx I_D \approx \frac{V_{DC} - 2V_F}{2R_{bias}} \quad (4.30)$$

$I_{BLAS}$  and  $I_D$  correspond to the flowing dc current into  $R_{bias}$  and  $D_1$ , respectively. For the proper operation of  $D_1$ ,  $I_D$  should be larger than  $I_F$  which is the forward diode current when  $V_F$  is applied into  $D_1$ . Based on (4.30) and  $I_F$ , the design rule of  $R_{bias}$  is extracted as,

$$R_{bias} < \frac{V_{DC} - 2V_F}{2I_F} \quad (4.31)$$

Although the thermal runaway can be prevented by using  $D_1$  which has the same I-V characteristic of BJTs, it is not easy to implement with discrete elements because of the tolerance of components. Accordingly, the risk of the thermal runaway is remaining due to the mismatching between  $D_1$  and BJTs. In the AEF design, the emitter degeneration is utilized by adding  $R_e$  at each emitter to prevent

the thermal runaway. To avoid the thermal runaway, the typical value of  $R_e$  is designed as  $1\sim 4\Omega$ .

When the maximum noise is applied to the input of the push-pull amplifier, the collector-emitter voltage,  $V_{ce}$ , may be close to the saturation region voltage,  $V_{ce(sat)}$ , and the voltage at the BJT emitter becomes  $\pm(V_{DC}/2 - V_{ce(sat)})$ . The maximum output current of the push-pull amplifier,  $I_{o,max}$ , is then generated as  $|V_{DC}/2 - V_{ce(sat)}|/(2R_o)$ . For proper operation,  $I_{o,max}$  should be adjusted to a setting lower than  $I_{c,max}$  by using  $R_o$ . From the relation of  $(V_{DC}/2 - V_{ce(sat)})/(2R_o) \leq I_{c,max}$ , the design guideline of  $R_o$  can be extracted as

$$R_o \geq \frac{1}{2I_{c,max}} \left( \frac{V_{DC}}{2} - V_{ce,sat} \right) \quad (4.32)$$

#### 4.3.5. The system stability and Damping resistor $R_d$

The system instability is an important issue in the feedback system, and the EMI filter with the AEF is also. The stability of the EMI filter with the AEF can be examined through  $A\beta$ . If the phase of  $A\beta$  is  $180^\circ$  and the magnitude=1, the system becomes unstable since the closed-loop gain is infinity. Although there are two  $180^\circ$  crossing frequencies in the phase of  $A\beta$ , the higher frequency is only considered as the frequency which can threaten the system stability since the magnitude of  $A\beta$  is much smaller than '1' at the lower  $180^\circ$  crossing frequency as shown in Fig 4-4(a).

By substituting  $\alpha$  with  $\alpha_{app}$ ,  $A\beta$  can be simplified as,

$$A\beta_{app} = \frac{k_{sen}sL_{sen}R_{bias}}{Z_{inj}Z_d} \quad (4.33)$$

$A\beta_{app}$  represents the approximated loop gain using  $\alpha_{app}$ .  $R_{bias}$  replaces for  $Z_{bias}$  in (4.33) since  $Z_{bias}$  is determined by  $R_{bias}$  below the conducted emissions frequency range. The system instability can occur at the resonance frequency due to the  $L_{sen}$  and  $C_b$ , because, the resonance between  $L_{sen}$  and  $C_b$  causes the phase of  $A\beta$  to be crossing at  $180^\circ$ . Accordingly, the  $180^\circ$  crossing frequency, which causes the system instability, can be expressed as,

$$f_{180} = \frac{1}{2\pi} \sqrt{\frac{1}{C_d L_{sen}}} \quad (4.34)$$

The large value of  $R_b$  can release the system instability since the magnitude of  $A\beta$  at  $f_{180}$  can be reduced. The gain margin, which is defined as  $|1/A\beta|$ , is calculated to estimate the effect of  $R_d$  on the stability and plotted in Fig 4-7 (a). Fig 4-7(a) shows that the higher  $R_d$  allows the higher gain margin.

It means that higher  $R_d$  makes the EMI filter with the AEF more stable. For the investigation of the  $R_d$  effect on the performance, the  $Z_{AEF}$  is also plotted in Fig 4-7(b) according to  $R_d$ , where all other parameter except for  $R_d$  are fixed. Although the  $Z_{AEF}$  is not affected by  $R_d$  in the conducted emissions, the large  $R_d$  can degrade the performance of the AEF when  $f_{180}$  is placed at the conducted emissions frequency range. Accordingly,  $f_{180}$  should be located below the conducted emissions frequency range to avoid the performance degradation.

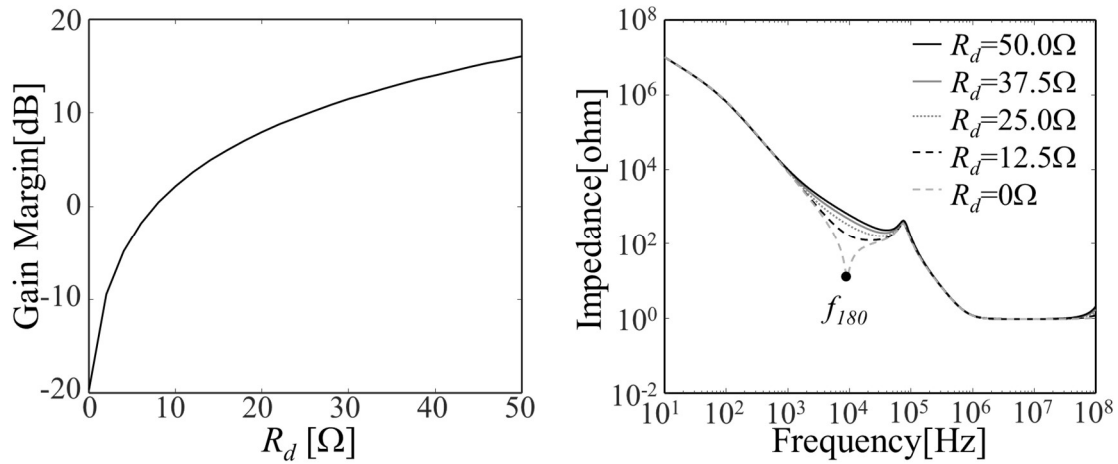


Fig 4-7. (a) The gain margin according to  $R_d$  (b)  $Z_{AEF}$  with variable  $R_d$

## 4.4. The Implementation and Measurement of the EMI Filter with the AEF

Based on the design rules of the AEF, the EMI filter with the AEF is manufactured. The performance of the AEF is validated through the VNA measurements. After employing the EMI filter into 2.2kW current-resonance inverter, the CM conducted emissions are measured and the performance of the AEF is demonstrated.

### 4.4.1. Design Flow and Implementation

The design flow for the EMI filter with the CSCC AEF is summarized in Fig 4-8. The target size and weight of the AEF, CM chokes  $C_{Y,max}$ , and  $f_{op}$  to be used are given before the design of AEF. The  $f_{op}$  should be set as the sufficiently lower than  $f_L$  to achieve maximum noise attenuation at the conducted emissions frequency range. At Step1 of Fig 4-8, the value of  $C_Y$  should be selected by using (4.24) to avoid the degradation due to the resonance between the CM choke and  $C_Y$ . The

selection of  $C_{inj}$  using (4.23) can prevent the safety issue caused by the touch current. The  $C_o$  is designed by using (4.25) so that the operation of the AEF is predominantly determined by  $C_{inj}$ . At Step2, the sensing transformer is developed based on (4.19) and (4.20). The size and weight of the core are predominantly responsible to the volume of the AEF, so that, the physical characteristic of the core should be considered and selected based on the target AEF size and weight. At Step3, the value of  $C_b$  is selected based on target  $f_{op}$  and (4.26). The BJTs are chosen from (4.27) and (4.28), and the bias circuit composed of  $D_1$  and  $R_{bias}$  is designed using (4.29) and (4.31). In addition, the value of  $R_o$  can be extracted from (4.32) to avoid the BJT saturation. After Step3, the system stability should be confirmed based on the gain margin. When the EMI filter with the AEF does not pass the stability check, the higher value of  $R_d$  should be used to achieve the larger gain margin.

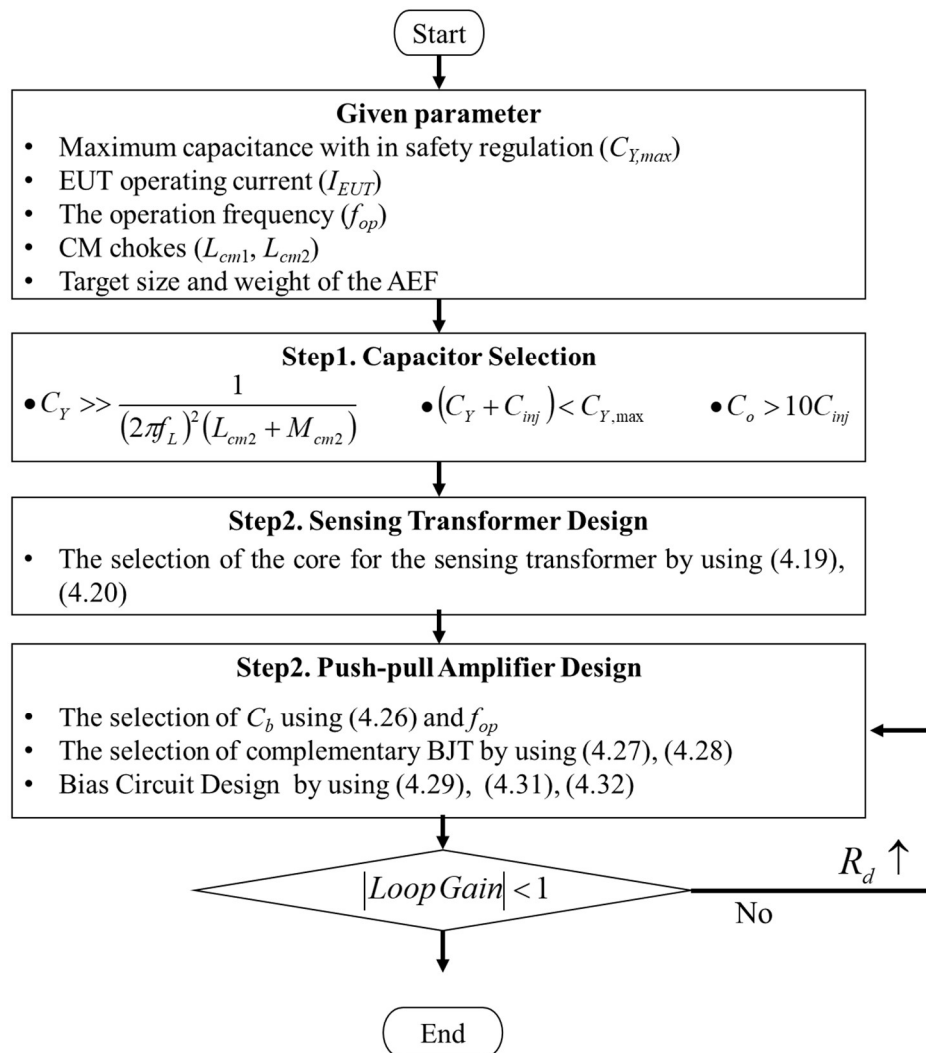


Fig 4-8. The design flow of the CSCC AEF

The EMI filter with the CSCC AEF is realized according to the design flow and then manufactured in a printed circuit board (PCB) at a size of 53 mm by 53 mm, as shown in Fig 4-9. All of the circuit parameters in the total EMI filter are summarized in Table 4-1. Besides, the specifications about the core of the sensing transformer are written in Table 4-2. The BJTs, KSA473, and KSC1173 have been utilized for the push-pull amplifier. For the DC power of the AEF, a DC 18V supply voltage was used from the control board of the main power system. When a DC 18V is applied to the AEF, the average operating current of the proposed AEF is measured as 18mA. Accordingly, the total power consumption of the operating AEF is about 324mW on average.

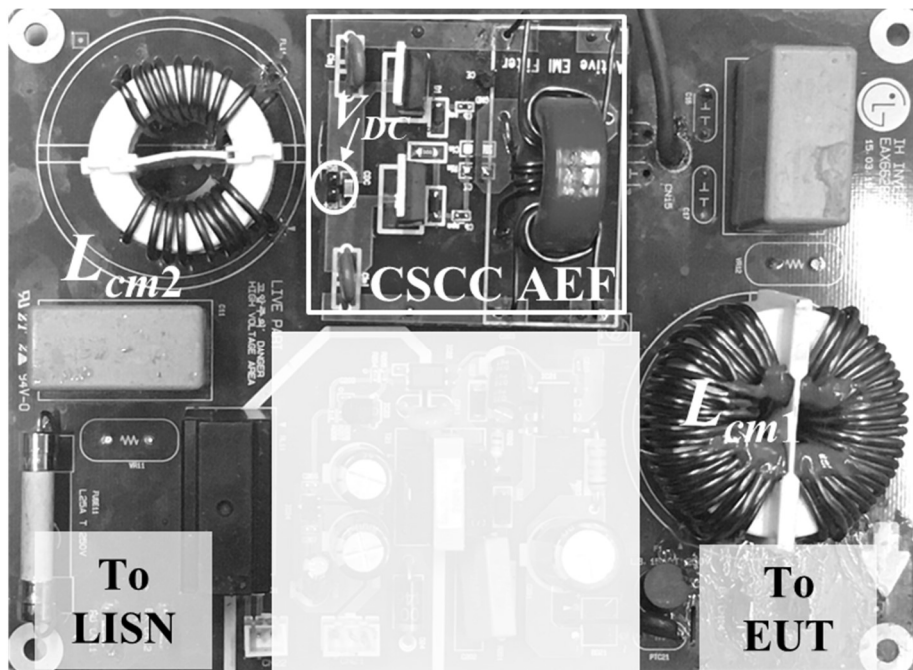


Fig 4-9. The photograph of the total EMI filter with the CSCC AEF

Table 4-1. Components Values of The CSCC Active EMI Filter

Components	Values
$C_Y, C_{inj}, C_b, C_e, C_{DC}, C_L, C_X$	2.2 nF, 1.5 nF, 2.2 $\mu$ F, 2.2 $\mu$ F, 10 $\mu$ F 150nF 2.2uF
$R_{bias}, R_e, R_o, L_{sen}$	15 k $\Omega$ , 2.2 $\Omega$ , 5.1 $\Omega$ , 59 uH
$L_{cm1}, R_{cm1}, C_{cm1}$	8 mH, 80 k $\Omega$ , 10 pF
$L_{cm2}, R_{cm2}, C_{cm2}$	1mH, 4 k $\Omega$ , 16 pF



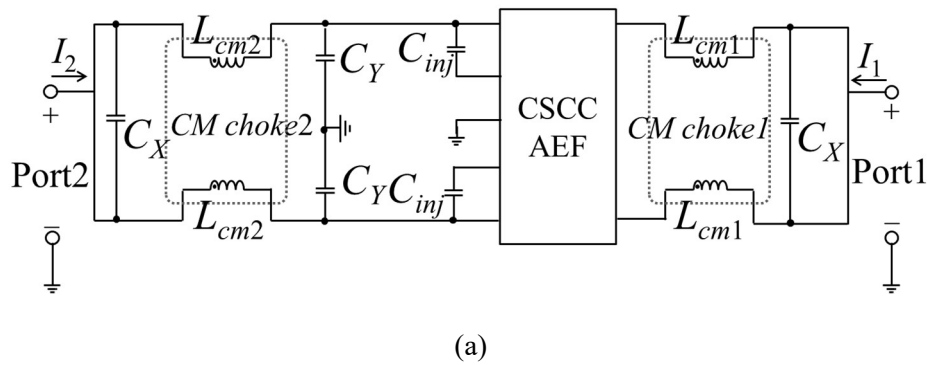
Table 4-2. Specification of the Core for the Sensing Transformer

Components	Values
Effective section area ( $A_c$ )	51.26 mm <sup>2</sup>
Effective length of magnetic path ( $l_e$ )	60 mm
Weight of the core	15.19 g
Saturation magnetic flux ( $B_m$ )	490 mT

#### 4.4.2. Performance Validation by VNA Measurements

For the performance validation of the EMI filter with the AEF, the S-parameters are extracted through the VNA as shown in Fig 4-10(a). The performance of the PEF is also measured for the comparison to the AEF. The PEF, which used for the comparison, consists of two CM choke,  $C_{inj}$  and  $C_Y$  by replacing the AEF part with only  $C_{inj}$  since the impedance of the sensing transformer can be negligible as compared to the other CM choke.

In the VNA measurements, the noise transfer characteristic from the EUT to the noise receiver can be estimated through the  $S_{21}$  parameter when the Port 1 and Port 2 are assigned as the noise source side and receiver side. The  $S_{21}$  parameters of all cases are measured and plotted in Fig 4-10(b). The simulated  $S_{21}$  using SPICE is also plotted to demonstrate the modeling accuracy. As compared to the  $S_{21}$  parameter in the PEF, the  $S_{21}$  is reduced by about 5~20 dB in a frequency range from 100 kHz to 10MHz when the AEF is implemented, as shown in Fig 4-10(b).





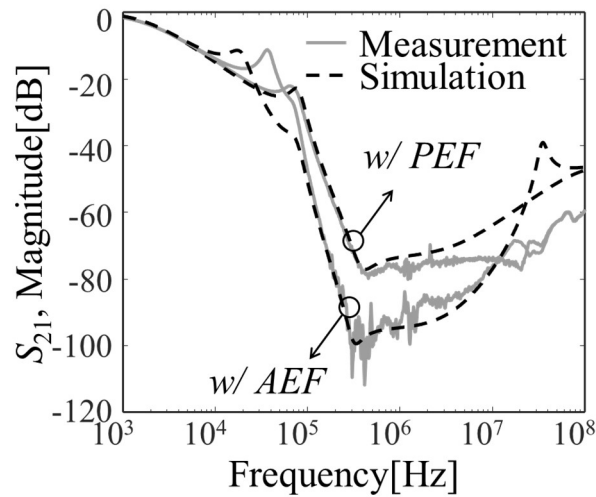


Fig 4-10. (a) Schematic of a VNA measurement to verify the AEF performance of the CM noise reduction (b)  $S_{21}$  parameter with the AEF and with the PEF

#### 4.4.3. CM Conducted Emissions Measurement

The EMI filter with the AEF was implemented in front of the 2.2 kW current resonance inverter in a commercial product. For comparison, the PEF composed of two CM chokes,  $C_{inj}$ , and  $C_Y$  has also been tested in the same setup. The CM-conducted emissions for all cases are measured by using LISN, CM/DM separator, and spectrum analyzer in the frequency range from 150 kHz to 30 MHz, as shown in Fig 4-11(a). The measurement results of all cases are plotted in Fig 4-11(b). As compared to the CM conducted emissions with the PEF, the AEF reduced the CM conducted emissions about 5 to 20 dB in the frequency range from 150 kHz to 10 MHz. This result is highly correlated with the VNA measurements.

It is difficult to reduce the low frequencies CM conducted emissions by the PEF in the compact size since the multistage structure is necessary. By applying the AEF in the real product, the CM noise can be effectively reduced in low-frequency range with the compact size.

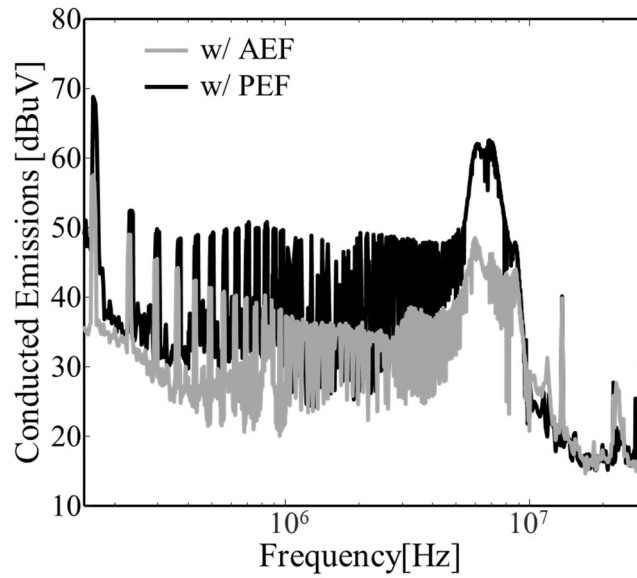
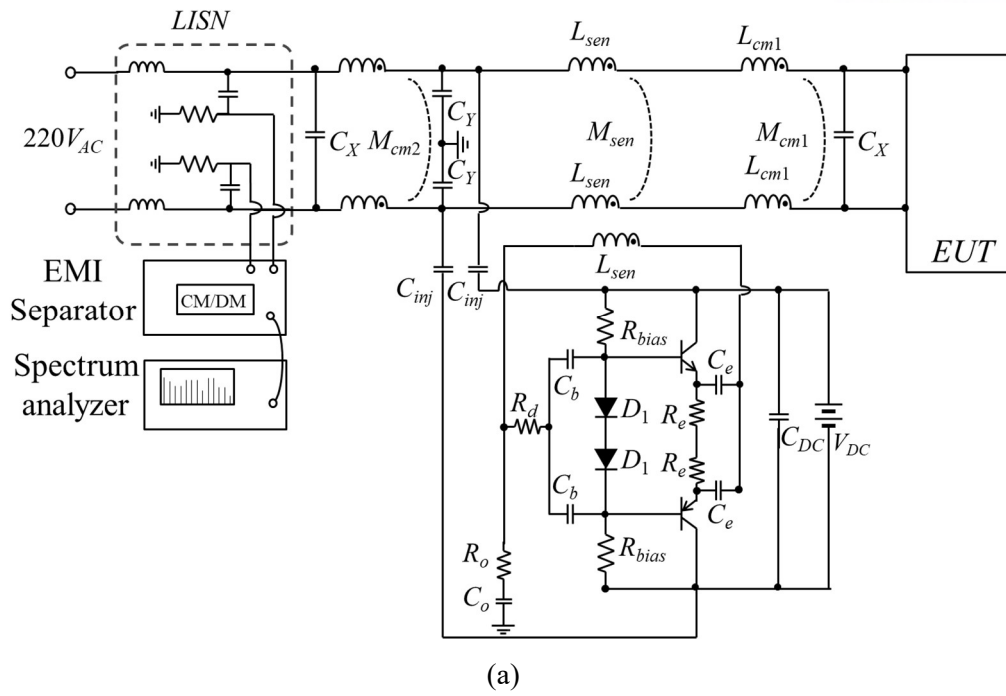


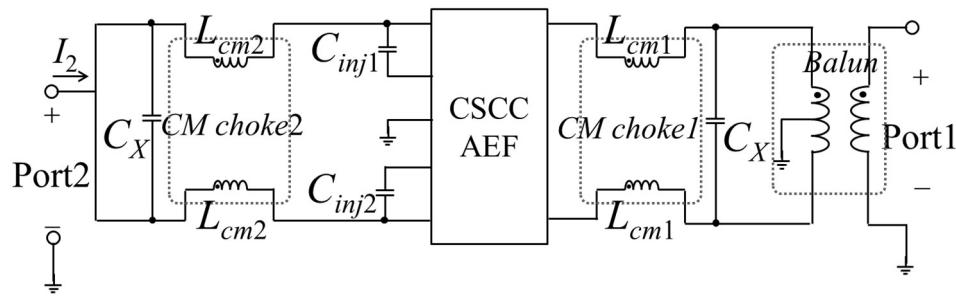
Fig 4-11. (a) The CM conducted emissions measurement setup (b) Measured CM conducted emissions with the AEF and the PEF

#### 4.4.4. The Discussion

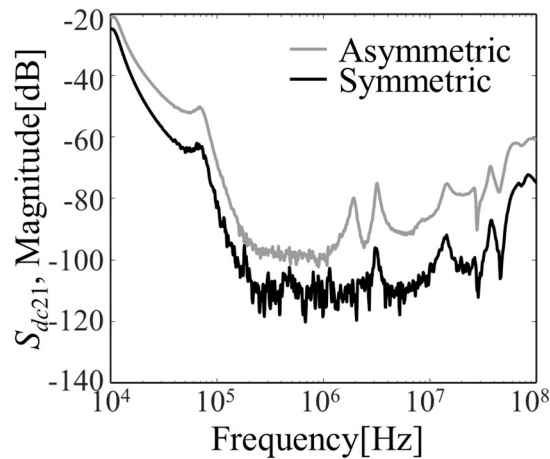
As aforementioned, the CSCC AEF in [40] can be implemented in the power conversion system without the additional dc supply since the rectified ac voltage from the power lines is available for the dc supply of the push-pull amplifier as shown in Fig 4-1(a). However, the AEF in [40] requires the high voltage BJTs due to high dc supply voltage and the transformation from the DM noise to CM noise occurs due to its asymmetric structure [41]. The asymmetric structure is inevitable since the compensation signal only affects the connected power lines. Although the compensation part can be coupled when the CSCC AEF of [40] is implemented in the single-phase power system, the asymmetry of the CSCC AEF can take place due to the impedance mismatching caused by the rectifier circuit. Accordingly, the configuration of the CSCC AEF in [40], which is directly connected to the power lines, is not suitable to employ into the real product.

Herein, the effect of the asymmetric structure is investigated by using the proposed CSCC AEF in this section. For the verification of the transformation from the DM noise to CM noise, mix-mode S-parameters are measured. For the realization of the DM noise, the balun transformer is inserted between the Port 1 and the total EMI filter, whereas, both power lines at opposite side are connected to the Port2 regarding the earth GND as shown in Fig 4-12(a). The balun transformer turns the CM signals generated by the Port1 into the DM signals and couples these with both power lines. On the other hand, the Port2 only measures the signal with reference of the earth GND. Thus, the measured  $S_{21}$  in Fig 4-12(a) represents the  $S_{dc21}$  which is the DM to CM mode conversion parameter from the Port 1 to the Port2.

The compensation capacitors,  $C_{inj1}$  and  $C_{inj2}$ , are same as 1.5 nF in the symmetric CSCC AEF, while  $C_{inj2}$  is disconnected from the power line and  $C_{inj1}$  is set as 3.3nF in the asymmetric CSCC AEF. The values of other circuit parameters uses the values in Table 4-1. The  $S_{dc21}$  of the asymmetric CSCC AEF is higher about 5 dB to than 20 dB than the symmetric CSCC AEF. It means that the unbalanced impedance due to the AEF operation can result in the increase of CM noise by the mode conversion from DM noise in the real products. Therefore, although the additional dc supply is necessary, the compensation part of the CSCC AEF should be designed as the symmetric configuration by using the capacitive coupling at the compensation part.



(a)



(b)

Fig 4-12. (a) Schematic of a VNA measurement to verify the transformation from DM noise to CM noise due to the unbalance structure of the AEF (b)  $S_{dc21}$  parameter with the asymmetric ( $C_{inj1}=3.3\text{nF}$ ) and symmetric ( $C_{inj1}=C_{inj2}=1.5\text{nF}$ ) AEF

## 4.5. Summary

The feed-forward current-sense current-compensation (CSCC) AEF has been proposed to effectively reduce the CM noise in the power conversion system. The CSCC AEF has been completely analyzed and the operation has been explained through the feedback theory. Practical design guidelines were developed from the analysis with considerations for both performance and stability. The design flow of the AEF was also introduced by using the extracted design rules. The total EMI filter with the CSCC AEF was designed according to the design flow and employed into a compact size PCB. The performance of the filter with the AEF was verified with VNA measurements. The AEF was applied to a real product with the 2.2 kW current resonance inverter, and the CM

conducted emissions were effectively attenuated by about 5 - 20 dB from 150 kHz to 10 MHz. Furthermore, the effect of the asymmetric structure due to the AEF has been investigated and presented.

## Chapter V. Conclusion

### 5.1. Performance Comparison Among the AEFs

The performances and characteristics of the AEFs in the thesis are compared with those of the previous AEFs, as summarized in Table 5-1. For the max attenuation of the AEF in the conducted emissions measurement,  $ATT_{max}$  is defined as

$$ATT_{max} = \max \left( \frac{CE_{w/oAEF}(f)}{CE_{w/ AEF}(f)} \right)$$

The  $ATT_{max}$  of each AEF is shown in Table 5-1, based on the presented value in each reference. Although the low-frequency boundary of the attenuation in the proposed AEFs is quite higher than those in the AEFs in [15] and [19], the proposed AEFs provide higher attenuation in the frequency range from 150 kHz to 10 MHz in the conducted emissions regulation range. The low-cost OP amp can be utilized for the proposed AEF in Chapter II because the maximum performance of the AEF can be achieved when the injection gain is “1”. Although the CSCC AEF of [15] has shown the highest  $ATT_{max}$ , the high-performance OP amp is necessary to obtain the high noise attenuation because the noise attenuation by CSCC AEF of [15] depends on the OP amp gain. Accordingly, the proposed VSCC AEF can be manufactured at a lower cost as compared with the AEF in [15] because the low-performance OP amp can be available for the proposed method. In addition, the AEFs in Chapter III and IV can be realized by using the low-cost and low-voltage BJTs. Therefore, the effective noise reduction can be obtained in the low-cost by using the proposed AEFs.

The size of proposed AEFs is also compared with the previous AEF based on the effective length of the core used for the sensing or compensation transformer because the transformer takes a large portion on the total size and weight of the AEFs. The VSVC AEF and CSCC AEF, which are presented in Chapter II and Chapter IV, can be realized by using the smaller size of the transformer as compared with other AEFs using the transformer, as shown in Table 5-1. In the transformerless configuration, the proposed AEF using the push-pull amplifier can be manufactured in a much more compact size, as compared with the AEF in [17], because the number of the components in the proposed AEF is much smaller than in the AEF in [17]. The size of the total EMI filter, thus, can be greatly reduced by using the proposed methods.

Although the separate DC supply for the proposed AEFs is necessary, proper DC voltage is usually available from a control board in real application products. In addition, the proper isolation between

the power lines and dc supply can be achieved to reduce the coupling noise at the AEF supply.

Table 5-1 Comparison of Performances and Characteristics Among AEFs

	Sensing - Injection type	Type of Amp.	BW [MHz]	$ATT_{max}$ [dB]	Target EUT [kW]	Dominant Factor of AEF Size	Core effective length [mm]	Benefits	Drawbacks
[13]	Inductive Inductive	OP	0.150~2	10	0.24	Transformer	30.1 55.8	Higher DOF in amp design	Bulky and expensive transformer Additional DC supply
[15]	Inductive Capacitive	OP	0.010 ~ 6	30	1	Transformer	94	$ATT$ in low frequency range Higher DOF in amp design	Bulky and expensive transformer Additional DC supply
[17]	Capacitive Capacitive	OP	0.15~0.5	10	6.8	Active components	No Core	Higher DOF in amp design	Leakage current Additional DC supply # of active components
[19]	Capacitive Inductive	Push-pull	0.010~3	20	3.7	Active components	144	$ATT$ in low frequency range Standalone	Bulky and expensive transformer High voltage BJT
[20]	Capacitive Inductive	Push-pull	0.150 ~ 1.5	-	0.75	Transformer,	331	Standalone	Bulky and expensive transformer High voltage BJT
[23]	Inductive Capacitive	Push-pull Amp.	0.150 ~ 10	20	3.7	Transformer, Active components dependent	-	Low voltage BJT	Bulky and expensive transformer Additional DC supply
Chapter II	Capacitive Inductive	Op	0.150~10	12	0.2	Active components	44	Low leakage current Higher DOF in amp design	Bulky and expensive transformer Additional DC supply
Chapter III	Capacitive Capacitive	Push-pull Amp.	0.150~6	25	2.2	Active components	No core	Low voltage BJT Compact and light	Leakage current Additional DC supply
Chapter IV	Inductive Capacitive	Push-pull Amp.	0.150~10	20	2.2	Active components	60	Low voltage BJT Compact size	Bulky and expensive transformer Additional DC supply

## 5.2. Conclusion

Three types of active EMI filters (AEFs) – 1) voltage-sense voltage-compensation; 2) voltage-sense current compensation; 3) current-sense current compensation – have been proposed in this thesis to achieve the high noise attenuation of the CM-conducted emissions at the low-frequency range.

In Chapter 2, the feed-forward VSVC AEF, which is composed of the sensing capacitors, the injection transformer, and the OP amp, has been introduced. The loop gain of the EMI filter with the VSVC AEF can be extracted based on the feedback theory. The effects of the VSVC AEF are demonstrated through the power line impedance boosting and feedback theory and verified by the VNA measurements. The VSVC AEF was implemented in the 200W power conversion system composed of the PFC, LLC converter, and flyback DC-DC converter. In the CM-conducted emissions

measurement, the VSVC AEF attenuates about 10~12 dB and reduces the size of the total EMI filter by 50% as compared with the three-stage CM chokes. The degradation of the VSVC AEF due to the magnetic saturation of the injection transformer was also verified from the experiments.

The transformerless AEF using the push-pull amplifier has been presented in Chapter 3. The sensing and compensation parts of the VSCC AEF are realized as the capacitive coupling for the high-current power system. Accordingly, the VSCC AEF can be free from the degeneration due to the magnetic saturation. The system characteristic was analyzed using the loop gain of the EMI filter, including the VSCC AEF, extracted from the block diagram of the total system. The quantified design guidelines regarding the performance and system reliability are developed based on the rigorous analysis. The circuit analysis and performance are validated by the VNA measurement. In the CM-conducted emissions measurement, the VSCC AEF shows the 5~15 dB noise attenuation from 150 kHz to 6 MHz. Also, the surge-protection circuits in the VSCC AEF are demonstrated on the 2kW lightning-surge test.

The CSCC AEF with the symmetric structure has been proposed in Chapter 4. The proposed CSCC AEF consists of the sensing transformer, injection capacitors, and push-pull amplifier. The symmetric configuration of the CSCC AEF has been realized by the capacitive coupling between the AFE and all of the power lines. Besides, the transformer designed by a small number of turns is used to avoid the magnetic saturation as the sensing transformer. Based on the circuit analysis, the operation of the CSCC AEF was investigated, and the loop gain of the total EMI filter including the CSCC AEF was calculated. The practical design guidelines of the CSCC AEF are developed from the circuit analysis. The performances of the CSCC AEF were validated in the VNA measurements. In the CM-conducted emissions measurements, the CSCCAEF shows the 5~20 dB CM noise attenuation from 150 kHz to 10 MHz. Furthermore, the effects of the asymmetrical structure due to the CSCC AEF on the CM noise are investigated through the VNA measurements.



## REFERENCES

- [1] C. Paul, *Introduction to Electromagnetic Compatibility*, 2nd ed, John Wiley & Sons, 2006.
- [2] IEC 60990:1999 ed. 2.0; “International standard –Methods of measurement of touch current and protective conductor current”, 1999
- [3] O. M. Timothy, P. L. Richard, *EMI filter Design*, 3rd ed, CRC Press, 2011.
- [4] H. Chen, Z. Qian, S. Yang and C. Wolf, "Finite-element modeling of saturation effect excited by differential-mode current in a common-mode choke," *IEEE Trans on. Power Electron.*, vol.24, no.3, pp.873-877, March 2009
- [5] M.J.Nave, "On modeling the common mode inductor," in *Proc IEEE Int. Symp. Electromagn. Compat.*, Aug. 1991, pp.452-457
- [6] K. Mainali, R. Oruganti., "Conducted EMI mitigation techniques for switch-mode power converters: a survey," *IEEE Trans.Power Electron.*, vol.25, no.9, pp.2344-2356, Sept. 2010
- [7] W. Xin, N.K. Poon, C. M. Lee, M.H. Pong, and Z. Qian, "A study of common mode noise in switching power supply from a current balancing viewpoint," in *Proc. IEEE Int. Conf. Power Electron. Drive Syst., 1999*, pp.621-625
- [8] D. Cochrane, D.Y. Chen, and D. Boroyevic, "Passive cancellation of common-mode noise in power electronic circuits," *IEEE Trans. Power Electron.*, vol.18, no.3, pp.756-763, May 2003
- [9] L. LaWhite and M. F. Schlecht, “Active filters for 1-MHz power circuits with strict input/output ripple requirements,” *IEEE Trans. Power Electron.*, vol. PE-2, no. 4, pp. 282–290, Oct. 1987..
- [10] L. LaWhite and M. F. Schlecht, “Design of active ripple filters for power circuits operating in the 1–10 MHz range,” *IEEE Trans. Power Electron.*, vol. 3, no. 3, pp. 310–317, Jul. 1988.
- [11] N.K. Poon, J. C. P. Liu, C. K. Tse, and M. H. Pong, "Techniques for input ripple current cancellation: classification and implementation," *IEEE Trans. Power Electron.*, vol.15, no.6, pp.1144-1152, Nov 2000
- [12] Y. Son, S. Sul, "Generalization of active filters for EMI reduction and harmonics compensation," *IEEE Trans. Ind. Appl.*, vol.42, no.2, pp.545-551, March./April 2006
- [13] K. Mainali and R. Oruganti, “Design of a current-sense voltage-feedback common mode EMI filter for an off-line power converter,” in *Proc. IEEE Power Electron. Spec. Conf.*, 2008, pp. 1632–1638.

- [14] W. Chen, W. Zhang, X. Yang, Z. Sheng, and Z. Wang, "An experimental Study of Common- and Differential-Mode Active EMI Filter Compensation Characteristics," *IEEE Trans. Electromagn. Compat.*, vol.51, no.3, pp.683-691, Aug. 2009
- [15] W. J. Chen, X. Yang, and Z. Wang, "A novel hybrid common-mode EMI filter with active impedance multiplication," *IEEE Trans. Ind. Electron.*, vol.58, no.5, pp.1826-1834, May 2011
- [16] D. Shin, S. Kim, G. Jeong, et al. "Analysis and design guide of active EMI filter in a compact package for reduction of common-mode conducted emissions," *IEEE Trans. Electromagn. Compat.*, vol. 57, no. 4, pp. 6670-671, Aug. 2015.
- [17] M.L. Heldwein, H. Ertl; J. Biela, J.W Kolar, "Implementation of a transformerless common-mode active filter for offline converter systems," *IEEE Trans. Ind. Electron.*, vol.57, no.5, pp.1772-1786, May 2010
- [18] Y. Chu, S. Wang, and Q. Wang, "Modeling and stability analysis of active/hybrid common-mode EMI filters for DC/DC power converters," *IEEE Trans. Power Electron.*, vol. 31, no. 9, pp. 6254–6263, Sep. 2016.
- [19] S. Ogasawara, H. Ayano, and H. Akagi, "An active circuit for cancellation of common-mode voltage generated by a PWM inverter," *IEEE Trans. Power Electron.*, vol. 13, no. 5, pp. 835–841, Sep. 1998.
- [20] M. C. Di Piazza, G. Tinè, and G. Vitale, "An improved active common-mode voltage compensation device for induction motor drives," *IEEE Trans. Ind. Electron.*, vol. 55, no. 4, pp. 1823–1834, Apr. 2008.
- [21] M. C. Di Piazza, A. Ragusa, and G. Vitale, "Design of grid-side electromagnetic interference filters in AC motor drives with motor-side common mode active compensation," *IEEE Trans. Electromagn. Compat.*, vol. 51, pt. 2, no. 3, pp. 673–682, Aug. 2009.
- [22] M. C. Di Piazza, A. Ragusa, and G. Vitale, "Effects of common mode active filtering in induction motor drives for electric vehicles," *IEEE Trans. Veh. Technol.*, vol. 59, no. 6, pp. 2664–2673, Sep. 2010.
- [23] Y. Son, S. Sul, "A new active common-mode EMI filter for PWM inverter," *IEEE Trans. Power Electron.*, vol.18, no.6, pp.1309-1314, Nov. 2003
- [24] K. Euerle, K. Iyer, E. Severson, R. Baranwal, S. Tewari and N. Mohan, "A compact active filter to eliminate common-mode voltage in a SiC-based motor drive," *2016 IEEE Energy Conversion Congress and Exposition (ECCE)*, 2016, pp. 1-8.

- [25] A. Esmaeli, Y. Sun, and L. Sun, "Mitigation of the adverse effects of pwm inverter through active filter technique," in *Proc. 1st Int. Symp. Syst.Control Aerospace Astronautics*, Jan. 2006, pp. 5–774.
- [26] P. Pairodamonchai, S. Suwankawin, and S. Sangwongwanich, "Design and implementation of a hybrid output EMI filter for high-frequency common-mode voltage compensation in PWM inverters," *IEEE Trans. Ind. Appl.*, vol. 45, no. 5, pp. 1647–1651, Sep./Oct. 2009.
- [27] K. Gulez, A. A. Adam, and H. Pastaci, "Torque ripple and EMI noise minimization in PMSM using active filter topology and field-oriented control," *IEEE Trans. Ind. Electron.*, vol. 55, no. 1, pp. 251–257, Jan. 2008.
- [28] D. Hamza, M. Pahlevaninezhad, and P. Jain, "Implementation of a novel digital active EMI technique in a DSP-based DC–DC digital controller used in electric vehicle (EV)," *IEEE Trans. Power Electron.*, vol. 28, no. 7, pp. 3126–3137, Jul. 2013.
- [29] D. Shin, S. Kim, G. Jeong, J. Park, J. Park, K. J. Han, and J. Kim, "A common-Mode Active Filter in a Compact Package for a Switching Mode Power Supply", in *Proc IEEE Int Symp Electromagn. Compat.* Aug 2014.
- [30] D. Shin, C. Son, S. Jeon, B. Cho, J. Han, and J. Kim, "A simple low-cost common mode active EMI filter using a push-pull amplifier" in *2016 IEEE Energy Conversion Congress and Exposition (ECCE)*, Milwaukee, 2016, pp. 1-5.
- [31] D. Shin, S. Jeong and J. Kim, "Quantified Design Guidelines of Compact Transformerless Active EMI Filter for Performance, Stability, and High Voltage Immunity," *IEEE Trans. Power Electron.*, vol. PP, no. 99, pp. 1-1.
- [32] A. P. Duffy, A. J. M. Martin, A. Orlandi, G. Antonini, T. M. Benson, and M. S. Woolfson, "Feature selective validation (FSV) for validation of computational electromagnetics (CEM)—Part I: The FSV method," *IEEE Trans. Electromagn. Compatibil.*, vol. 48, no. 3, pp. 404–415, Aug. 2006.
- [33] *Standard for Validation of Computational Electromagnetics Computer Modeling and Simulations*, IEEE Standard P1597, Aug. 2008.
- [34] D. A. Neamen, *Microelectronics circuit analysis and design*, 3rd ed, McGraw Hill, 2007.
- [35] J. Jeong, S. Kim and C. Kim and J. Kim,, "Estimation of the worst-case conducted emission noise due to multiple parallel power converters," in *Proc. 2016 URSI Asia-Pacific Radio Science Conference (URSI AP-RASC)*, Seoul, 2016, pp. 931-934.

- [36] J. Meng, W. Ma, Q. Pan, Z. Zhao, and L. Zhang, "Noise source lumped circuit modeling and identification for power converters," *IEEE Trans. Ind. Electron.*, vol. 53, no. 6, pp. 1853–1861, Dec. 2006.
- [37] V. Tarateeraseth, H. Bo, K. Y. See, and F. Canavero, "Accurate extraction of noise source impedance of SMPS under operating condition," *IEEE Trans. Power Electron.*, vol. 25, no. 1, pp. 111–117, Jan. 2010.
- [38] F. Luo, D. Dong, D. Boroyevich, P. Mattavelli, and S. Wang, "Improving high-frequency performance of an input common mode EMI filter using an impedance-mismatching filter," *IEEE Trans. Power Electron.*, vol. 29, no. 10, pp. 5111–5115, Oct. 2014.
- [39] IEC 61000-4-5 ed.3.0; "International standard – Electromagnetic compatibility (EMC)–Part 4-5: Testing and measurement techniques – Surge immunity test", 2014
- [40] 사토신지, 능동필터장치 및 전력변환장치. 특허출원 제 10-2010-0026696, 2010
- [41] S. Wang and F. C. Lee, "Investigation of the Transformation Between Differential-Mode and Common-Mode Noises in an EMI Filter Due to Unbalance," *IEEE Tran. Electromagn. Compat.*, vol. 52, no. 3, pp. 578-587, Aug. 2010.

## APPENDIX. A.

# Quantified Design Guides for Reduction of Radiated Emissions in Package-Level Power Distribution Networks

### A.1. Introduction

Simultaneous switching currents are generated by the switching operation of the numerous logic circuits and buffers inside integrated circuits (ICs). The switching currents can be the source of the electromagnetic interference (EMI) problem such as the radiated emissions and the noise coupling due to power and GND voltage fluctuations [A.1]–[A.4]. By placing decoupling capacitors between the power and GND nets, the impedance of a power distribution network (PDN) can be limited at low values in the target frequency range [A-4]. The EMI due to the switching current is suppressed by the low impedance PDN. The radiated emissions also are directly affected by the placement of the decoupling capacitors and the geometry of the PDN in packages and printed circuit boards (PCBs). The switching current distributions on the PDN geometry are the sources of radiated emissions.

The radiated emissions can be computed by various full-wave numerical methods such as the finite element method (FEM), the finite-difference time-domain (FDTD) method, and the method of moments (MoM). The partial element equivalent circuit (PEEC) method based on the electric field integral equation (EFIE) also can be used to compute the radiated emission [A-5]–[A-8]. In the PEEC method, structures are discretized into many conductor or dielectric mesh cells and modeled as equivalent circuits. The voltages and currents at every mesh cell are obtained as the solutions of the PEEC model. The radiated emissions can then be computed by considering every current segment on the structures as a Hertzian dipole. The PEEC method is suitable for the analysis of the EMI factors in the PDN because the effects of individual current paths on the radiated emissions easily can be identified. Any lumped-circuit components also are easily incorporated into the PEEC models. Although the PEEC method has advantages in analysis of the EMI factors, the numerical calculation procedures are too complicated to be applied in the initial design stage for a PDN.

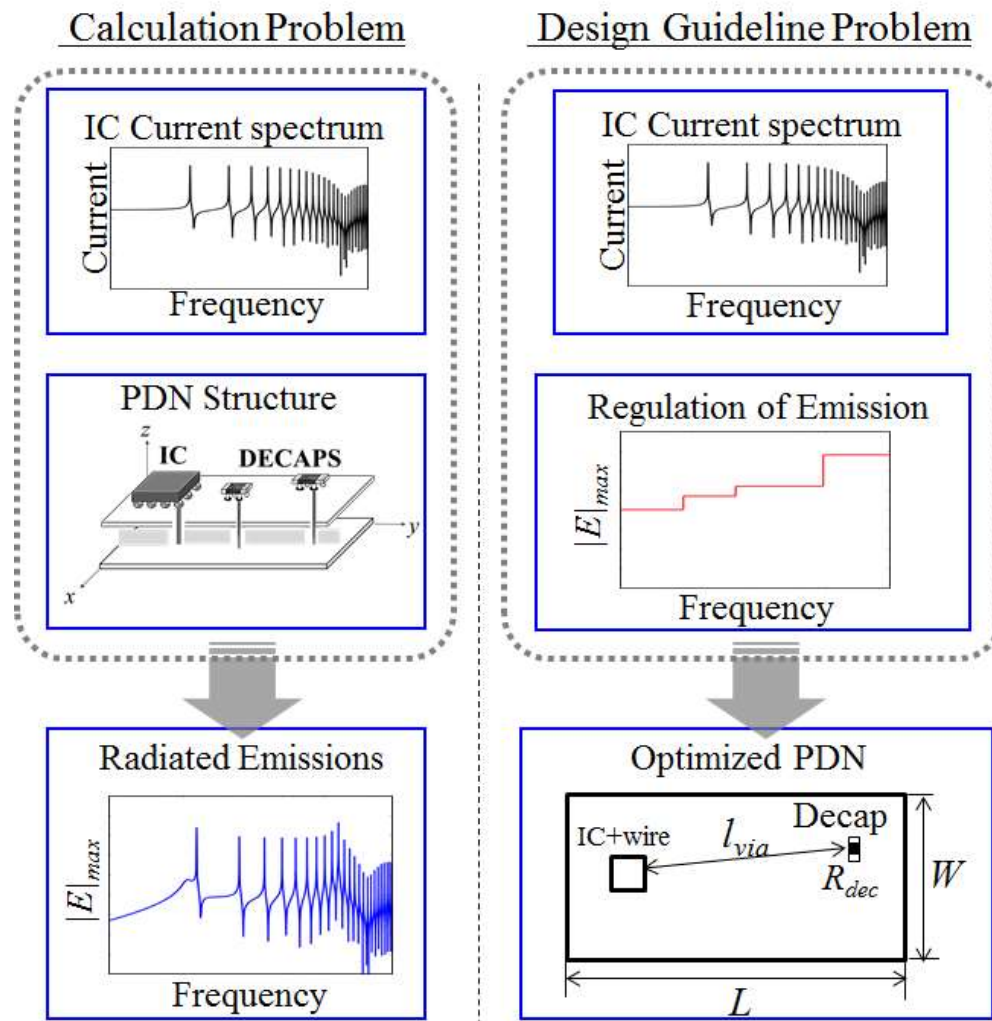


Fig A-1. Development of PDN design guidelines as the reverse of radiated emission analysis

Analytical closed-form expressions of the radiated emissions due to power and GND planes have been proposed using the equivalent magnetic currents in [A-9]–[A-11]. The tangential electric field at the edges of the planes is calculated based on the cavity model [A-12], [A-13]. The equivalent magnetic currents at the edges are derived, and the radiated emissions are calculated from the magnetic currents. In [A-10], the effects of the decoupling capacitors mounted on the PCB also are considered in closed-form expressions with the assumption that the decoupling capacitors are uniformly distributed. The analytical expressions are useful in estimating the far-field radiated emissions of the designed PDN structure. In the initial design stage of a PDN, however, even a simpler expression and analysis method are still desired.

The radiated emissions from the small power and GND planes in packaging structures can be

calculated in a simpler method, if the cavity mode resonances would occur at the high frequency range above the regulations for radiated emissions. The radiated emissions due to the small power and GND planes have been calculated using the equivalent lumped-circuit model in [A-14] and [A-15]. In the lumped-circuit model, the parallel planes are modeled as the via self-inductances, mutual inductances, and a plane capacitance based on the cavity resonance model [A-16]. The on-chip capacitance, on-chip resistance, the inductances at bonding wires, and the surface-mount technology (SMT) decoupling capacitors are easily included in the PDN circuit model. The conduction currents at the vertical vias and the polarization currents in the dielectric medium are obtained from the circuit model. The radiated emissions are then computed by treating the via currents and polarization currents as the sources of the far-zone electromagnetic fields [A-15]. The calculation using the equivalent lumped-circuit model is faster and simpler than for other numerical or analytical models. Several effects of the PDN geometry on the radiated emissions also have been investigated in [A-15]; however, the quantified analysis and design guides of a PDN have not been presented.

Establishing PDN design guides for radiated emissions is the reverse problem of the emission calculation. As depicted in Fig A-1, the radiated emission can be computed from the PDN model and the IC switching current. Conversely, the PDN design guides could be obtained from a knowledge of the IC switching current and the regulation of radiated emissions. To solve the reverse problem and develop the design guides, however, an even simpler closed-form expression for the PDN radiated emission is necessary.

In this chapter, simple closed-form expressions for the radiated emission due to a package-level PDN are developed based on the equivalent lumped-circuit model. The closed-form expressions are validated with the numerical calculations and far-field measurements. The closed-form expression allows an effective analysis of the EMI factors in the PDN structure. The effects of the PDN design parameters on the radiated emissions are calculated by sensitivity analysis. In addition, a systematic procedure for developing quantified PDN design guidelines to suppress the radiated emission is proposed using the closed-form expression. The regulation of the radiated emissions is normalized by the spectrum of switching currents in extracting the PDN design procedure. An example of the PDN design satisfying the EMI regulations also is demonstrated.

## A.2. Closed-Form Expressions of Radiated Emissions for the Package-Level PDN

The equivalent circuit model for the PDN with a small pair of rectangular planes is briefly



introduced in this section. In the example herein, two decoupling capacitors and an IC are mounted on the top side of the board. The GND (VSS) terminals are directly connected to the upper metal plane, and the power (VDD) terminals are connected to the bottom plane through vias. The via self-inductance, mutual inductance, and plane capacitance are extracted from the cavity resonance model. Parasitic circuit elements of the bonding wire and IC are included in the equivalent lumped-circuit model of the PDN. The currents and voltages are calculated from the circuit model. The closed-form expression for the far-zone radiated emissions is derived using the extracted currents with reasonable assumptions. The closed-form expression is validated by comparison with the numerical results from an in-house PEEC tool and a commercial FEM solver, HFSS. The PEEC model of [A-5] is implemented in the in-house PEEC tool. The measurements of radiated emissions are also performed to verify the closed-form expression.

### A.2.1. Equivalent lumped-circuit model for the package-level PDN

An example of the package-level PDN is shown in Fig A-2 (a). An IC die is connected to the power and GND planes through vias and bonding wires. Two decoupling capacitors (Decap1 and Decap2) are also connected to the planes. The switching currents generated by the IC switching behavior are flowing through the vertical via between the top and bottom planes. When the ports are defined across the antipads of the vias, the transfer impedance  $Z_{ij}$  between “Via  $i$ ” and “Via  $j$ ” is expressed as a parallel-plate capacitance  $C_p$  and inductances  $L_{ij}(\omega)$  as [A-12], [A-13], and [A-16]

$$Z_{ij} = \frac{1}{j\omega C_p} + j\omega L_{ij}(\omega), \quad (\text{A.1})$$

where

$$L_{ij}(\omega) = \frac{\mu d}{ab} \sum_{m=0} \sum_{n=0} \frac{\varepsilon_m^2 \varepsilon_n^2}{k_{mn}^2 - k^2} f(x_i, y_i, x_j, y_j) \Big|_{(m,n) \neq (0,0)} \quad (\text{A.2})$$

$$f(x_i, y_i, x_j, y_j) = \cos\left(\frac{m\pi x_i}{a}\right) \text{sinc}\left(\frac{m\pi x_i}{2a}\right) \cos\left(\frac{n\pi y_i}{b}\right) \text{sinc}\left(\frac{n\pi y_i}{2b}\right)$$

$$\times \cos\left(\frac{m\pi x_j}{a}\right) \text{sinc}\left(\frac{m\pi x_j}{2a}\right) \cos\left(\frac{n\pi y_j}{b}\right) \text{sinc}\left(\frac{n\pi y_j}{2b}\right)$$

The  $a$ ,  $b$ , and  $d$  correspond to the plane width, length, and the distance between the two planes, respectively. The  $i$ th and  $j$ th rectangular ports are placed at  $(x_i, y_i)$  and  $(x_j, y_j)$ .  $(t_{xi}, t_{yi})$  and  $(t_{xj}, t_{yj})$



represent the widths of the  $i$ th and  $j$ th ports, respectively.  $k_{mn}^2 = (m\pi/a)^2 + (n\pi/b)^2$  with mode number  $m, n$ ,  $k = \omega\sqrt{\mu\varepsilon}$ , the constant  $\varepsilon_{m,n} = 1$  if  $m, n = 0$ ,  $\varepsilon_{m,n} = \sqrt{2}$ , if  $m, n \neq 0$ , and  $f(x_i, y_i, x_j, y_j)$  represents the wave function for open circuit boundary condition at the parallel-plane boundaries.

The parallel-plate capacitance  $C_p$  can be decomposed into a part due to free charge,  $C_{air}$ , and the other part due to the dielectric bound charge,  $C_{excess}$ , as [A-5]

$$C_p = C_{air} + C_{excess} \quad (A.3)$$

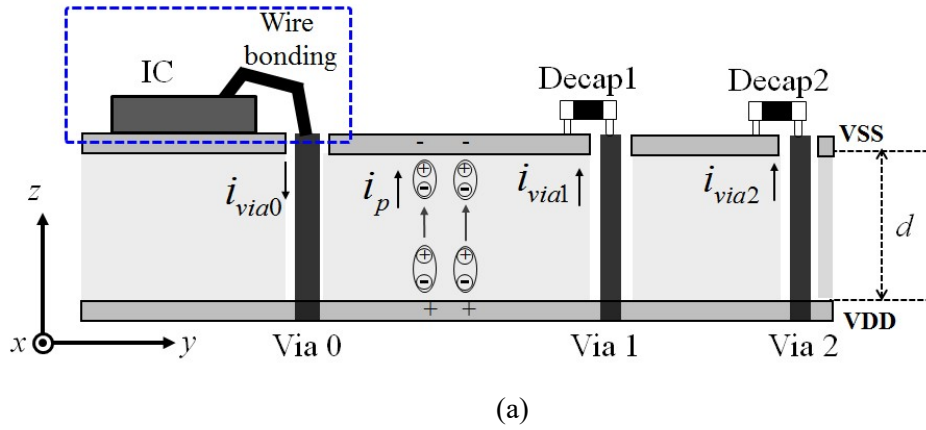
where

$$C_{air} = \varepsilon_0 \frac{ab}{d} \quad (A.4)$$

$$C_{excess} = \varepsilon_0 (\varepsilon_r - 1) \frac{ab}{d}. \quad (A.5)$$

The current flowing through  $C_{excess}$  corresponds to the dielectric polarization current. As will be discussed in Section A.2.2, the polarization current contributes to the far-zone radiated emissions.

In addition, the  $L_{ij}(\omega)$  is nearly constant at the frequencies below approximately 60% of the first cavity resonance frequency; in the low frequency range, it can be approximated to a single value at DC,  $L_{ij}$ , when  $k$  is equal to zero [A-16]. The DC inductance values are used in the lumped-circuit model for the small parallel planes in packages, assuming the cavity mode resonances occur at the frequencies higher than the frequency range interested for radiated emissions.



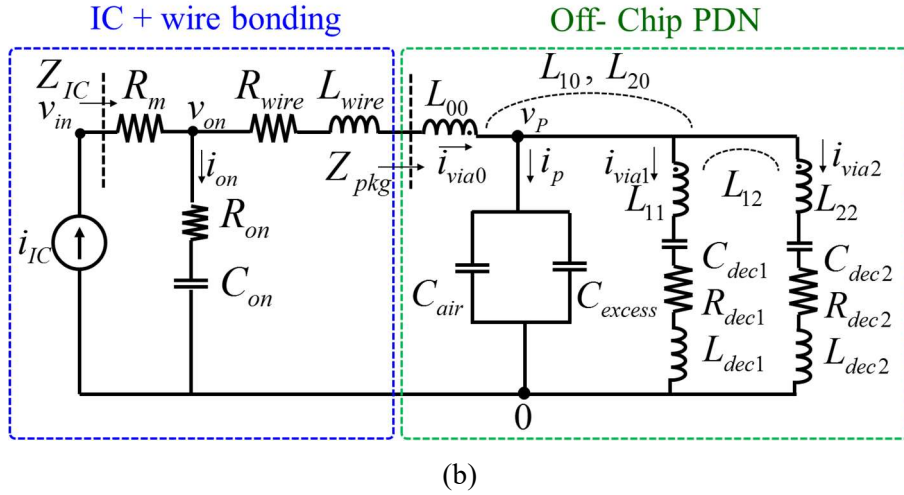


Fig A-2. Example of package-level PDN (a) Cross-section view (b) Equivalent lumped-circuit model

As a result, the PDN structure in Fig A-2(a) can be modeled with the equivalent lumped-circuit model, as shown in Fig A-2(b). The  $L_{00}$ ,  $L_{11}$ ,  $L_{22}$ ,  $L_{10}$ ,  $L_{20}$ , and  $L_{12}$  represent the self- and mutual-inductances for Via 0, Via 1, and Via 2. The SMT decoupling capacitors are modeled as the capacitances,  $C_{dec1}$ ,  $C_{dec2}$ , with the equivalent series resistances (ESR),  $R_{dec1}$ ,  $R_{dec2}$ , and the equivalent series inductances (ESL),  $L_{dec1}$ ,  $L_{dec2}$ . The  $R_{wire}$  and  $L_{wire}$  correspond to the parasitic inductance and resistance of bonding wires. The on-chip decoupling capacitor is modeled as the capacitance,  $C_{on}$ , with the parasitic resistance  $R_{on}$ . The parasitic resistance of the on-chip metal lines also is included as  $R_m$ . The  $Z_{IC}$  and  $Z_{pkg}$  are designated as the PDN impedance looking at the IC current source and the off-chip PDN impedance looking into the Via0, respectively. The  $v_{in}$ ,  $v_{on}$ , and  $v_p$  represent the voltages at each node with reference to the GND zero potential. The  $i_{IC}$ ,  $i_{on}$ ,  $i_{via0}$ ,  $i_{via1}$ ,  $i_{via2}$ , and  $i_p$  correspond to each branch current.

Every node voltage and branch current can be obtained by SPICE simulations or calculations using the circuit model. In this work, every branch current is analytically calculated by building the modified nodal analysis (MNA) equations as [A-18]

$$\begin{bmatrix} \bar{\mathbf{0}} & -\bar{\mathbf{V}}_m^T \\ \bar{\mathbf{V}}_m & \bar{\mathbf{Z}} \end{bmatrix} \begin{bmatrix} \bar{\mathbf{V}} \\ \bar{\mathbf{I}} \end{bmatrix} = \begin{bmatrix} \bar{\mathbf{I}}_s \\ \bar{\mathbf{0}} \end{bmatrix}, \quad (\text{A.6})$$

where the  $\bar{\mathbf{V}}_m$ ,  $\bar{\mathbf{0}}$ , and  $\bar{\mathbf{Z}}$  represent the connectivity matrix, the zero matrix, and the impedance matrix, respectively. The  $\bar{\mathbf{V}}_m$  is associated with the KVL between the node voltages. One node of the branch is defined as the start node, and the other is the end node. The start node and the end node are

assigned by ‘1’ and ‘-1’, else ‘0’ in the  $\overline{\overline{V}}_m$ . All of the circuit parameters are included in the  $\overline{\overline{Z}}$  with the corresponding branch currents. The  $\overline{I}$  and  $\overline{V}$  represent the unknown branch current vector and the node voltage vector, respectively. The source vector  $\overline{I}_s$  includes the IC switching current  $iIC$ . The analytical solutions of the branch currents are utilized to calculate the radiated emission in the next section.

### A.2.2. Closed-form expressions for radiated emissions

ICs themselves are not a typically efficient radiator due to their very small size compared with the off-chip structures. The ICs are often the EMI source when they meet antenna such as PCB traces, power/ground planes, or cables [A-19]. In this work, the electromagnetic fields radiated directly from the IC are neglected, and a package-level PDN structure is the only antenna considered.

The electric field  $\overline{E}$  at an arbitrary point outside the source structure can be calculated from the vector magnetic potential  $\overline{A}$  and scalar electric potential  $V$  as

$$\begin{aligned} \overline{E} &= -j\omega\overline{A} - \nabla V \\ &= -\frac{j\omega\mu}{4\pi} \int_{v'} \frac{\overline{J}_c(\overline{r}')e^{-jk_0|\overline{R}-\overline{r}'|}}{|\overline{R}-\overline{r}'|} dv' - \frac{j\omega\mu}{4\pi} \int_{v'} \frac{\overline{J}_D(\overline{r}')e^{-jk_0|\overline{R}-\overline{r}'|}}{|\overline{R}-\overline{r}'|} dv' - \frac{\nabla}{4\pi\epsilon_0} \int_{v'} \frac{q_T(\overline{r}')e^{-jk_0|\overline{R}-\overline{r}'|}}{|\overline{R}-\overline{r}'|} dv', \quad (\text{A.7}) \end{aligned}$$

where the  $\overline{J}_c$  and  $\overline{J}_D$  are the conduction current density and polarization current density, respectively. The  $q_T$  is the total charge density, including free and bound charges. The  $k_0$  represents the wave number in air. The position vectors of the source and observation points are designated as  $\overline{r}'$  and  $\overline{R}$ .

The electric potential term vanishes quickly with increasing the observation distance, and the far-zone electric field is approximated to

$$\overline{E} \approx -j\omega\overline{A} = -\frac{j\omega\mu}{4\pi} \int_{v'} \frac{\overline{J}_c(\overline{r}')e^{-jk_0|\overline{R}-\overline{r}'|}}{|\overline{R}-\overline{r}'|} dv' - \frac{j\omega\mu}{4\pi} \int_{v'} \frac{\overline{J}_D(\overline{r}')e^{-jk_0|\overline{R}-\overline{r}'|}}{|\overline{R}-\overline{r}'|} dv', \quad (\text{A.8})$$

except that the radial component is zero. Therefore, only the conduction and dielectric polarization currents contribute to the far-zone radiated emissions [A-17].

The radiated emissions due to the PDN structure of Fig A-2 are calculated on a large far-zone sphere, as depicted in Fig A-3. The  $\theta$  and  $\phi$  represent the polar and azimuthal angles of the observation point, respectively. The location of the IC is set as the origin. The parallel planes lie on the  $x$ - $y$  plane with the center at  $(x_c, y_c)$ . The  $l_{via1}$  and  $l_{via2}$  represent the distances between the origin and

each via. The  $l_c$  represents the distance from the origin to the center of the planes. The  $\phi_{via1}$ ,  $\phi_{via2}$ , and  $\phi_c$  correspond to the azimuthal angles of the positions for the vias and the center of the planes, respectively.

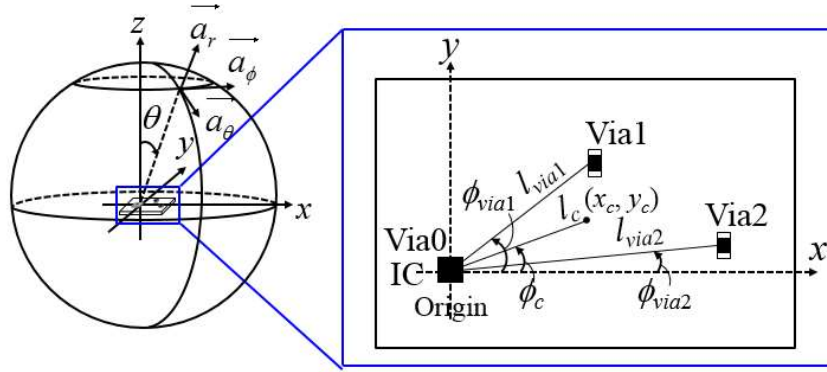


Fig A-3. PDN structure in the spherical coordinates

The horizontal currents flowing along the parallel planes with thin spacing have little effect on the far-zone radiated emissions because the electromagnetic fields caused by the top and bottom plane currents are cancelled by each other [A-15]. Accordingly, only the vertical currents are predominantly responsible and considered as the source of the radiated emissions. The polarization currents in the dielectric medium as well as the via conduction currents behave as the sources of the electromagnetic fields. The amounts of the via and polarization currents can be found from the branch currents in the circuit model of Fig A-2(b). The polarization current is a part of the total plane current, as  $i_p \cdot (\epsilon_r - 1) / \epsilon_r$ .

The far-zone electric fields due to the total PDN structure,  $\bar{E}_{total}$ , are the summation of electric fields caused by the vertical currents as

$$\bar{E}_{total} = \sum_{k=0} \bar{E}_{via,k} + \bar{E}_{polar} \quad (A.9)$$

where

$$\bar{E}_{via,k} = -j \frac{\omega \mu_0 d}{4\pi} i_{via,k} \frac{e^{-jk_0 |\bar{R} - \bar{r}'|}}{|\bar{R} - \bar{r}'|} \sin \theta \cdot \bar{a}_\theta, \quad (A.10)$$

$$\bar{E}_{polar} = -j \frac{\omega \mu_0 d}{4\pi} \int_{-b/2+y_c}^{b/2+y_c} \int_{-a/2+x_c}^{a/2+x_c} \frac{e^{-jk_0 |\bar{R} - \bar{r}'|}}{|\bar{R} - \bar{r}'|} \frac{\epsilon_r - 1}{\epsilon_r} \frac{i_p}{ab} \sin \theta \cdot \bar{a}_\theta dx dy. \quad (A.11)$$

$\bar{E}_{via,k}$  represent the electric fields caused by the  $k$ th via currents. The  $\bar{E}_{polar}$  is the electric fields due to the polarization current distributed uniformly on the planes in the low frequency range below

the cavity mode resonances. The far-zone electric fields have the  $\theta$  components only because the only the currents along the  $z$  axis contribute to the radiated emissions.

The far-zone radiated emissions are calculated as the maximum electric field intensity at the far-sphere. Applying the parallel-ray approximation for the far-field and the small argument approximation for the exponential functions, the maximum magnitudes of the electric fields at the point with  $\phi$  azimuthal angle are expressed as

$$\left| \vec{E}_{via,k} \right| = \frac{\omega\mu_0 d \left| i_{via,k} e^{jk_0 l_{via,k} \cos(\phi - \phi_{via,k})} \right|}{4\pi(R - l_{via,k} \cos(\phi - \phi_{via,k}))} \approx \frac{\omega\mu_0 d \left| i_{via,k} (1 + jk_0 l_{via,k} \cos(\phi - \phi_{via,k})) \right|}{4\pi(R - l_{via,k} \cos(\phi - \phi_{via,k}))} \quad (A.12)$$

$$\begin{aligned} \left| \vec{E}_{polar} \right| &= \frac{\varepsilon_r - 1}{\varepsilon_r} \frac{\omega\mu_0 d}{4\pi(R - l_c \cos(\phi - \phi_c))} \times \left| i_p e^{jk_0 l_c \cos(\phi - \phi_c)} \text{sinc}\left(\frac{k_0 a}{2} \cos \phi\right) \text{sinc}\left(\frac{k_0 b}{2} \sin \phi\right) \right| \\ &\approx \frac{\varepsilon_r - 1}{\varepsilon_r} \frac{\omega\mu_0 d \left| i_p (1 + jk_0 l_c \cos(\phi - \phi_c)) \right|}{4\pi(R - l_c \cos(\phi - \phi_c))} \end{aligned} \quad (A.13)$$

For the small-size parallel planes, the sinc functions also are approximated to 1. Finally, the expression for the maximum radiated emission caused by the total PDN structure is greatly simplified as

$$\left| \vec{E}_{total} \right| \approx \frac{\omega\mu_0 d}{4\pi} \left| \sum_{k=0} i_{via,k} \frac{(1 + jk_0 l_{via,k} \cos(\phi - \phi_{via,k}))}{R - l_{via,k} \cos(\phi - \phi_{via,k})} + \frac{\varepsilon_r - 1}{\varepsilon_r} i_p \frac{(1 + jk_0 l_c \cos(\phi - \phi_c))}{R - l_c \cos(\phi - \phi_c)} \right| \quad (A.14)$$

The procedure for the calculation of radiated emissions is summarized in Fig A-4. The lumped-circuit model of the PDN is constructed using (A.1) with including the decoupling capacitors and the parasitic components, as shown in Fig A-2. The branch currents are analytically calculated by solving the MNA equations in (A.6). The maximum radiated emission is then calculated from (A.14) using the extracted currents. All the calculations can be effectively conducted using mathematical software such as MATLAB.

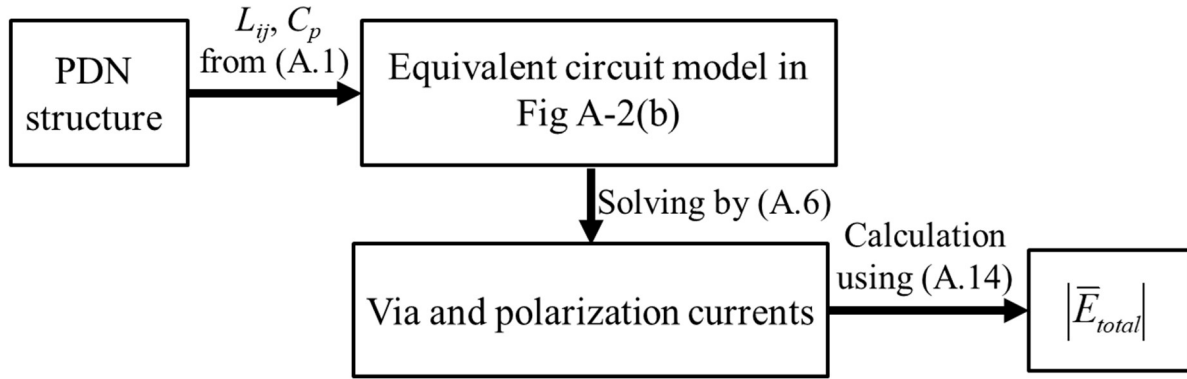


Fig A-4. Calculation procedure for the far-zone radiated emissions

### A.2.3. Validation of the closed-form expressions

The PDN at the off-chip side in Fig A-2 is designed and fabricated in a test PCB. The test board consists of a pair of parallel rectangular planes with size of 40mm by 20mm. The separation between planes  $d$  is 1 mm and filled with FR4 dielectric material of relative permittivity 4.4. The position of the IC via0 is set as (0, 0) mm, and the center of the planes is located at (16, 0) mm. An SMA port is mounted on the bottom side of the test PCB and connected to the top plane through Via 0. The two vias for the decoupling capacitors are located at (24, 8) mm and (34, -8), respectively, as shown in Fig A-5 (a). The vias for decoupling capacitors are arbitrarily placed on the test board for representation of a practical PDN. The off-chip package-level PDN impedance,  $Z_{pkg}$ , is measured at the SMA port using the vector network analyzer (VNA). The circuit model of the IC and wire bonding are then added to the measured off-chip PDN impedance by post-processing. The circuit models for the on-chip decoupling capacitance and wire bonds are adopted from those in [A-20] and [A-21]. The  $Z_{IC}$ , seen at the switching current source inside the IC, is derived using the measured  $Z_{pkg}$  and the circuit models of IC and wire bonds as

$$Z_{IC} = R_m + \left( \frac{1}{j\omega C_{on}} + R_{on} \right) \parallel (Z_{pkg} + j\omega L_{wire} + R_{wire}). \quad (A.15)$$

The measured  $Z_{pkg}$  and the  $Z_{IC}$  extracted using (A.15) are plotted in Fig A-5(b).

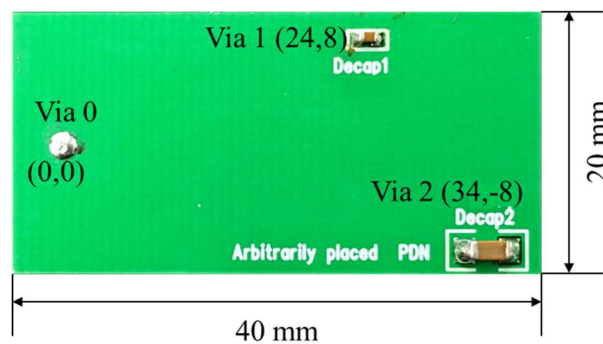
For the calculation, the test board is converted into the equivalent lumped-circuit model by (A.1)–(A.5). The circuit models of the decoupling capacitors are extracted from the VNA measurements. All the circuit parameter values are summarized in Table A-1. Using the equivalent lumped-circuit model, the  $Z_{IC}$  and  $Z_{pkg}$  are calculated and validated by comparison with the numerical results from HFSS and

in-house PEEC codes and the measurements using VNA, as shown in Fig A-5(b).

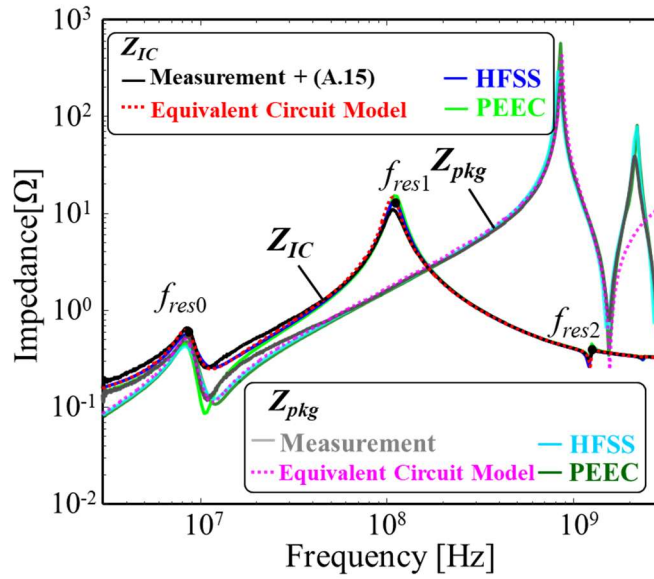
The calculated  $Z_{pkg}$  deviates from the measured one at the cavity mode resonance frequency. The  $L_{ij}$  is the DC inductance value from (A.2), and the cavity mode resonances above 2 GHz are not captured in the equivalent lumped-circuit model. However, the  $Z_{IC}$  calculated from the equivalent lumped-circuit agrees well with the numerical and measured results because the impedance peaks at the mode resonances are screened out by the low impedance path through the on-chip capacitance. In the impedance curve of  $Z_{IC}$ , the first resonance at the frequency  $f_{res0}$  is generated by the parallel resonance between the decoupling capacitance  $C_{dec1}$  and the loop inductance from the IC to both decoupling capacitors. The resonance at the frequency  $f_{res1}$  occurs between the  $C_{on}$  and the loop inductances. The resonance at the frequency  $f_{res2}$  occurs between the parallel plate capacitance,  $C_p$ , and the inductances of both vias.

Table A-1. Values of the Circuit Elements Used in the PDN Example

<i>Circuit Parameter</i>	<i>Value</i>
Parasitic resistance of the IC, $R_m$	10m $\Omega$
On-chip resistance, $R_{on}$	300m $\Omega$
On-chip decoupling capacitor, $C_{on}$	0.6nF
Bonding wire resistance, $R_{wire}$	100m $\Omega$
Bonding wire inductance, $L_{wire}$	1nH
Decap1 capacitance, $C_{dec1}$	82nF
Decap1 equivalent series resistance, $R_{dec1}$	50m $\Omega$
Decap1 equivalent series inductance, $L_{dec1}$	0.35nH
Decap2 capacitance, $C_{dec2}$	10 $\mu$ F
Decap2 equivalent series resistance, $R_{dec2}$	5m $\Omega$
Decap2 equivalent series inductance, $L_{dec2}$	1nH



(a)



(b)

Fig A-5. (a) Photograph of the test board (b) Impedance covers from the models and measurements

Next, the far-zone radiated emissions at the 3 m sphere from the test board, including the IC part, are calculated from 3 MHz to 3 GHz by using the procedure in Fig A-4 and also validated with the results using the PEEC model and HFSS, as shown Fig A-6(a). The  $E_{total,1A}$  represents the total electric field, when the  $i_{IC}$  is consistently 1A at all frequencies. The peaks of the radiated emissions are correlated with those of the  $Z_{IC}$  in Fig A-5(b). Although the resonance at  $f_{res2}$  and the cavity mode resonances do not cause impedance peaks in the  $Z_{IC}$  impedances, they cause high peaks in the radiated emissions. The closed-form expression deviates from numerical results near the first cavity resonance frequency above 2 GHz.

The radiated emissions caused by each current component can be individually calculated from (A.12) and (A.13), and also validated with the results from PEEC model in Fig A-6 (b). The computation of the radiated emissions using the PEEC method is also performed by treating all the current segments as the Hertzian dipoles. The  $E_{polar,1A}$ ,  $E_{via0,1A}$ ,  $E_{via1,1A}$ , and  $E_{via2,1A}$  represent the field components caused by each vertical current, respectively, at the condition of  $i_{IC} = 1A$ . The  $E_{via1,1A}$  and  $E_{via2,1A}$  cancel out a part of the  $E_{via0,1A}$  below the resonance frequency  $f_{res2}$ , as the  $i_{via1}$  and  $i_{via2}$  currents have the direction opposite to the  $i_{via0}$ . In addition, the radiated emission from the polarization current,  $E_{polar,1A}$ , increases near the frequency  $f_{res2}$  because the polarization current in dielectric medium resonates at the resonance frequency.



Furthermore, for more accurate validations, the radiated field patterns of the  $E_{total,1A}$  are calculated using the closed-form expression and plotted in Fig A-7. Fig A-7 (a)–(d) represent the  $H$ -plane normalized field patterns at 30 MHz, 108 MHz, 300 MHz, and 1.24 GHz, respectively. The 108 MHz and 1.24 GHz frequencies correspond to the resonance frequencies,  $f_{res1}$  and  $f_{res2}$ . The field patterns calculated using the closed-form expression agree well with the HFSS simulation results.

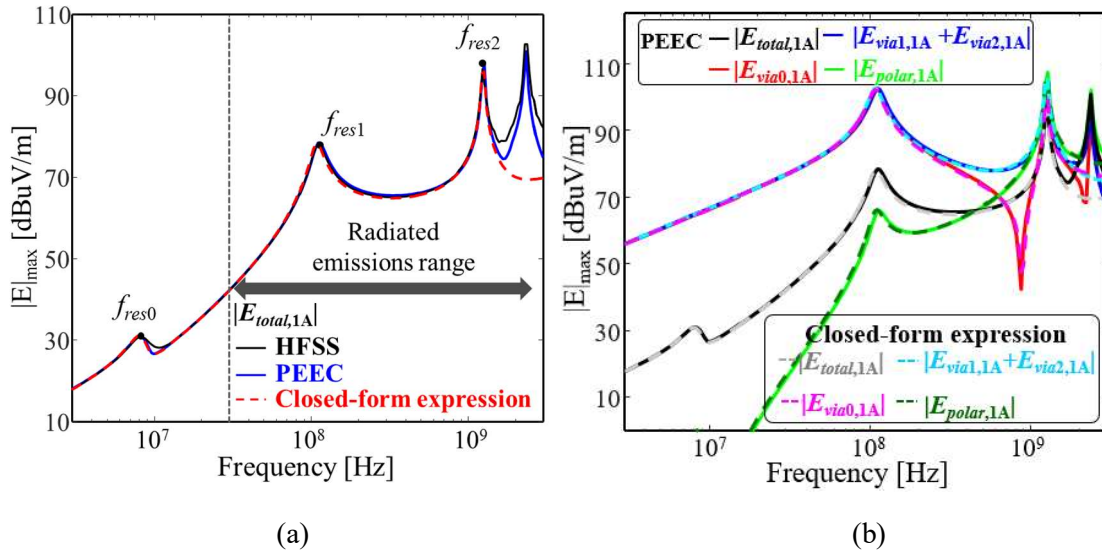
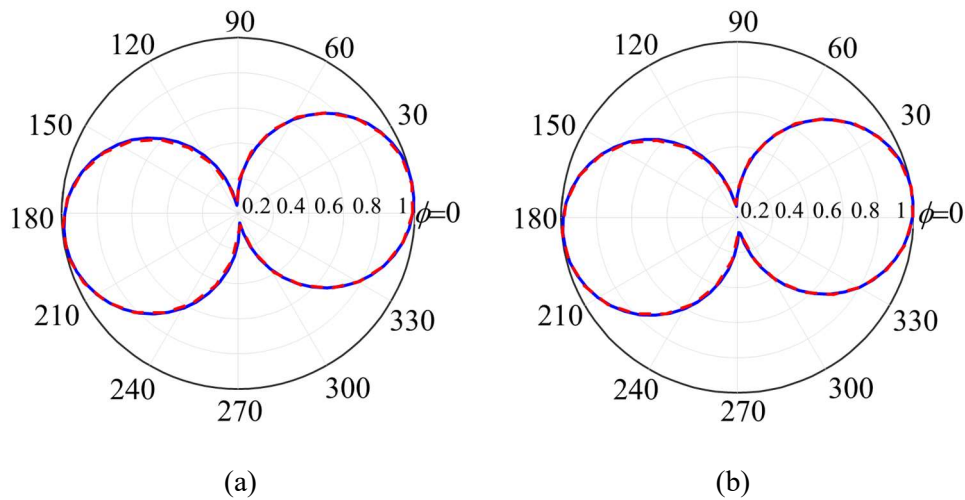


Fig A-6. Comparison among the results obtained from the closed-form expressions, PEEC model, and HFSS with  $i_{IC}=1A$  (a) Total radiated emissions (b) Radiated emissions caused by each current component



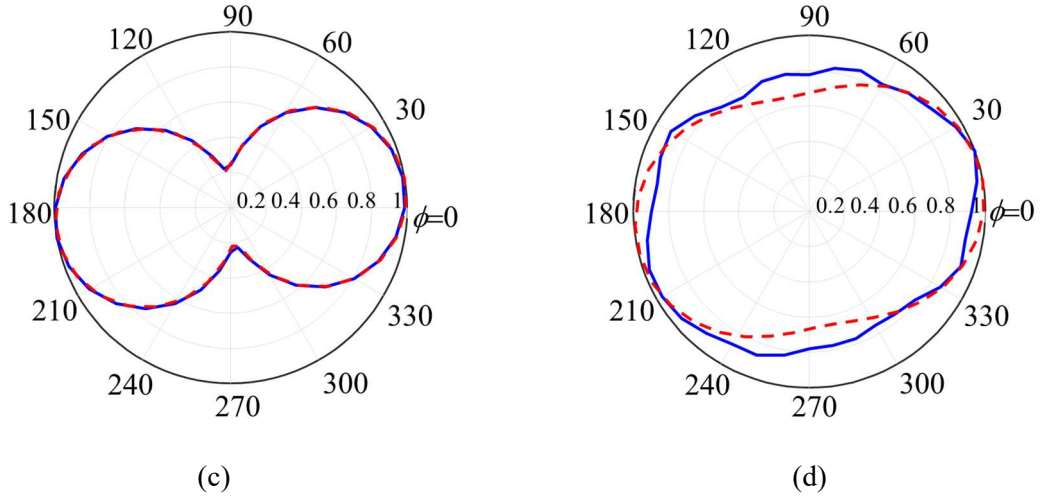


Fig A-7.  $H$ -plane normalized field patterns (solid line: HFSS, dot line: closed form expression) at (a) 30 MHz; (b) 108 MHz; (c) 300MHz; (d) 1.24 GHz

The radiated emissions calculated using the closed-form expression are also validated by measurements. The far-zone radiated emissions are measured at a 3 m distant point in a semi-anechoic chamber, as depicted in Fig A-8(a). The test board is placed on a wooden table, and the SMA port at the Via0 of the board is connected to the signal generator through a coaxial cable. A sufficient number of ferrite cores are mounted on the cable to reduce common-mode noise. Two 30 dB amplifiers are employed at the feeding and receiving cables. The radiated emissions from the test board are measured from 30 MHz to 3 GHz, as the turn table is rotated. The measured results are the radiated emissions with a particular amount of  $i_{via0}$  current, which is determined by the signal generator, cable gain, and the board input impedance,  $Z_{pkg}$ .

To validate the calculated radiated emissions with the measurements, the value of  $E_{total,1A}$ , which is the radiated emissions from the PDN, including the on-chip models at the condition of  $i_{IC} = 1A$ , is extracted from the measured results as

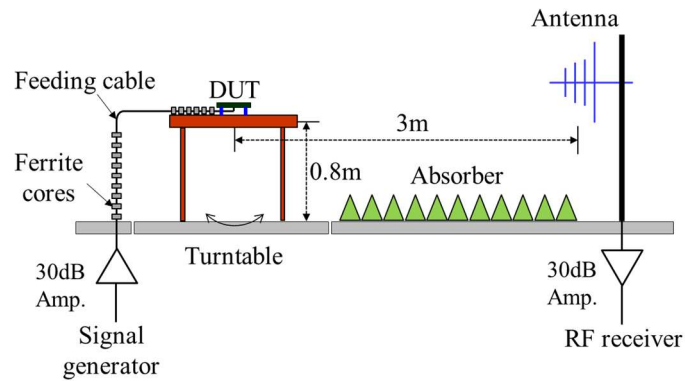
$$|E_{total,1A}| = \frac{|E_{measured}|}{|i_{via0,measured}|} \cdot |i_{via0,1A}|, \quad (A.16)$$

where  $|E_{measured}|$  represents the maximum radiated emissions directly measured in the experimental setup. The  $i_{via0,measured}$  represents the actual Via0 current in the experiments, which can be extracted by separate measurements of the cable gain. The  $i_{via0,1A}$  denotes the current when  $i_{IC}=1A$ . The  $i_{via0,1A}$  can be found from the measured  $Z_{pkg}$  and circuit model of the IC and wire bonds.

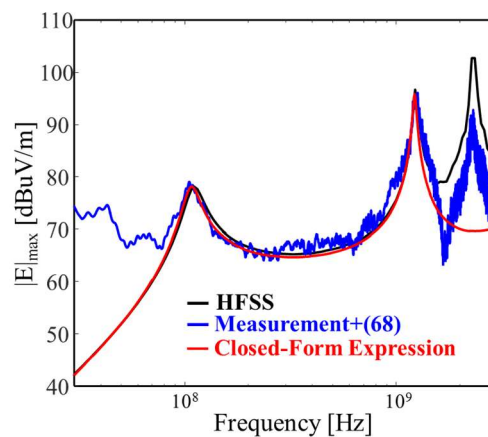
The curve of  $|E_{total,1A}|$  extracted from the measurements using (A.16) is compared with the

calculated one in Fig A-8(b). They show good agreement in the frequency range below the cavity mode resonance. The measured results below 70 MHz are not accurate due to the small signal-to-noise ratio. Consequently, the closed-form expression has been validated by HFSS, PEEC, and measurements.

In terms of computational time, the calculation using the closed-form expression is much faster than the numerical computations. In the example herein, it took about 2.8 s using the expressions, whereas it took 6196 s and 227 s using the HFSS and PEEC method, respectively. Also, the expressions can provide effective analytical solutions to find the EMI factors of the PDN structure and to develop the design guides satisfying the regulations of radiated emissions. It is assumed that the first cavity resonance frequency is higher than the interested frequency range, which is usually the case in the package-level PDN structure



(a)



(b)

Fig A-8. (a) Maximum radiated emissions measurement setup in a semi-anechoic room (b) Maximum radiated emissions

## A.3. Quantified Design Guides of The PDN for Reduction of Radiated Emissions

The regulation of radiated emissions is normalized by the switching current spectrum in quantifying the design guides for the PDN. The package-level PDN structure shown in Section A.2 is used for demonstration. The major sources of the radiated emissions at each frequency range are analytically investigated by sensitivity analysis using the equivalent lumped-circuit model. A systematic procedure for developing a quantified design guidelines for the package-level PDN is proposed.

### A.3.1. Normalized regulation for radiated emissions

The spectrum of IC switching currents should be considered in designing the PDN structures for reduction of radiated emissions. The switching currents occur at the rising and falling transitions of the I/O or logic circuits. The switching currents can be approximated as a train of triangular impulses [A-21]. The spectrum of the periodic triangular impulses has peaks at the harmonics of the fundamental frequency. The periodic triangular current impulses with 800 mA peak, 500 ps rise/fall time, and 8 ns period are utilized as the IC switching currents herein. The actual radiated emissions caused by the IC current impulses on the PDN structures,  $|E_{total}|$ , are obtained by multiplication of the radiated emission due to 1A current spectrum and the spectrum of the IC currents, as depicted in Fig A-9(a). The actual radiated emissions are then compared with the regulations for radiated emissions, such as the federal communications commission (FCC) regulation. The design is successful in the view of radiated emissions, if

$$|E_{reg}| > |E_{total,1A}| \cdot |i_{IC}(f)|, \quad (A.17)$$

where the  $|E_{reg}|$ ,  $|E_{total,1A}|$ , and  $i_{IC}(f)$  represent the maximum limit of the radiated emissions regulation, the radiated emissions from the PDN due to 1A IC current, and the spectrum of the IC switching current, respectively.

The actual radiated emissions are determined by the spectrum of IC switching currents and the radiated emissions property of the PDN structure itself. When the actual radiated emission violates the  $|E_{reg}|$ , it is difficult to distinguish whether the spectrum of switching currents is more responsible or the PDN structure is. Thus, it is not effective to extract the design guidelines of the PDN from the actual radiated emissions directly.

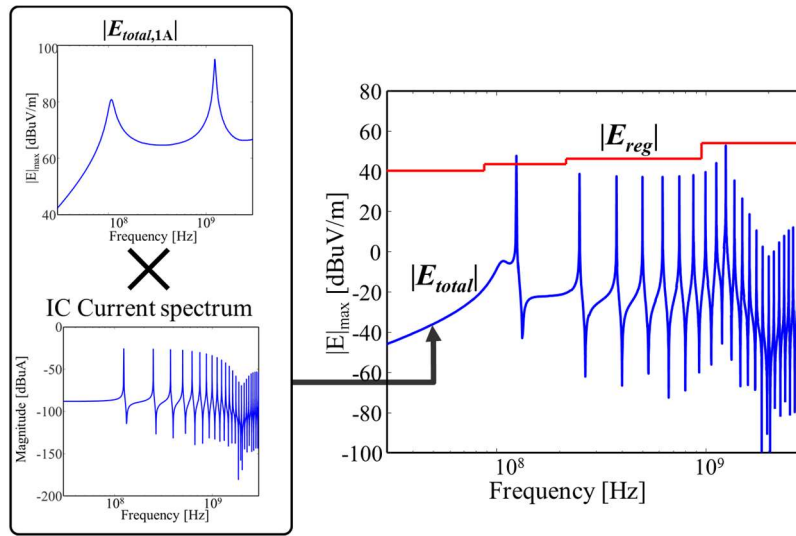
The characteristics of the radiated emissions from PDN structures can be more clearly identified

from  $|E_{total,1A}|$ . Correspondingly, the  $|E_{reg}|$  is divided by the  $i_{IC}(f)$ , and the equation (A.17) is modified as

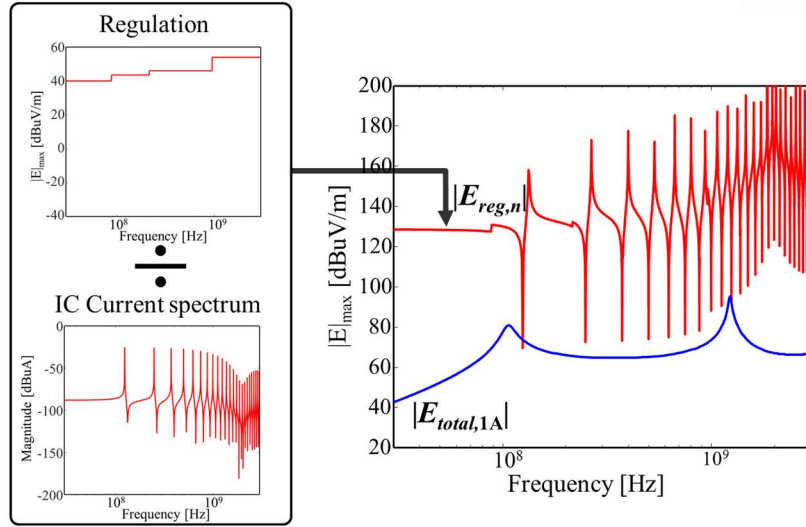
$$|E_{reg,n}| > |E_{total,1A}|, \quad (A.18)$$

$$\text{where } |E_{reg,n}| = \frac{|E_{reg}|}{|i_{IC}(f)|}. \quad (A.19)$$

$|E_{reg,n}|$  represents the radiated emissions regulation normalized by the spectrum of IC switching currents. The peaks in the current spectrum result in the valleys in the  $|E_{reg,n}|$ , as shown in Fig A-9(b). The characteristics of the current spectrum are included in the  $|E_{reg,n}|$ . Using the  $|E_{reg,n}|$  and the  $|E_{total,1A}|$  in Fig A-9(b), the effects of only the PDN geometry on the radiated emissions are much clearer than the actual radiated emissions in Fig A-9(a). The violation of radiated emissions may occur if the valleys of the  $|E_{reg,n}|$  and the peaks of the  $|E_{total,1A}|$  arise at the same frequency. The violation can be avoided by suppressing the magnitude or moving the peak frequencies of  $|E_{total,1A}|$ .



(a)



(b)

Fig A-9. (a) Comparison between the  $|E_{reg}|$  and the actual radiated emissions (b) Comparison between  $|E_{reg,n}|$  and the radiated emissions due to the 1A switching current at all frequencies

### A.3.2. Dominant current path at each frequency region and sensitivity analysis

The decoupling capacitors in the PDN play a role as the hierarchical charge reservoirs for the ICs. The hierarchical decoupling capacitors cause the multiple poles and zeros in the impedance curve, as shown in Fig A-5(b). The dominant current paths between the IC and the charge reservoirs vary with the frequency. The major sources of the radiated emissions also are changing with the frequency.

The current components on the PDN are solved from (A.6) using the equivalent lumped-circuit model with the 1A IC current source. The magnitude of current components is plotted in Fig A-10(a). Major current paths in each frequency region can be found from the magnitudes of the branch currents, as illustrated in Fig A-10(b)–(e).

First, in the frequency range lower than  $f_{res0}$ , only the  $i_{via0}$  and  $i_{via2}$  have significant values, which indicates that most of the IC current flows through Via0 and Via2. In the example herein, the  $f_{res0}$  is lower than the low frequency limit of the emission regulations. At the frequencies between  $f_{res0}$  and the  $f_{res1}$ , a large amount of the  $i_{via0}$  flows through the Via1 because the low impedance path is formed by the Decap1, as described in Fig A-10(b). The main current path is indicated by a red solid line, and the remaining current path is shown by a red dashed line. The radiated emissions caused by the  $i_{via1}$

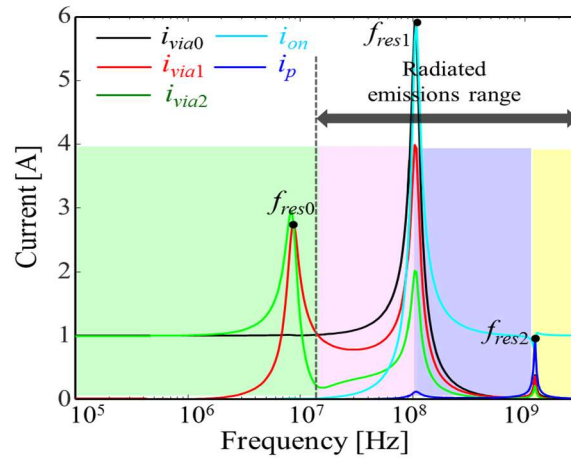
cancel a part of those caused by the  $i_{via0}$  due to that the current direction for  $i_{via0}$  and  $i_{via1}$  is opposite to each other. The cancelling amount is dependent on the exact amount of each current and the distance between the Via0 and Via1, resulting in the total radiated emissions varying with frequency. Hence, the distance from the IC to the Decap1 and the circuit parameters placed along the current path are the major EMI factors in this case.

At the  $f_{res1}$  resonance frequency, as observed in Fig A-10(a), the amount of the  $i_{via0}$ ,  $i_{via1}$ , and  $i_{via2}$  are greatly increasing due to the parallel resonance between the on-chip capacitance and the inductance from the IC to the decoupling capacitors. The currents flowing through the decoupling capacitors are in antiphase with the  $i_{via0}$  due to the resonance condition, as denoted with the green line in Fig A-10(c). The peak of the currents is dependent on the quality factor of the resonance, which is determined by the capacitance, inductance, and resistance in the current loop. Correspondingly, the radiated emission at the  $f_{res1}$  frequency can be adjusted by the distance from the IC to the decoupling capacitors and the resistance in the current path.

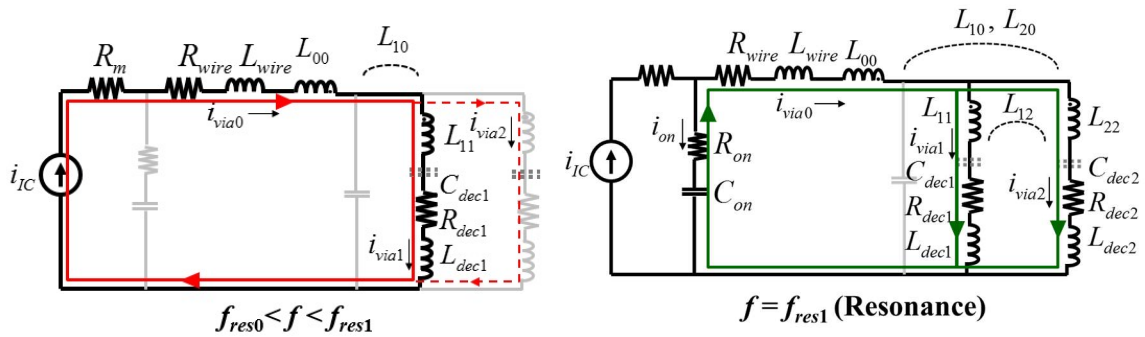
After the  $f_{res1}$  frequency, the low impedance path is generated by the on-chip capacitance, and most of the IC current returns through the on-chip capacitance. The  $i_{via0}$  and  $i_{via1}$  are greatly reduced, as shown by the red dashed line in Fig A-10(d). Therefore, the radiated emissions in the frequency range between the  $f_{res1}$  and the  $f_{res2}$  are not so high. Some amount of the IC current still flows through the Decap1, contributing to the radiated emissions. The radiated emission in this region also can be suppressed by adjusting the distance between the IC and the Decap1.

At the next resonance frequency,  $f_{res2}$ , the amount of the  $i_p$ ,  $i_{via1}$ , and  $i_{via2}$  are greatly increased. The resonance occurs between the parallel plate capacitance and the inductances of bonding wires and both vias. The currents in antiphase with the  $i_p$  flow through all the vias due to the parallel resonance, as depicted with green lines in Fig A-10(e). Because the current  $i_p$  is large, the polarization currents in the dielectric medium also have significant contributions to the radiated emission. In this case, increasing the ESR of the decoupling capacitors would be effective for reduction of the radiated emission by reducing the quality factor of the resonance.



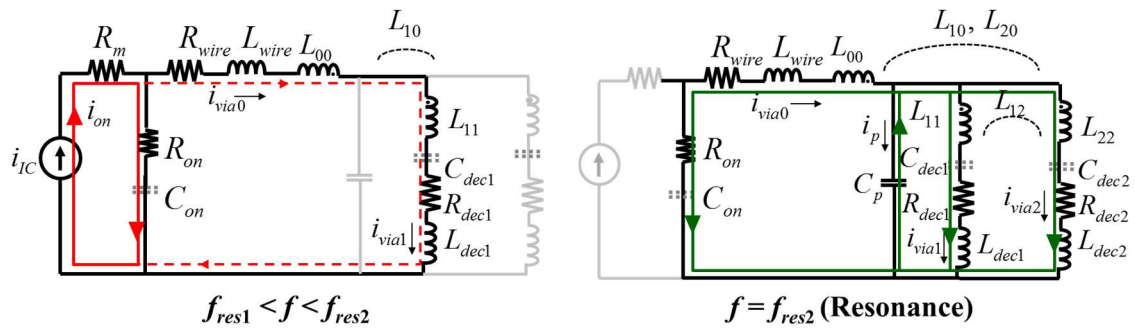


(a)



(b)

(c)



(d)

(e)

Fig A-10. (a) Current components obtained by solving (A.6) for the PDN lumped-circuit model (b) Dominant current path for the radiated emissions in the frequency range below the  $f_{res1}$  (c) Path at the resonance frequency of  $f_{res1}$  (d) Path in the frequency range between the  $f_{res1}$  and the  $f_{res2}$  (e) Path at the resonance frequency of  $f_{res2}$

It is found in (A.14) that the radiated emissions are affected by the distance between the vias and



the amount of currents, which are obtained from the PDN lumped-circuit model. The closed-form expression for the radiated emission can be analytically written in terms of all circuit parameters and the PCB geometry; however, the expression is complicated to investigate the effect of each parameter directly. To quantitatively inspect the effects of the decoupling capacitors and the PDN geometry, the sensitivity of the radiated emission due to each variable is analytically calculated as

$$S_x^{E_{total,1A}} = \frac{x}{|E_{total,1A}(x)|} \frac{\partial |E_{total,1A}(x)|}{\partial x}, \quad (A.20)$$

where the  $x$  represents a variable affecting the radiated emission, such as the distance between the vias and the circuit parameters in Table 4-1. The  $x$  is set as a PDN variable at the first step in the procedure of Fig A-4, and the calculation procedures for the radiated emissions using (A.6) and (A.14) are performed. That is, the currents are given as the function of the  $x$  by solving (A.6), and the expression of the radiated emission is then derived as the function of the  $x$ ,  $|E_{total,1A}(x)|$ , using (A.14). Specifically, when the variable  $x$  represents one of the PDN geometries, such as the PCB size and the distance between the vias, it is used in the equation (A.14) as well as the generation of PDN circuit model. When the variable  $x$  represents a value of the circuit elements in Table A-1, it is used only in the generation of PDN circuit model.

The sensitivity of the radiated emission to several dominant parameters has been calculated at several frequencies, and the results are summarized in Table A-2. The 30 MHz, 108 MHz, 300 MHz, and 1.24 GHz correspond to the frequencies for the cases of Figs. A-10(b), (c), (d), and (e), respectively. Based on the sensitivities in Table A-2, it is expected that the radiated emissions in all frequency ranges effectively can be suppressed by placing the Decap1 closer to the IC. Although the current through the Decap2 is much smaller than the current through the Decap1, as shown in Fig A-10(a), it is also expected that the adjustment of the  $l_{via2}$  would have some effects on the radiated emissions. As examples, the radiated emissions at  $f=30\text{MHz}$  and  $f=300\text{MHz}$  have been calculated with varying the  $l_{via1}$  from 2mm to 30mm ( $\phi_{via1}=18.4^\circ$ ) and plotted in Fig A-11(a). It is clearly shown that the emissions are reduced by decreasing the  $l_{via1}$ .

The sensitivities to the  $R_{dec1}$  and  $R_{dec2}$  at the resonance frequencies have negative values. Thus, increasing the  $R_{dec1}$  and  $R_{dec2}$  would reduce the radiated emissions at the resonance frequencies. The radiated emissions at  $f=108\text{ MHz}$  and  $f=1.24\text{ GHz}$  also have been calculated with varying the  $R_{dec1}$  from 0 m $\Omega$  to 700 m $\Omega$ , and plotted in Fig A-11(b). The results are correlated well with the sensitivity analysis.

Actually, the sensitivity analysis also can be performed based on the parametric sweep using a full-

wave solver, but it takes a much longer time than using the closed-form expression. As an example, the sensitivity analysis of the  $R_{dec1}$  at 30 MHz was performed using both HFSS and the closed-form expressions. It took 2755s in HFSS, whereas it took 9.8 s using the closed-form expressions.

Table A-2. Sensitivity of Radiated Emissions to PDN Parameters

Parameters	30MHz	108MHz( $f_{res1}$ )	300MHz	1.24GHz( $f_{res2}$ )
$l_{via1}$	0.8158	0.6055	0.2599	-0.6678
$l_{via2}$	0.2135	0.0762	0.0487	-1.5138
$R_{dec1}$	0.0014	-0.0745	-0.0018	-0.1463
$R_{dec2}$	0	-0.002	0	-0.0050

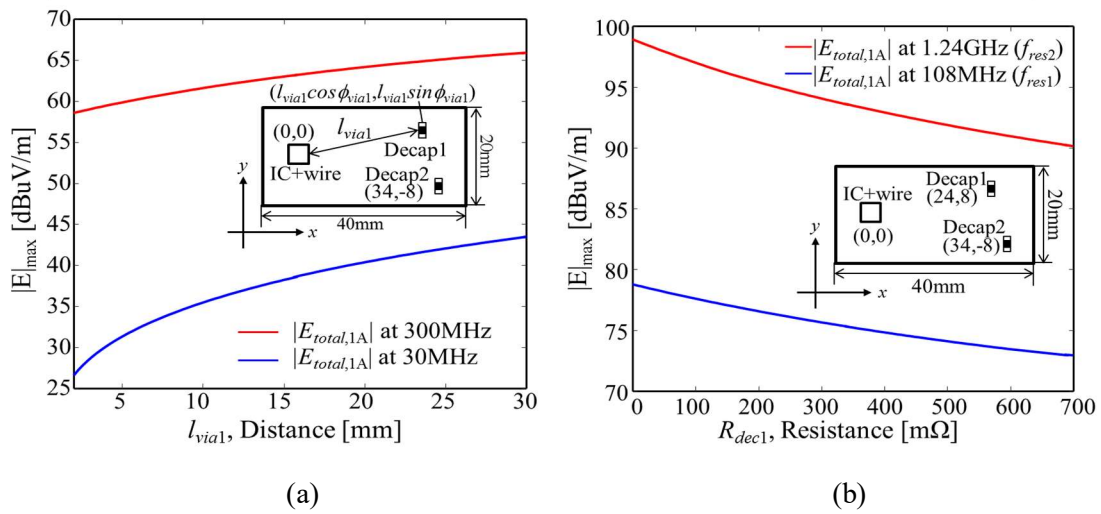


Fig A-11. Radiated emission (a) at 30 MHz and at 300 MHz with varying  $l_{via1}$  (b) Resonance frequencies (108 MHz, 1.24 GHz) with varying  $R_{dec1}$

### A.3.3. Extraction of optimal distance between the vias and the ESR values for target radiated emission level

The distance between vias in the dominant current path is the major EMI factor in each frequency range. In addition, high ESR values of the decoupling capacitors are effective in suppressing the radiated emission at the resonance frequencies. Accordingly, the radiated emissions can be controlled by adjusting the position of the decoupling capacitor and the ESR values. The ESR value depends on the physical size and capacitance of the decoupling capacitor. The ESR value of the decoupling capacitor is a controllable parameter [A-22]–[A-24].

A dominant current path is usually formed between the IC and one of the hierarchical decoupling

capacitors, as shown in Fig A-10(a). Two vertical currents in the dominant current path are major sources of the radiated emissions. Even though all the currents affect the radiated emissions at the resonance frequencies, two of the vertical currents still have more dominant effects than the others. Thus, the radiated emission of (A.14) is maximized at the observation point along the extended line of the dominant current path. Accordingly, the maximum radiated emission of (A.14) is obtained at the observation point with the azimuth angle equal to the azimuth angle of the via providing the dominant current path as  $\phi = \phi_{via,k}$ . By reversing the calculation procedure of Fig A-4, the optimal via positions and ESR values can be directly extracted from the target level for radiated emissions. At first, as explained in the previous subsection for the sensitivity analysis, the expression of the radiated emission is written as the function of the target variable,  $x_{target}$ , whose value should be extracted. The values of all other parameters except for the  $x_{target}$  are fixed with certain values. The radiated emission as the function of target variable,  $|E_{total,1A}(x_{target})|$  is then set to the target radiated emission level,  $|E|_{target}$ , as

$$|E_{total,1A}(x_{target})| = |E|_{target} \quad . \quad (A.21)$$

Although (A.21) is complicated, the target values for the optimal via positions and ESR can be solved using the mathematical software MATLAB.

### A.3.4. Control of the resonance frequency

The resonances in the PDN occur due to the capacitance and the inductance in the current paths, as shown in Figs A-10(c) and (e). When the resonance peak is overlapped with a valley in the normalized regulation due to the IC current spectrum, as illustrated in Fig A-9(b), changing the resonance frequency should be the most effective way to avoid violation of regulations. The resonance frequency can be adjusted by tuning the board size and the capacitance of the decoupling capacitance. Accordingly, control of resonance frequencies is one of the important design considerations for radiated emissions.

Although the first resonance,  $f_{res0}$ , is out of the frequency range of radiated emissions in the test PDN, the resonance may occur in the frequency range of radiated emissions, if the  $C_{dec1}$  is smaller. Thus, the resonance also should be considered in the design. The expression of the  $f_{res0}$  is written as

$$f_{res0} = \frac{1}{2\pi\sqrt{C_{dec1}(L_{11} + L_{dec1} + L_{22} + L_{dec2})}} \quad . \quad (A.22)$$

The  $f_{res0}$  is predominantly determined by the self-inductance of the vias, the ESL in the decoupling

capacitors, and the  $C_{dec1}$ . The  $f_{res0}$  can be tuned by the capacitance of the Decap1.

The decoupling capacitors can be considered as the ESL after their self-resonance frequencies. The effects of resistance on the resonance frequency are small and neglected for simplicity. With neglecting the resistances, the relation of the voltages and currents in the PDN lumped-circuit model of Fig A-2 can be expressed as

$$\begin{bmatrix} v_P - v_{in} \\ v_P \\ v_P \end{bmatrix} = j\omega \begin{bmatrix} L_{00} & L_{01} & L_{02} \\ L_{10} & L_{11} + L_{dec1} & L_{12} \\ L_{20} & L_{21} & L_{22} + L_{dec2} \end{bmatrix} \begin{bmatrix} -i_{via0} \\ i_{via1} \\ i_{via2} \end{bmatrix}. \quad (A.23)$$

The sum of the  $i_{via1}$  and  $i_{via2}$  is equal to the  $i_{via0}$ , and (A.23) can be modified as

$$\begin{bmatrix} B_{00} & B_{01} + B_{02} \\ B_{10} + B_{20} & B_{11} + B_{12} + B_{21} + B_{22} \end{bmatrix} \begin{bmatrix} v_P - v_{in} \\ v_P \end{bmatrix} = j\omega \begin{bmatrix} -i_{via0} \\ i_{via0} \end{bmatrix}. \quad (A.24)$$

The  $B$  matrix in (4.24) represents the inverse matrix of the inductance matrix in (A.23). By inverting the  $2 \times 2$   $B$  matrix in (4.24), the equivalent inductance matrix can be expressed as

$$\begin{bmatrix} L_{e00} & L_{e01} \\ L_{e10} & L_{e11} \end{bmatrix} = \begin{bmatrix} B_{00} & B_{01} + B_{02} \\ B_{10} + B_{20} & B_{11} + B_{12} + B_{21} + B_{22} \end{bmatrix}^{-1}. \quad (A.25)$$

The  $3 \times 3$  inductance matrix (A.23) is converted into the  $2 \times 2$  equivalent inductance matrix in (A.25) [A-16]. Finally, the test PDN is simplified to the circuit model in Fig A-12(a), which is then used for calculation of resonance frequency. The self-inductance of Via0 is retained in the  $L_{e00}$ , and the inductance of Via1 and Via2 is merged as the  $L_{e11}$ . The  $L_{e01}$  represents the mutual inductances between the Via0 and the vias connected to the decoupling capacitors. The total equivalent inductance,  $L_{eq}$ , seen at the IC can be expressed as  $L_{eq} = L_{wire} + L_{e00} + L_{e11} - L_{e01} - L_{e10}$ .

Using the simplified equivalent circuit, it is found that the  $C_{on}$  and the  $L_{eq}$  produce the parallel resonance at the  $f_{res1}$ . Also, the  $C_p$  and all inductances produce the parallel resonance at the  $f_{res2}$ . The expressions are obtained as

$$f_{res1} = \frac{1}{2\pi\sqrt{C_{on}L_{eq}}}. \quad (A.26)$$

$$f_{res2} = \frac{1}{2\pi\sqrt{\left(\frac{L_{wire} + L_{e00} + L_{e11} - 2L_{e01}}{(L_{wire} + L_{e00})L_{e11} - L_{e01}^2}\right)C_p}}. \quad (A.27)$$

Although the  $L_{eq}$  can be adjusted by the ESL and the via position, the degree of freedom in

adjusting the  $f_{res1}$  is quite low because the  $C_{on}$  is fixed by the ICs. On the other hand, the  $f_{res2}$  can be tuned by the PDN geometry because the  $C_p$  can be controlled by the PCB size and thickness.

The calculation procedure of the resonance frequencies in the PDN structure also is depicted in Fig A-12(b). The first and second steps are the same as those in Fig A-4. In the third step, the PDN lumped-circuit model is simplified by merging the inductances from (A.23), (A.24), and (A.25). The expressions of the resonance frequencies are finally given as using (A.22), (A.26), and (A.27).

Similarly, by reversing the calculation procedure of Fig A-12(b), the optimal values for the PDN structure can be directly extracted from the target resonance frequency as

$$f_{res,k}(x_{target}) = f_{res,k,target} \quad (A.28)$$

The  $f_{res,k}$  and  $f_{res,k,target}$  represent one of the resonance frequencies from (A.22), (A.26), and (A.27), and the corresponding target resonance frequency. The  $x_{target}$  would be the plane geometry or the  $C_{dec1}$ . The  $f_{res,k}(x_{target})$  is the function of the  $x_{target}$  to extract the design value. Equation (A.28) also can be analytically solved using MATLAB, and the  $x_{target}$  is extracted as the design factor.

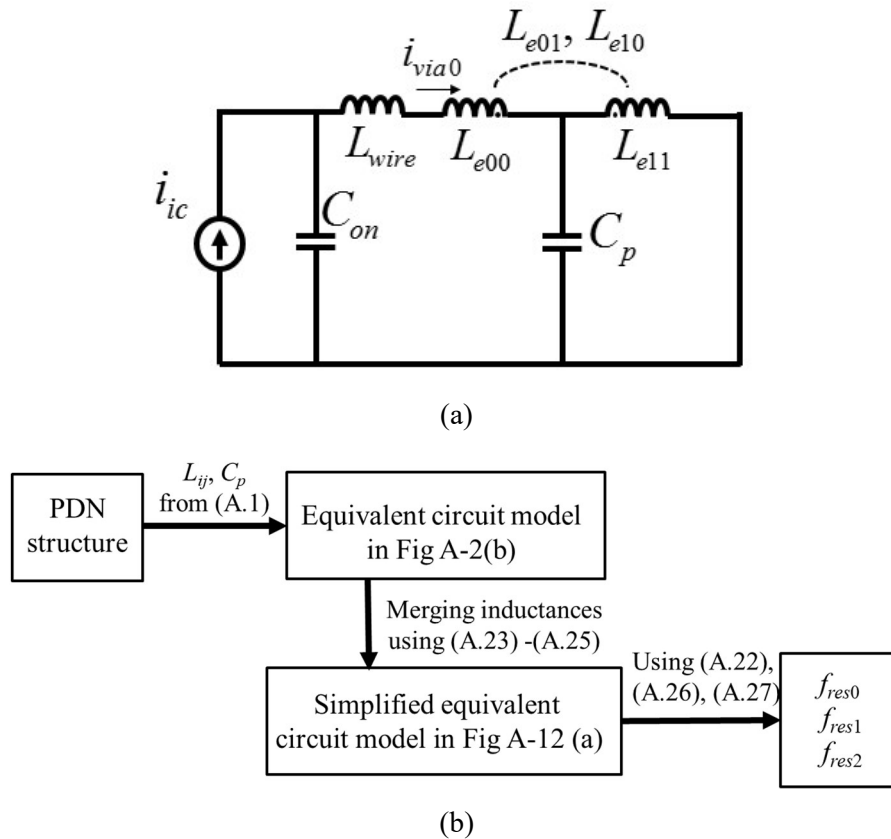


Fig A-12. (a) Simplified equivalent model of the test PDN structure (b) Calculation procedure of the resonance frequencies

### A.3.5. Flow chart of the quantified design guides

The design flows for the optimal PDN structure are summarized in Fig A-13(a). The  $f_{res,k}$  represents the resonance frequency, which is determined by (A.22), (A.26), and (A.27). The  $l_{via,k}$ ,  $R_{dec,k}$ , and  $C_{dec,k}$  represent the distance between the Via0 and the Via, $k$ , the ESR, and the capacitance of the  $k$ th decoupling capacitor, respectively. A prototype PDN is given at first, and the radiated emissions due to the 1A switching current are calculated using the calculation procedure of Fig A-4. The  $|E_{reg,n}|$  is also calculated from (A.19) using the IC current spectrum. The radiated emissions of the prototype PDN is evaluated at the third stage with checking the violation of the regulation. When the  $|E_{total,1A}|$  is below the  $|E_{reg,n}|$ , the prototype PDN structure is a successful design.

If the radiated emission of the prototype PDN violates the regulation at the  $f_{res,k}$ , the resonance frequency is moved to a target value by adjusting a target variable based on (A.28). When the violation occurs at the resonance between the capacitance of a decoupling capacitor  $C_{dec,k}$ , and the loop inductance, the  $f_{res,k}$  can be adjusted by changing the  $C_{dec,k}$  based on (A.22). When the violation occurs at the resonance between parallel plate capacitance,  $C_p$ , and the via inductances, the  $f_{res,k}$  can be controlled by adjusting the PCB size based on (A.27). The magnitude of radiated emissions at the  $f_{res,k}$  also can be suppressed by increasing the ESR value in the dominant current path. The ESR value can be assigned as the target variable as well. In this case, the radiated emissions are written as the function of  $R_{dec,k}$ , and the optimum ESR value is extracted by solving  $|E_{total,1A}(R_{dec,k})| = |E|_{target}$ . Because the ESR cannot be adjusted precisely, an ESR value larger than optimal ESR can be chosen.

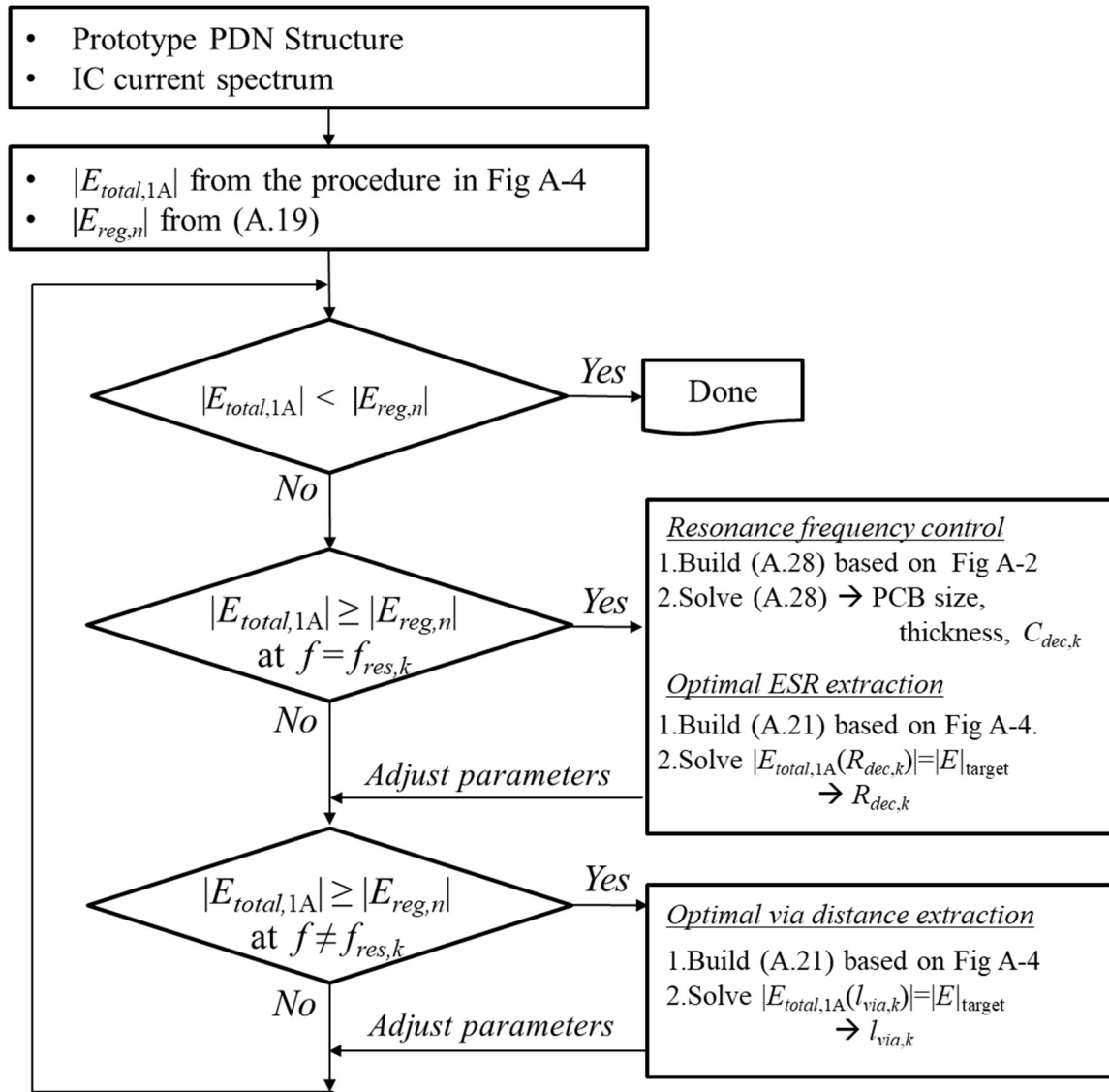
When the radiated emissions exceeds the  $|E_{reg,n}|$  at a frequency range other than the resonance frequencies,  $f \neq f_{res}$ , the dominant current path should be found using the equivalent lumped-circuit model to calculate the target distance between the Via0 and Via, $k$ . The  $|E_{total,1A}(l_{via,k})|$  is derived based on the procedure in Fig A-4 by setting the  $l_{via,k}$  as a variable at the first step. The optimal  $l_{via,k}$  is extracted by solving the  $|E_{total,1A}(l_{via,k})| = |E|_{target}$ . At the final stage in Fig A-13(a), the PDN design is modified according to the values extracted at the previous stages. The radiated emission of the modified PDN will be checked to confirm whether it satisfies the normalized regulation. When the radiated emissions are below the regulation, the modified design is successful. Otherwise, the design flow is repeated for a fine tune.

As an example, the PDN structure and the current spectrum shown in Fig A-9 are used as the prototype design. Although the normalized regulation  $|E_{reg,n}|$  is absent below 30 MHz due to the absence of the FCC radiated emission regulation, the calculated radiated emissions for the prototype and optimized PDN are plotted from 3 MHz to check the variation in wide frequency range. In Fig

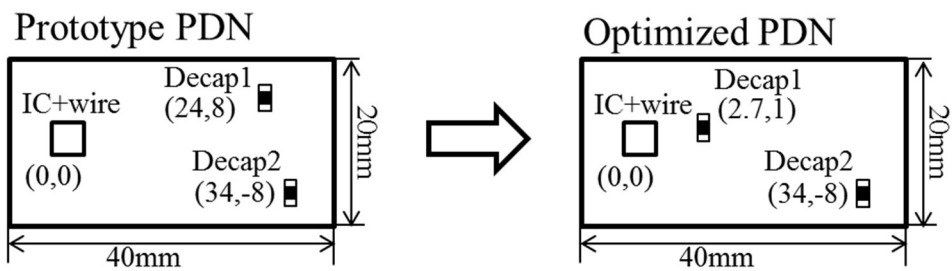
A-13(b), the prototype PDN violates the normalized regulation at 125 MHz and 1.25 GHz. The violations at 125 MHz and 1.25 GHz correspond to the cases of  $f \neq f_{res}$ , and  $f = f_{res}$ , respectively. The violation at 1.25 GHz is suppressed by using a high ESR. The ESR in the Decap1 is changed 5 m $\Omega$  into 400 m $\Omega$  based on the optimal ESR extraction process with  $|E|_{\text{target}}=90$  dBuV for 3 dB margin. At the 125 MHz, the path from the IC to the Decap1 is the dominant current path, as shown in Fig A-10(a). The radiated emission can be reduced below the  $|E_{reg,n}|$  by placing the Decap1 at the optimal  $l_{via1}$ . The optimal  $l_{via1}$  is derived as 2.9 mm from the process of the optimal distance extraction with  $|E|_{\text{target}}=67$  dBuV for 3 dB margin. After applying the optimal  $l_{via1}$  and  $R_{dec1}$ , the  $f_{res2}$  is changed from 1.24 GHz to 1.125 GHz. At the third stage, the  $|E_{total,1A}|$  from the optimized PDN is checked again and passes the regulation. The radiated emissions of the optimized PDN is reduced below the normalized regulation, as shown in Fig A-13(b).

The PDN satisfying the emission regulation also can be designed using a full-wave solver by optimizing and tuning. However, it takes much more time and effort because the optimization using a full-wave solver is based on the parametric sweep. For the design example herein, it took over 3 hours using HFSS, whereas it took just about 5 min using the proposed design flow in Fig A-13(a).

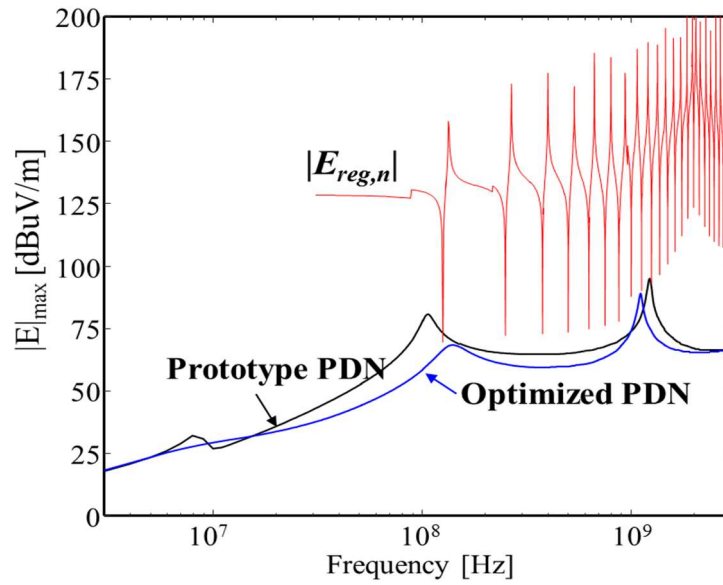




(a)







(b)

Fig A-13. (a) PDN design flow satisfying the regulation of radiated emissions (b) Radiated emissions from the prototype PDN and the optimized PDN

## A.4. Summary

The package-level PDN is modeled as lumped-circuits using the cavity equivalent circuit model. The via currents and the dielectric polarization currents are calculated from the circuit model. The closed-form expression of the radiated emissions is developed and validated with the numerical calculations and the experiment. The regulation for radiated emissions is normalized by the spectrum of switching currents and compared with the radiated emission of the PDN due to the 1A current source at all frequencies. The effect of the PDN structure on the radiated emissions can be clearly identified in this way. The effects of EMI factors are investigated based on the dominant current paths and the sensitivity analysis.

For design applications, a systematic procedure for developing quantified PDN design guidelines to suppress the radiated emissions is proposed using the closed-form expressions. The optimal ESR of decoupling capacitors and the distance between the vias are quickly extracted using the proposed calculation procedure. The design flows are demonstrated using a prototype PDN example. The proposed design method also can be utilized for PCB-level PDN designs with small power and GND planes. The method allows the EMC-aware PDN design in the initial design stage.

## REFERENCES

- [A-1] S. Radu and D. Hockanson, "An investigation of PCB radiated emissions from simultaneous switching noise," in *Proc. IEEE Int. Symp. Electromag Compat.*, Seattle, WA, Aug. 1999, pp. 893–898
- [A-2] J.P. Leca, N. Froidevaux, P. Dupre, G. Jacquemod, Braquet, H. "EMI measurements, modeling, and reduction of 32-Bit high-performance microcontrollers," *IEEE Trans. Electromagn. Compat.*, vol.56, no.5, pp.1035 – 1044, Oct. 2014
- [A-3] T. Sudo, H. Sasaki, N. Masuda and J. L. Drewniak, "Electromagnetic Interference (EMI) of System-on-Package (SOP)," *IEEE Trans. Adv. Packag.*, vol. 27, NO. 2, May. 2004.
- [A-4] T. H. Hubing, J. L. Drewniak, T. P. Van Doren, and D. M. Hockanson, "Power bus decoupling on multilayer printed circuit boards," *IEEE Trans. Electromagn. Compat.*, vol. 37, no. 2, pp. 155–166, May 1995.
- [A-5] A.E. Ruehli and H. Heeb, "Circuit models for three-dimensional geometries including dielectrics," *IEEE Trans. on Microw. Theory Tech.*, vol.40, no.7, pp.1507-1516, Jul 1992
- [A-6] W. Yahyaoui, L. Pichon, and F. Duval, "A 3D PEEC Method for the Prediction of Radiated Fields From Automotive Cables," *IEE Trans. Magn.*, vol.46, no.8, pp.3053-3056, Aug. 2010
- [A-7] B. Archambeault and A. E. Ruehli, "Analysis of power/ground-plane EMI decoupling performance using the partial-element equivalent circuit technique," *IEEE Trans. Electromag. Compat.*, vol. 43, no. 4, pp. 437- 445, Nov. 2001
- [A-8] J. Park, J. Lee, B. Seol, J. Kim, "Efficient Calculation of Inductive and Capacitive Coupling Due to Electrostatic Discharge (ESD) Using PEEC Method," *IEEE Trans. Electromag. Compat.*, vol.57, no.4, pp.743-753, Aug. 2015
- [A-9] M. Leone, "The radiation of a rectangular power-bus structure at multiple cavity-mode resonances," *IEEE Trans. Electromagn. Compat.*, vol. 45, no. 3, pp. 486–492, Aug. 2003.
- [A-10] H. W Shim and T.H. Hubing, "A closed-form expression for estimating radiated emissions from the power planes in a populated printed circuit board," *IEEE Trans. Electromag. Compat.*, vol.48, no.1, pp.74-81, Feb. 2006.
- [A-11] S. Jeong, B. Jung, K. Hong, H. Kim, Y. Kim and J. Kim "Analytical calculation of electromagnetic fields near parallel power planes with decoupling capacitors for RF interference

- estimation", *Proc. Electrical Design of Advanced Packaging and Systems Symposium (EDAPS 2015)*, pp. 136-139, Dec. 2015.
- [A-12]Y.T. Lo, W. Solomon, and W.F. Richards, "Theory and experiment in microstrip antennas," *IEEE Transactions on Antenna and Propagation*, vol. AP-7, no.2, 137-145, Mar. 1979.
- [A-13]C. Wang, J. Mao, G. Selli, S. Luan, L. Zhang, J. Fan, D. J. Pommerenke, R. E. Dubroff, and J. L. Drewniak, "An efficient approach for power delivery network design with closed-form expressions for parasitic interconnect inductance," *IEEE Trans. Advanced Packaging*, vol. 29, no. 2, pp. 320-334, May 2006.
- [A-14]M. Friedrich and M. Leone, "Inductive Network Model for the Radiation Analysis of Electrically Small Parallel-Plate Structures," *IEEE Trans. Electromagn. Compat.*, vol.53, no.4, pp.1015-1024, Nov. 2011
- [A-15]D. Shin, J. Park, N. Kim, J. Lee, Y. Park, and J. Kim, "Efficient Calculation of EMI Factors from Power Distribution Network using Cavity Resonance Circuit Model," *Proc. Electrical Design of Advanced Packaging and Systems Symposium (EDAPS 2015)*, pp. 140-143, Dec. 2015
- [A-16]J. Kim, L. Ren, J. Fan, "Physics-Based Inductance Extraction for Via Arrays in Parallel Planes for Power Distribution Network Design," *IEEE Trans. Microw. Theory Tech.*, vol.58, no.9, pp.2434-2447, Sept. 2010.
- [A-17]M. Leone, and H. Singer, "Efficient Computation of Radiated Fields From Finite-Size Printed Circuit Boards Including the Effect of Dielectric Layer," in *1999 IEEE Int. Symp. Electromagn. Compat.*, Seattle, WA, Aug. 2-6, vol. 1, pp. 81-90
- [A-18]C. Ho, A. E. Ruehli, and Brennan, "The modified nodal approach to network analysis," *IEEE Trans. on Circuits and Systems*, Vol. CAS-25, pp. 504-509, Jun. 1975.
- [A-19]H. H. Park, J.-H. Jung, T.-S. Jang, S.-T. Han, S.-H. Song, J.-J. Park, and H.-B. Park, "Prediction of radiated EMI from PCB excited by switching noise of IC," *Microw. Opt. Technol. Lett.*, vol. 51, no. 10, pp. 2262–2266, Oct. 2009.
- [A-20]E. Park, H. Kim, J. Shim, Y. Kim, Y. Kim, J. Kim, "Analytical Calculation of Jitter Probability Density at Multistage Output Buffers Due to Supply Voltage Fluctuations," *IEEE Trans. Electromag. Compat.*, vol.57, no.4, pp.796-806, Aug. 2015
- [A-21]J. Kim, J. Lee, S. Ahn, J. Fan, "Closed-Form Expressions for the Noise Voltage Caused by a Burst Train of IC Switching Currents on a Power Distribution Network," *IEEE Trans. Electromagn. Compat.*, vol.56, no.6, pp.1585-1597, Dec. 2014

- [A-22]T. Roy, L. Smith, and J. Prymak, “ESR and ESL of ceramic capacitor applied to decoupling applications,” in *Proc. Elect. Perform. Elect. Packag. Conf.*, Oct. 1998
- [A-23]M. Togashi, “ESR Controlled MLCCs and Decoupling Capacitor Network Design,” *DesignCon 2007*, Jan, 2007
- [A-24]I. Novak, S. Pannala, J. Miller, “Overview of some options to create low-Q controlled-ESR bypass capacitors,” in *Proc. EPEP*, Nov. 2004, pp. 55-58.

## 감사의 글

석·박사 5년 반이란 시간을 되돌아보며 짧은 글로나마 감사의 말을 전합니다.

이 논문이 나오고 학위를 마치는 데까지 부족한 저에게 많은 관심과 지도해 주신 김진국 교수님께 누구보다 먼저 감사드립니다. 교수님 지도 아래, 보고 배웠던 학문적 지식과 연구에 대한 열의는 어디에서도 얻을 수 없는 값진 것들이었습니다. 그 열정적인 모습 본받아 노력하며 열심히 살아가겠습니다. 또한 바쁜 일정 가운데 논문 심사위원 및 논문 지도를 해 주신 김재준 교수님, 정지훈 교수님, 김예린 교수님, 한기진 교수님께도 감사드립니다.

잠버릇이 고약한 룸메이트 만나 고생한 동기 상현이와 성우 형에게 심심한 사과와 감사의 말을 전합니다. 같이 지내는 동안 아침마다 알람으로, 밤으로는 잠꼬대로 괴롭혀서 미안하고 이해해줘서 고맙습니다. 말 많은 동생 투덜거림, 고민거리 개의치 않고 들어 주시고 조언해주시는 BICDL 의 형근이형, 경민이형 고맙습니다. 필요한 순간마다 선뜻 도와준 CSDL 의 경환이와 수빈이에게도 감사의 말의 전합니다.

랩 초기부터 같은 공간에서 같이 고생한 영곤이 형, 연구실에 문제 있을 때마다 도움 주셔서 고맙습니다. 티격태격하기도 했지만 동기로 많이 의지했던 종우에게도 감사하다는 말을 전합니다. 그리고 베리타스 모임 알려주신 희돈이 형, 신앙적으로나 생활적으로 조언과 도움 주셔서 감사합니다.

ICEMC Lab 구성원들에게도 감사의 말을 전합니다. 좋은 본을 보이고 앞서 졸업한 은경, 명준이에게 감사합니다. 연구 중에 막힐 때 같이 고민하고 조언해 줬던 연구실의 브레인 준식이와 상영이, 혼자서도 자기 일을 척척 잘 해 나가고 있는 경진, 남다른 유머코드를

가지고 있는 명조, 연구실에서 불박이처럼 묵묵히 잘 하고 있는 우룡, 동욱, 병진, 부족하고 미숙한 랩장이었지만 잘 따라와주어서 진심으로 감사합니다. 차후 연구실을 이끌어 갈 동생들보면 든든하고 기대됩니다.

힘들 때마다 먼저 연락 와서 말동무가 되어주 친구, 호성이에게도 이 자리를 빌려 감사하다는 말을 전합니다. 대학 동기로 형제같은 나의 벅들, 패션니스타 철순, 센스쟁이 한수, 개구쟁이 재인, 듬직한 민석, 우러러보게 되는 준승, 항상 걱정되는 희섭, 룬호의 슈퍼맨 정수, 세상 속에서 나에게 쉼이며 각자의 삶 속에서 고군분투하는 모습은 나에게 자극제가 되었습니다. 고맙습니다.

기도로서 주시는 정태윤 목사님과 이영숙 사모님 자주 찾아 뵈지 못해서 늘 죄송하고 목사님과 사모님의 기도 덕분에 무탈하게 잘 마칠 수 있었습니다. 감사합니다.

믿음 안에서 한 형제인 현기형, 민의형, 신앙적으로 같이 고민하고 믿음의 길을 서로 의지하며 걸어갈 동역자가 있다는 것이 얼마나 큰 축복인지 모릅니다. 고맙습니다.

누나 같은 동생 은미의 세심한 배려와 조언들이 언제나 나를 되돌아보게 하였고, 나를 인격적으로 성장하게 하였습니다. 감사합니다. 나의 안식처, 사랑하는 현주, 떨어져 있어서 자주 보지 못하고 잘 챙겨주지 못해서 미안하고, 함께 있어서 힘든 시간 잘 견뎌 낼 수 있었습니다. 고맙습니다. 무뚝뚝한 손자, 외할머니의 헌신이 있었기에 지금의 내가 있을 수 있었음을 이 글을 빌어 고백합니다. 감사합니다.

삶의 표석이자 가장 큰 선생 되시는 아버지께 감사의 말을 전합니다. 나에게 있어 가장 큰 유산은 아버지께서 삶으로 보여주신 성실과 근면입니다. 날마다 아들 기도로 새벽을 깨우시는 어머니, 세상 속에서 흔들리지 않는 믿음의 본이 되어 주셔서 감사합니다.

고난 중에 도움이셨고, 환난 중에 피난처였으며, 날마다 새 힘주시는 하나님 아버지께 경배와 찬양을 올려드립니다. 하나님께서 지금까지 그리고 여기까지 인도하셨습니다.

하나님께서 이끌어 가실 이다음 또한 기대하고 선한 것들로 채워 가실 것임을 신뢰합니다.

다양한 손길로 도움 주신 모든 분들께, 다시 한번 감사드리며 마지막으로 나를 되돌아볼 때 묵상하는 성경 구절로 이 논문과 감사의 글을 마칩니다. *Soli Deo Gloria*

“우리가 이 보배를 질그릇에 가졌으니  
이는 심히 큰 능력은 하나님께 있고  
우리에게 있지 아니함을 알게 하려 함이라  
고린도 후서 4:7 ”

## CURRICULUM VITAE

### EDUCATION

**2012.09 ~ 2018.02** Combined M.S-Ph.D in Department of Electronic Engineering,  
Ulsan National Institute of Science and Technology (UNIST), Ulsan, Korea  
**Major:** EMI/EMC  
**Thesis Title:** Quantified Design Guidelines of Compact Active EMI Filters to  
Reduce the Common-Mode Conducted Emissions  
**Advisor:** Prof. Jinguok Kim

**2006.03 ~ 2012.08** B.S in Department of Electrical Engineering  
Kumoh national Institute of Technology (KIT), Gumi, Korea

### PUBLICATIONS

- [1] **D. Shin**, S. Kim, G. Jeong, et al. "Analysis and design guide of active EMI filter in a compact package for reduction of common-mode conducted emissions," *IEEE Trans. Electromagn. Compat.*, vol. 57, no. 4, pp. 6670-671, Aug. 2015.
- [2] **D. Shin**, N. Kim, J. Lee, Y. Park and J. Kim, "Quantified Design Guides for the Reduction of Radiated Emissions in Package-Level Power Distribution Networks," *IEEE Trans. Electromagn. Compat.*, vol. 59, no. 2, pp. 468-480, April 2017.
- [3] **D. Shin**, S. Jeong and J. Kim, "Quantified Design Guidelines of Compact Transformerless Active EMI Filter for Performance, Stability, and High Voltage Immunity," Accepted to *IEEE Trans. Power Electron.*
- [4] **D. Shin**, S. Kim, G. Jeong, J. Park, J. Park, K. J. Han, and J. Kim, "A common-Mode Active Filter in a Compact Package for a Switching Mode Power Supply", in *Proc IEEE Int Symp Electromagn. Compat.* Aug 2014.
- [5] **D. Shin**, J. Park, N. Kim, J. Lee, Y. Park, and J. Kim, "Efficient Calculation of EMI Factors from Power Distribution Network using Cavity Resonance Circuit Model", *Proc. Electrical Design of Advanced Packaging and Systems Symposium (EDAPS 2015)*, pp. 140-143, Dec. 2015



- [6] **D. Shin**, C. Son, S. Jeon, B. Cho, J. Han, and J. Kim, "A simple low-cost common mode active EMI filter using a push-pull amplifier" in *2016 IEEE Energy Conversion Congress and Exposition (ECCE)*, Milwaukee, 2016, pp. 1-5.
- [7] K. Kwak, **D. Shin**, J. Kim and J. Kim, "Dipole-moment model including phases for IC near-field analysis based on GTEM cell measurements," *2016 Asia-Pac. Int. Symp. Electromagn. Compat.* May 2016, pp. 605-607.
- [8] S. Jeong, **D. Shin**, J. Kim, J. Kim and S. Kim, "Design of effective surge protection circuits for an active EMI filter," *2017 Asia-Pac. Int. Symp. Electromagn. Compat.*, Jun. 2017, pp. 210-212.